UNIVERSITY OF CALIFORNIA, SAN DIEGO

Magnetotelluric Exploration of the Aleutian Arc: Mantle Melt Generation and Migration beneath Okmok Caldera

A Thesis submitted in partial satisfaction of the requirements
for the degree Master of Science

in

Earth Sciences

by

Georgianna Zelenak

Committee in charge:

Professor Kerry Key, Chair
Professor Geoffrey Cook
Professor Leonard Srnka

2016

The Thesis of Georgianna Zelenak is approved and it is acceptable in quality and form for publication on microfilm and electronically:

_____

_____

_____

Chair

University of California, San Diego

2016

DEDICATION

To my parents Amy and Steve Zelenak, my brother Andy and sister-in-law Little Andy, and my grandmother Polly Knight.

TABLE OF CONTENTS

LIST OF FIGURES

LIST OF TABLES

ACKNOWLEDGEMENTS

I would first of all like to thank my many mentors beyond Scripps. Thanks to Graham Hill for the many lessons in MT theory, and for access to the CRAY computing cluster at the University of Hawaii. Thanks to Don Thomas and Erin Wallin for the many interesting discussions and for the opportunities to work with Center for the Study of Active Volcanoes. Thanks also to Danny Feucht for introducing me to the amazing world of fieldwork.

Thanks to my committee members for the guidance throughout this process. I would also like to thank Jake Perez, Chris Armerding, and Jacques Lemire in the Marine EM Lab at Scripps for the many opportunities to help with tech work. Learning to drive the forklift is still one of the highlights of grad school.

Thank you to everyone involved in the fieldwork for this project, both onshore and offshore. Thank you to Neil, Dale, and Ivan from the Bering Pacific Cattle Ranch for making sure that I always had a warm dry coat heading into the field, and for the countless stories around the woodstove. Thank you to our fantastic pilots Sam and Dan for getting us to and from our sites safely, and thanks to mechanic Sean for promising to rescue me himself if we ever got stuck in the caldera. During such a crazy field campaign it made a huge difference to know that such capable people were in our corner. Thanks of course also to the crews on the R/V Thompson and R/V Sikuliaq.

Thanks also to Jim Ingle at Stanford University for teaching me as a high school student that there are mountains under the ocean, and for telling me amazing stories that made me dream of studying what is beneath the sea. Thanks to the many professors at Colorado School of Mines who took the time to be not only great researchers but also great teachers and mentors.

Thank you to the Harvey family. Your faith in me over the years and your never-ending support of my education and dreams has meant the world to me.

Thanks to all of the friends who kept me sane through this process. Huge thank you to the Neosho House roommates (and the hot tub), for helping make San Diego home, and for the endless love when I was struggling the most. Thanks to Telma Sigurõardóttir for being my MT sister and fearless viking adventure buddy. Thank you to Virginia Clay for the many reminders that there is a wide world outside of Scripps.

And of course, thank you to my incredible family. Thank you for supporting every crazy idea that I have come up with, from SEA to Rio to working inside an active volcano. Dad, thanks for teaching me how to solder and giving me my first knife and .22. Who could have guessed how useful those skills would be as a geophysicist.

ABSTRACT OF THE THESIS

Magnetotelluric Exploration of the Aleutian Arc: Mantle Melt Generation and Migration beneath Okmok Caldera

by

Georgianna Zelenak

Master of Science in Earth Sciences

University of California, San Diego, 2016

Professor Kerry Key, Chair

In the summer of 2015, a geophysical survey was completed across Okmok Caldera in the Aleutian Islands. Okmok is an active volcano with eruptions every 10-20 years in recent history (*Miller et al.,* 1998). In order to better understand the melt system beneath the volcano, data were collected at 54 marine magnetotelluric (MT) and 23 onshore MT stations in an amphibious array crossing from the forearc into the backarc. Thirteen temporary broadband seismometers were also installed onshore for one year to supplement the network of 13 permanent seismometers on the island. Initial processing of

the marine MT data reveals complex features across many of the stations, with full wrapping of the phase in both transverse electric (TE) and transverse magnetic (TM) modes. Attempts to invert these data using a two-dimensional finite element based inversion code resulted in poor RMS goodness-of-fit values, and evaluation of skew and polarization plots indicates that much of the data is impacted by 3D geologic structure. In order to understand what subsurface features could be consistent with the complex responses seen in the marine MT data, forward modeling was completed using a version of the freely-available 3D code ModEM that was modified to accommodate the marine environment. The 3D forward modeling shows that the complex offshore topography strongly distorts the MT responses. Simple models of seafloor resistivity represented as a half-space with bathymetry are able to account for a significant fraction of the observed MT response structure. More quantitative interpretation of the offshore MT data requires a 3D inversion code capable of including the complex 3D seafloor bathymetry.

Chapter 1

Introduction

The surface of the Earth is composed of distinct tectonic plates that move relative to each other as material is created at mid-ocean ridges and recycled at subduction zones where two converging plates meet. As the denser slab sinks beneath the lighter overriding plate at subduction zones, fluids contained in the sediments are released. These fluids decrease the melting point of mantle materials, leading to partial melting of the overriding mantle and creation of extensive volcanic arcs, such as the Aleutian Arc off the coast of Alaska (*Peacock,* 1990). Okmok Caldera and the associated volcanic center on Umnak Island in the Aleutians provide excellent targets for geophysical studies of magma generation and transport throughout the subsurface. Previous studies in the area have used active and passive seismic methods to constrain regional structure associated with the subduction zone, and numerous GPS, InSAR, and seismic studies have attempted to constrain crustal magmatic features beneath the caldera. In the summer of 2015, a magnetotelluric (MT) survey was completed across the area in order to provide new constraints on the electrical resistivity structure in the subsurface.

1.1 Global subduction

The surface of the Earth consists of distinct tectonic plates that move relative to one another as new oceanic crust is created along mid-ocean ridges. Subduction zones are found where these plates of collide. Where the two plates meet, differences in buoyancy drive the denser oceanic lithosphere beneath the less dense overriding plate. These differences in buoyancy can be due to either thermal or compositional differences. Today oceanic crust is being subducted along 43,500 km of the surface of the Earth (*von Huene and Scholl,* 1991). Nearly 40% of this subduction involves oceanic lithosphere being subducted beneath oceanic lithosphere of different buoyancy (*Leat and Larter,* 2003).

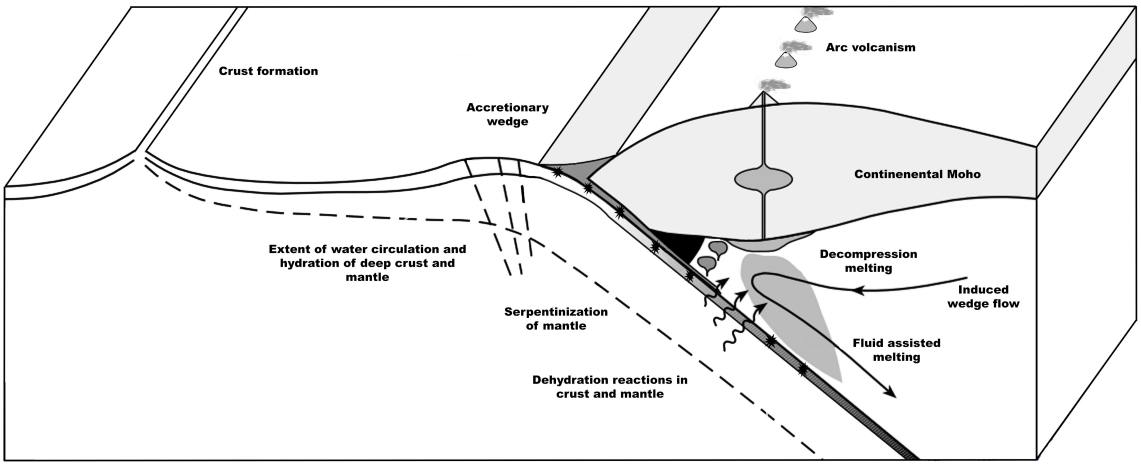

Figure 1.1: Simplified illustration of subduction zones. Modified from van Keken (2003).

As oceanic lithosphere subducts, there is significant deformation, which is accommodated along near-surface faults on the bending plate and through large underthrusting earthquakes in the seismogenic zone (*van Keken*, 2003). This down dip limit of the seismogenic zone generally ends at the continental Moho. Down-dip of this, earthquakes are located within the slab. In this deeper section of the subduction zone, the overlying mantle is coupled with the down-going slab. Viscous drag draws mantle material down with the slab, and mantle from along the overriding plate is drawn in towards the region of subduction. This area of deformation is referred to as the mantle wedge in most of the literature. Note that this model of subduction, as illustrated in Figure 1.1, is extremely simplified. Complications such as the slab geometry, age, and speed, as well as buoyancy forces in the wedge, are ignored.

When oceanic lithosphere is subducted, the sediments, crust, and hydrated mantle are dehydrated by various depth dependent mechanisms. The influx of water in the overlying mantle leads to increased melt generation by lowering the melting temperature of mantle peridotite. This partial melt gradually rises to feed arc volcanism, as seen in the Aleutian Islands where 41 active volcanoes are associated with the subduction zone.

1.2 Aleutian arc geology

The Aleutian Arc extends nearly 3000 km from the Kamchatka Peninsula to the Gulf of Alaska. The subduction zone along the arc has a complex geologic history, beginning with the Pacific and Kula plates subducting beneath the North American plate prior to 56 Ma. During the Cretaceous period, several complex terranes were transported up from the south and accreted to the southern portions of the Alaskan and Beringian

margins (*Plafker et al.,* 1994). By roughly 60 Ma, the Beringian margin became mostly strike-slip, but volcanism continued along the southern and western Alaskan margins, covering the accreted terranes with volcanics.

At 56 Ma, the plate boundary jumped south and west from the Beringian margin. This trapped a part of the oceanic Kula plate against the North American plate as the Beringian margin became passive, forming the current subduction zone at the eastern end of the arc (*Worral*, 1991).

At around 50 Ma, the plate boundary again jumped west, establishing the present subduction zone in the western Aleutians. By 40 Ma, the Kula plate, with the exception of the relic portion trapped against the North American plate, had totally subducted. There was a change in the motion of the Pacific plate and a sudden reduction of subduction speed. From that point forward, tectonics proceeded similar to today,

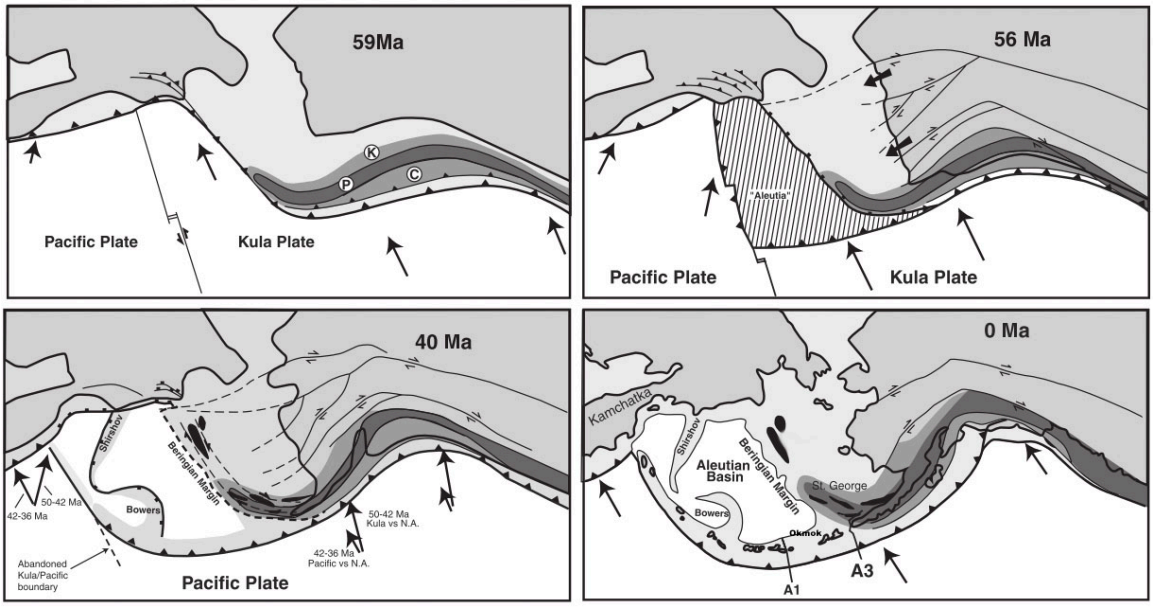

Figure 1.2: Tectonic history of the Aleutian Arc. In the present-day arc, the Pacific plate is subducting beneath the relic Kula plate in the west, and continental accreted terranes in the east. Modified from Lizarralde et al. (2002).

with the Pacific plate subducting beneath the accreted terranes on the eastern end of the arc while in the western portion of the arc, the Pacific plate is sliding beneath oceanic crust associated with the trapped portion of the Kula plate (*Lizarralde et al.,* 2002).

Today most authors reference the break in the slope of the continental crust at 164°W near Unimak pass as the transition between oceanic and continental crust on the overriding plate. To the west of Unimak Pass, the oceanic lithosphere of the Pacific plate is subducting beneath the trapped portion of the Kula plate, while to the east, the overriding plate is composed of the Mesozoic terranes that were accreted during the Cretaceous and then subjected to tectonism, erosion, and reintrusion (*Lizarralde et al.,* 2002). As Umnak Island is to the west of Unimak Pass, Okmok volcano formed on oceanic crust.

In general, volcanic centers in the eastern portion of the arc tend to be larger. This is attributed to the angle of subduction relative to the angle of the arc. In the western portion of the arc, the Pacific plate is moving nearly parallel to the subduction zone, while in the Eastern portion the subducting plate is moving close to perpendicular to the arc. This leads to an increased convergence rate in the east that is believed to cause the larger volcanic centers (*Marsh,* 1979).

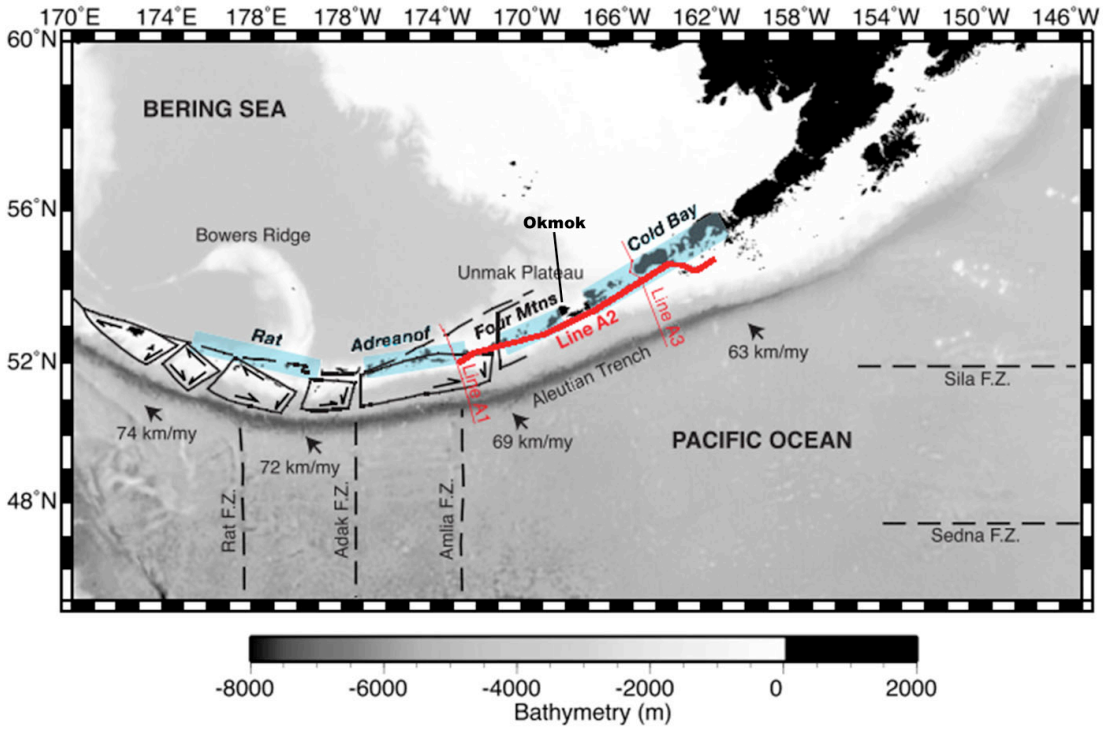

Figure 1.3: Location of 1994 Aleutian survey, with red lines indicating survey lines. Arc segments are indicated with blue boxes. Motion of the Pacific plate relative to the North American plate is indicated with arrows. Modified from Shillington et al. (2004).

Many authors break the Aleutian arc into distinct segments, with the edges of segments coinciding with major tectonic breaks in the plates or the terminations of rupture zones from earthquakes (*Kay and Kay,* 1994). In general, larger volcanic centers are found at the ends of segments or between segments (*Kay and Kay,* 1994). Note that Okmok Caldera is located between the Four Mountains and Cold Bay segments (Figure 1.3).

It is also worth noting that one study points to a secondary volcanic front behind the main subduction zone centers in the region from Cold Bay to the Four Mountains segment of the arc. The volcanic centers on this secondary front are much smaller, as seen at Bogoslof Island to the northeast of Okmok (*Kay and Kay,* 1994).

1.3 Aleutian arc subduction

Most previous geophysical studies of arc structure around Okmok use data from the 1994 Aleutians experiment. The seismic reflection and refraction survey covered approximately 700 km of the arc, from Unimak Pass to Seguan Pass as shown in Figure 1.4. Shots were fired on a 20-element airgun array, and recorded on a 4-km multi-channel hydrophone streamer. Ocean-bottom seismometers (OBS) and hydrophones, as well as a small number of onshore portable seismometers, also recorded the shots (*Holbrook et al.,* 1999). The survey consisted of three primary parts: 1) a line running trench-perpendicular through Unimak Pass (*Holbrook et al.,* 1999), 2) a line running trench-perpendicular through Seguan Pass (*Lizarralde et al.,* 2002), and 3) a trench-parallel line 40 km into the forearc (*Fliedner and Klemperer*, 1999; *Shillington et al.,* 2004; *Shillington et al.,* 2013).

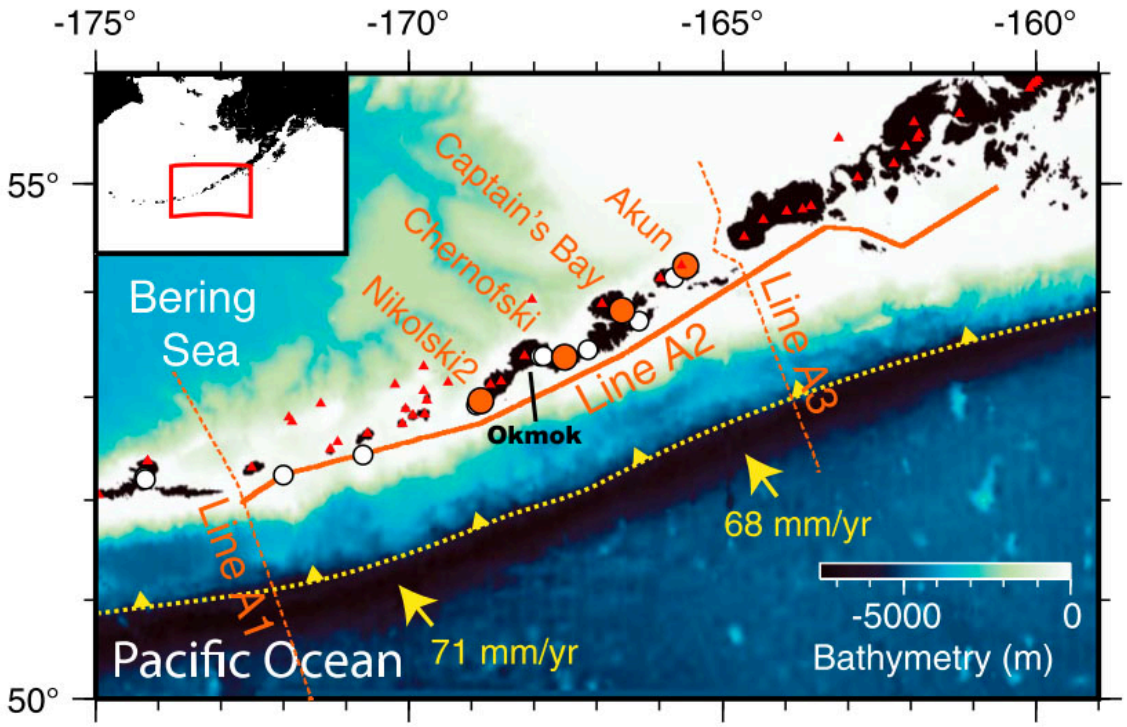

Figure 1.4: Map of the 1994 Aleutian experiment, with orange lines showing shot tracks and orange and white circles showing seismometers. The red triangles show volcanoes in the region. Plate motion rates are relative to the North American plate. Modified from Shillington et al. (2013).

Surprisingly, the two trench-perpendicular lines show remarkably similar structure. On both lines A1 and A3, there are three main crustal units (*Holbrook et al.,* 1999; *Lizarralde et al.,* 2002). The upper-most layer is roughly 5-10 km thick, and is interpreted to be volcaniclastic sediments, flows, and small plutons. Lizarralde et al. (2002) go on to subdivide this shallow crustal layer into five sub-layers, all with low velocities under 6 km/s. Lizarralde et al. (2002) and Holbrook et al. (1999) identify a midcrustal layer that is believed to be oceanic crust, based on both thickness and velocity structure. A final lower crustal layer of variable thickness brings the total crustal thickness to 25-30 km along both transects that run arc-parallel (*Lizarralde et al.,* 2002). This agreement between the two profiles at opposite ends of the survey indicates that

there is continuity in structure across the arc, even though the overriding plate on the western end of the arc is the oceanic relic Kula plate, and on the eastern end the overriding plate is accreted terranes.

An early study of the arc-parallel profile using P-wave velocities from onshore instruments and the two OBS revealed 30-km-thick mafic crust (*Fliedner and Klemperer*, 1999). However, as Shillington et al. (2004) points out, this study did not account for bathymetry and near-surface changes in structure. The five shallow crustal layers identified by Lizarralde et al. (2002) could have a major impact on the interpretation of deeper structure. Shillington et al. (2004) used the data collected by the OBS and the multi-channel seismic (MCS) data to complete 3D ray tracing and 2.5D inversions. The work revealed three crustal layers, with total crustal thickness of 35-37 km. In addition to thicker crust, the Shillington et al. (2004) work showed greater lateral continuity and vertical stratification than the Fliedner and Klemperer (1999) results.

Shillington et al. (2013) used converted S-waves to calculate Vp/Vs ratios across line A2, parallel to the arc. It was found that the average Vp/Vs ratio was low for the lower crust, while Vp was high. The authors used petrologic modeling to show that the best explanation for this combination is a mixture of clinopyroxenite with smaller amounts of mafic material containing alpha quartz (*Shillington et al.,* 2013).

Janiszewski et al. (2013) expanded the survey area beyond the 1994 Aleutians experiment by incorporating receiver functions from stations across the arc (see Figure 1.5). The study finds that crustal thickness stays constant at 38.5 km across the arc (omitting stations on Attu. Leaving in the western-most stations yields a crustal thickness of 37.5 km). This is surprising, as the composition of the overlying plate changes from

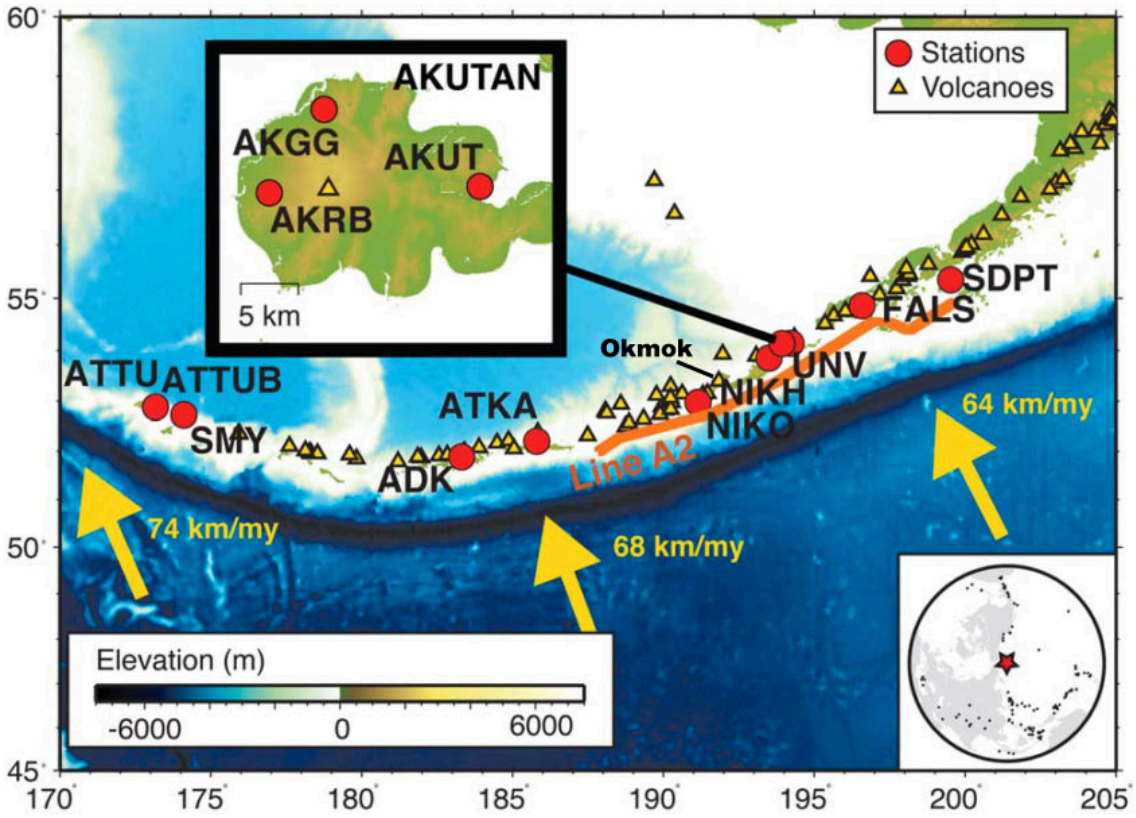

Figure 1.5: Locations of the seismic stations used by Janiszewski et al. (2013) across the arc. The orange line indicates the line of shots collected parallel to the arc during the 1994 Aleutian project. Bottom inset shows the locations of earthquakes used in calculating receiver functions. Modified from Janiszewski et al. (2013).

continental to oceanic crust moving westward. The authors suggest that erosion and isostasy are acting to keep crustal thickness constant across the two different subduction environments. The study also finds an increase in Vp/Vs moving west across the study area. This is believed to come from the gradient in SiO_2 content across the averaged crust. Overall, the results of Janiszewski et al. (2013) are consistent with the Shillington et al. (2004) findings, and indicate a thicker crust than earlier studies along the cross-lines of the 1994 Aleutians experiment.

1.4 Okmok setting

The Aleutian Arc is among the most volcanically active regions on Earth, containing 41 volcanoes that are deemed capable of a major eruption in the near future. Umnak Island in the eastern Aleutians is home to three of these volcanoes. The island sits on oceanic crust at the eastern end of the Aleutian Island chain, just west of the break in the slope of the continental shelf that marks the transition from continental to oceanic crust. It is located approximately 1400 km southwest of Anchorage and 100 km west of Dutch Harbor.

Umnak is made up of two lobes, with the andesitic stratovolcanoes Vsevidof and Recheschnoi on the southwestern portion of the island, and the tholeiitic shield volcano Okmok on the northeastern part. The southwestern and central parts of Umnak have much rougher topography, while the gently sloping flanks of Okmok dominate the northeastern section (see Figure 1.7). These differences in composition and structure suggest a dramatic change in the magmatic system creating the volcanoes across a small area.

Okmok occupies almost the entirety of the northeastern portion of the island, with the 10 km diameter caldera roughly centered. The highest point on the caldera rim is just over 1000 m above mean sea level, some 500-800 m above the caldera floor. The relatively low profile of Okmok, combined with the close proximity to a major port, simplifies many of the logistics of working in such a remote region.

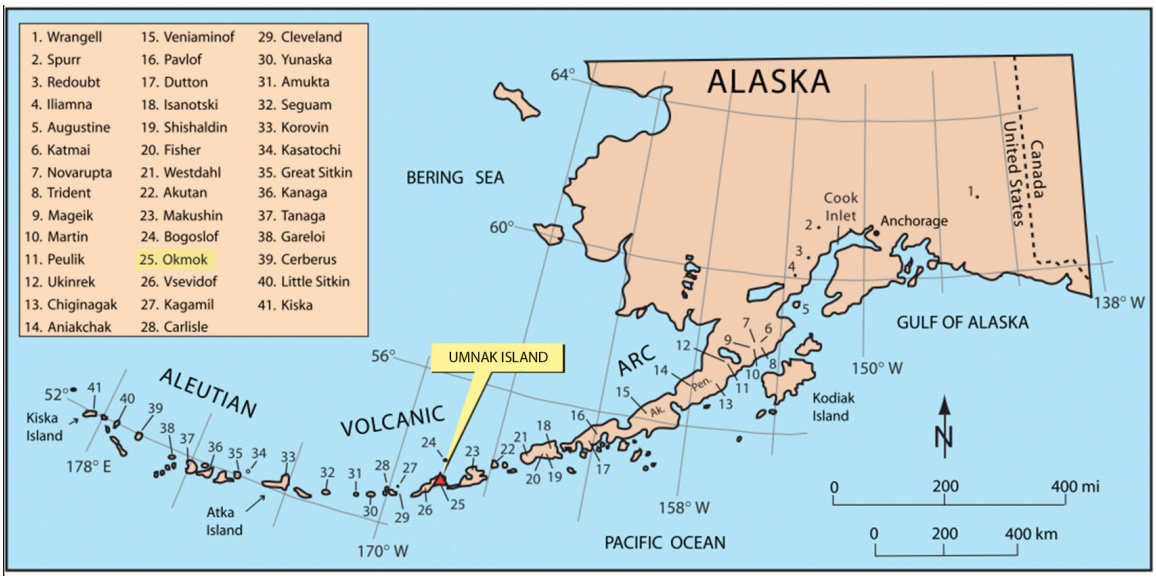

Figure 1.6: Locations of the 41 volcanoes deemed capable of major eruptions in the near future in the Aleutian Arc. Modified from Begét et al. (2005).

Figure 1.7 reveals that Okmok is a very complex volcanic system. The most obvious feature is the large, roughly circular caldera. However, a closer look reveals that there are actually two large nested calderas. Within the caldera, a series of cones is evident, with the most prominent Cones A and D labeled in the image. In addition, we see volcanic cones such as Tulik Volcano and Jag Peak on the flanks of the volcano. It is quite remarkable that a single magmatic system may be responsible for such a variety of volcanic structures in a small region. An overview of these major features and the eruptions that have formed them is valuable for this research, as past eruptions often give the best clues as to what future volcanic activity may look like.

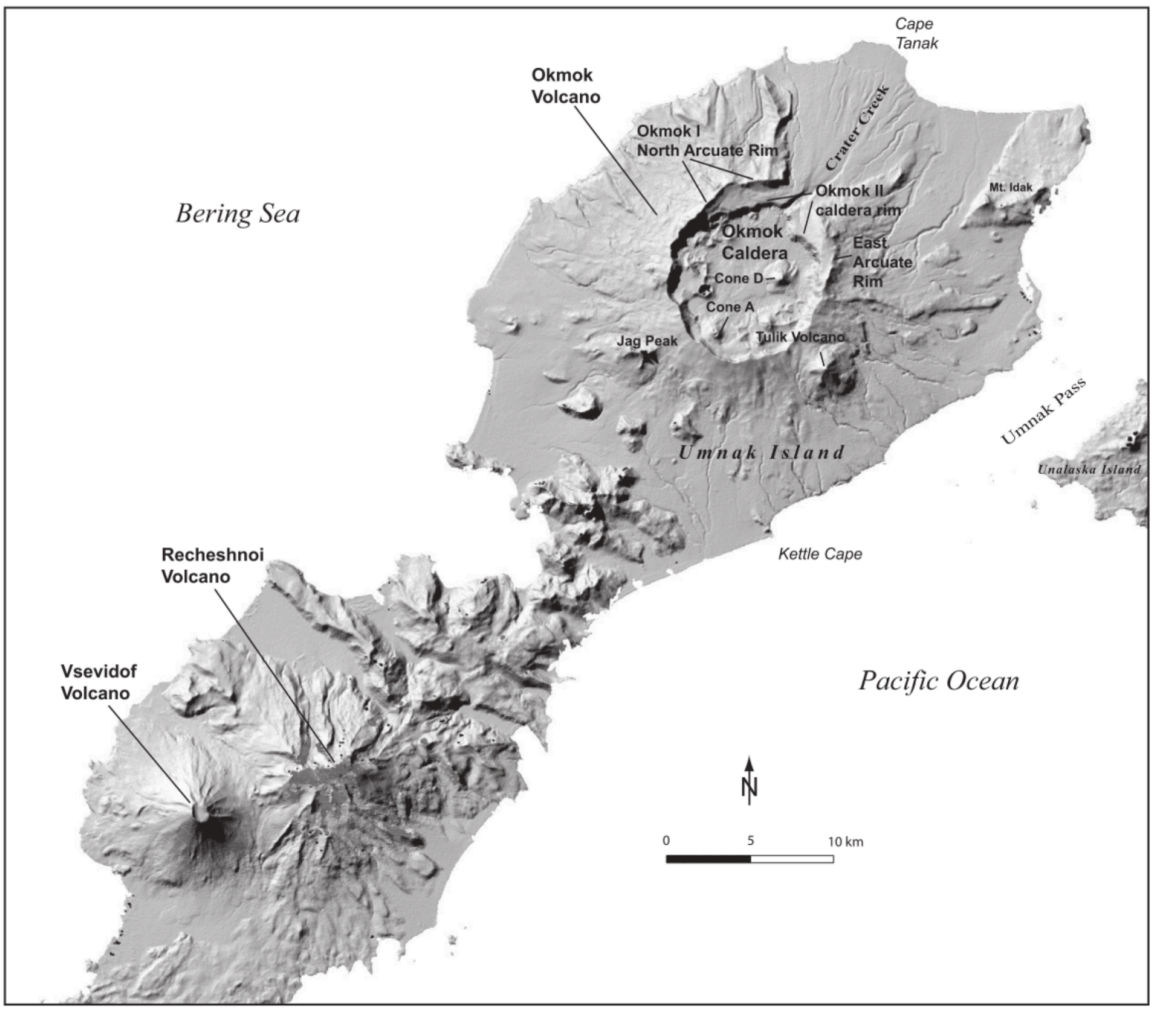

Figure 1.7: Shaded relief image of Umnak Island, including Vsevidof and Recheshnoi volcanoes in the southwest, and Okmok in the northeast. Modified from Larsen et al. (2007).

1.5 Prehistoric eruptions at Okmok

Before the caldera-forming eruptions took place Okmok was primarily effusive. One study using radiometric dating found that the volcano has been active for at least one million years, although deposits older than 12,000 years have either been covered by more recent deposits or have been modified by glaciation (*Nye*, 1990). It is therefore only possible to recover a detailed record for the past 12,000 years.

The first caldera-forming eruption at Okmok (referred to as Okmok I) occurred approximately 12,000 yBP (years Before Present) (*Bean,* 1999). This eruption produced ~30 km^3 dense rock equivalent (DRE) (*Larsen et al.,* 2007). The second caldera-forming eruption, Okmok II, took place within the Okmok I caldera roughly 2050 yBP. This second caldera-forming eruption was smaller, with only ~15 km^3 DRE (*Patrick et al.,* 2003). It is believed that both of these eruptions started with small volumes of rhyolite and rhyodacite magmas, but the greater volume of extruded material was andesite and basaltic andesite magmas (*Larsen et al.,* 2007).

An outcrop at Kettle Cape on the south side of Okmok shows at least 43 volcanic ash layers between an organic layer dated at 8,600 yBP and a pyroclastic flow from the 2050 yBP caldera-forming eruption. This indicates an eruption periodicity of 150 years during this time period. However, in all likelihood there were many more eruptions that were not large enough to leave geologic deposits at this site 15 km from the caldera (*Begét et al.,* 2005). A change in prevailing wind direction could also prevent ash from being deposited at this location during an eruption. This 150-year eruption interval is therefore taken as the minimum. It should be noted that four of these large deposits appear to be phreatomagmatic in nature, meaning that there was interaction between magma and surface water.

Less is known about the cones and lava flows on the flanks of the volcano. They do not appear to be glacially eroded, and are believed to be older than the Okmok II caldera-forming eruption. This would indicate that they were formed between 12,000 and 2,050 yBP. There were some reports of Tulik Volcano erupting within historic times, but geologic studies have found no evidence of recent deposits from this area. It is

believed that the eruptions attributed to Tulik instead were inside the caldera, but were obscured by angle or cloud cover (*Begét et al.,* 2005).

At Kettle Cape tephra layers are also preserved from 24 eruptions since the second caldera-forming event. This would indicate that there have been large eruptions capable of depositing material 15 km from the caldera every 75 years for the past 2,000 years. This suggests a change in either eruption frequency or explosiveness compared to the time between caldera-forming eruptions (*Begét et al.,* 2005). All of the eruptions since Okmok II are believed to have been at one of the eight volcanic cones that are younger than 2050 yBP inside the caldera (*Byers,* 1959).

1.6 Eruptions during historic times

Since the first Russian records, there have been at least sixteen eruptions, both effusive and explosive in nature, at Okmok (Table 1). All of the eruptions since World War 2 (with the exception of 2008) have occurred at Cone A, but other cones have likely been active since the 1800s. Some reports suggest that Tulik Volcano has erupted in recent times, but there is no geologic evidence for this. Over the past 200 years, the average eruption interval has been 12 years (*Begét et al.,* 2005). Since 1930, this interval has decreased to 7 years. All of these eruptions from historic times were too small to be preserved as geologic deposits, with the exceptions of eruptions in 1817 and 1958 (*Begét et al.,* 2005). This suggests that there were many smaller prehistoric eruptions that were not preserved in the rock record at Kettle Cape.

Table 1.1: Historical eruptions of Okmok, modified from *Begét et al.,* 2005

Date	Repose (yr.)	Vent (Cone)
1805	-	?
Mar. 1 or 2, 1817 (to 1820?)	12	E?B?
1824-1830	7	B?
1878	48	A?
1899	21	A
Mar. 21- May 13, 1931	32	A?
1936	5	A
1938	2	A
June 1943	5	A
June 4- Dec. 1945	2	A
Aug. 14-25, 1958	13	A
Oct. 15, 1960- April 15, 1961	2	A
Mar. 24, 1981	20	A
July 8, 1983	2	A
Nov. 18, 1986- Feb. 26, 1988	3	A
Feb. 11- Apr. 1, 1997	9	A
July 12- Aug. 23, 2008	11	Near D

The first documented eruption of Okmok occurred in 1817. Lava flows from Cone B dammed an intra-caldera lake, eventually leading to a catastrophic flood along Crater Creek. This buried an Aleut village at Cape Tanak with flood deposits (*Begét et al.,* 2005).

Military personnel stationed at Fort Glenn observed the 1945 eruption. Several days prior to the eruption, there was a large earthquake felt throughout the area. A few days later, there was an eruption from Cone A that sent ash to 3,000 m. The eruption lasted close to six months, and ultimately created a 6.5 km-long lava flow (*Begét et al.,* 2005).

An eruption in 1958 was not nearly so well documented. The eruption from Cone A was primarily explosive, but also emplaced an 8 km lava flow across the caldera,

leading to the formation of a new lake. While little is known about this eruption, it was likely very similar to the 1945 eruption (*Begét et al.,* 2005).

In February 1997 an eruption from Cone A created a 10-50 m thick blocky lava flow crossing 6 km of the caldera, covering most of the flow from 1958. The ash cloud associated with this eruption was fairly small, reaching a maximum of 9 km above sea level. There were no seismic or geodetic instruments on the island at the time of this eruption, but remote sensing indicates a dense rock equivalent (DRE) of 0.12 km^3 (*Patrick et al.,* 2003).

On July 12, 2008, Alaska Volcano Observatory (AVO) received a call from the Coast Guard alerting them to an explosive eruption at Okmok. The cattle ranchers at Fort Glenn had made an emergency call indicating that they needed evacuation. Within five minutes of the phone call, AVO confirmed the eruption in the seismic network and by using satellite imagery. The volcano was immediately elevated from aviation code Green (meaning everything at quiet background levels) to aviation code Red (highly explosive eruption with significant ash emission). This was the first such occurrence in the history of AVO. In retrospect, scientists found less than five hours of precursory seismic activity. During the two months leading up to the eruption, there was no tremor and only three small earthquakes. There were no notable geodetic precursors (*Larsen et al.,* 2009). The unexpected nature of this eruption is especially important, as Okmok lies directly beneath trans-Pacific flight paths. See Appendix 2 for more information on the aviation hazard.

Aviation Color Code Used by USGS Volcano Observatories

Color codes, which are in accordance with recommended International Civil Aviation Organization (ICAO) procedures, are intended to inform the aviation sector about a volcano's status and are issued in conjunction with an Alert Level. Notifications are issued for both increasing and decreasing volcanic activity and are accompanied by text with details (as known) about the nature of the unrest or eruption, especially in regard to ash-plume information and likely outcomes.

Color	Description
GREEN	Volcano is in typical background, noneruptive state or, *after a change from a higher level,* volcanic activity has ceased and volcano has returned to noneruptive background state.
YELLOW	Volcano is exhibiting signs of elevated unrest above known background level or, *after a change from a higher level,* volcanic activity has decreased significantly but continues to be closely monitored for possible renewed increase.
ORANGE	Volcano is exhibiting heightened or escalating unrest with increased potential of eruption, timeframe uncertain, **OR** eruption is underway with no or minor volcanic-ash emissions [ash-plume height specified, if possible].
RED	Eruption is imminent with significant emission of volcanic ash into the atmosphere likely **OR** eruption is underway or suspected with significant emission of volcanic ash into the atmosphere [ash-plume height specified, if possible].

Figure 1.8: Color code used to communicate volcanic hazard to the aviation community (https://www.avo.alaska.edu/activity/alert_levels.pdf)

The 2008 eruption was phreatomagmatic in nature, with a volcanic explosivity index (VEI) of 4 (*Larsen et al.,* 2009). Geologic evidence exists for phreatomagmatic eruptions at Okmok in the past, but this stands in stark contrast to the more effusive eruptions from Cone A in historic times. The 2008 eruption was also unique in that it issued from a series of vents on the sides of Cone D, across the caldera floor from all of the recent eruptions at Cone A. Eventually the eruption led to formation of a new cone, called Ahmanalix, on the sides of Cone D (*Larsen et al.,* 2013). The name fittingly means "surprise" in the native language. Figure 1.9 shows the changes in structure within the caldera due to the 2008 eruption. In total, this eruption had a DRE of 0.26 km^3, more than twice what was seen from the 1997 eruption (*Larsen et al.,* 2013).

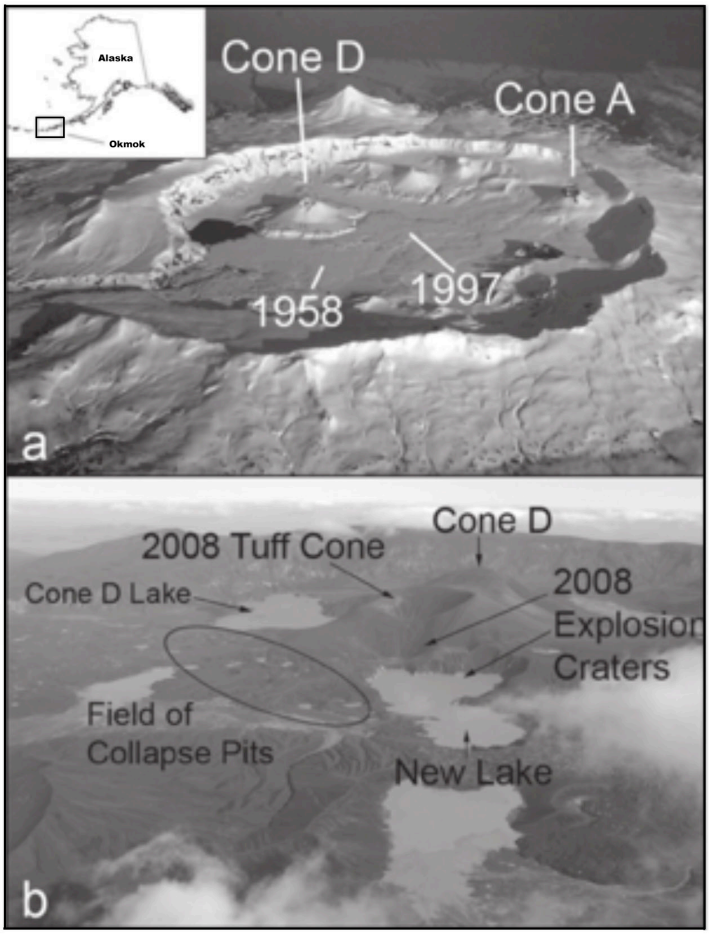

Figure 1.9: Photographs showing the changes in Okmok caldera associated with the 2008 eruption. (a) photograph looking south, showing cones A and D and lava flows from 1958 and 1997. (b) oblique aerial view showing new cone, lake, and collapse pits created during the 2008 eruption. Modified from Larsen et al. (2009)

1.7 Previous studies of crustal features

Early observations of eruptions at Okmok relied primarily on remote sensing and aircraft observations. Beginning in 2000, campaign-style GPS benchmarks were used at 33 points in and around the caldera. From 2000 until 2005 surveys were completed annually, although the most recent complete survey was in 2002. Following the 2008 eruption, seven of these benchmarks were reoccupied for seven months to record post-eruptive behavior. Between 2002 and 2004, four permanent GPS stations were also

installed across the island (*Freymueller and Kaufman,* 2010). In 2003, a permanent seismic network of ten short-period single-component seismometers and four broadband three-component seismometers was put in place (*Ohlendorf et al., 2014*).

Studies using GPS and InSAR in the early 2000's consistently found the source of deformation to be 2-3 km beneath the center of the caldera, as shown in Table 1.2. The models in these studies use Mogi sources, which are point sources in a homogeneous elastic half space with flat topography.

More recent studies using seismic methods have challenged that these assumptions are not appropriate for the complex geologic system at Okmok. Masterlark et al. (2010) made use of ambient noise tomography (ANT) to image two low velocity zones (LVZ) beneath the caldera. The shallower LVZ, extending from the surface to two kilometers, is interpreted as a zone of weak caldera material with high fluid saturation. A second LVZ at 4 km depth is believed to be a persistent magma reservoir that was molten as of late 2005. The study went on to test if this model of two low velocity zones was consistent with the InSAR interferograms from the same period. It is found that if the near-surface heterogeneity is factored in, the deeper magma chamber can explain the InSAR measurements (*Masterlark et al.,* 2010). Masterlark et al. (2012) followed up on this by demonstrating that shifting from a homogeneous elastic half-space model to a finite element model incorporating topography and heterogeneity shifted the source from 2664 m to 3527 m. It is concluded that homogeneous elastic half-space models can be good starting points for finite-element modeling, and can be useful for determining horizontal location, but should not be used independently for determining depth of a source.

Table 1.2: Summary of select recent studies of depth of Okmok magma chamber (Modified from *Ohlendorf et al., 2014)*.

Study	Time period	Data Type	Source depth (km bsl)
Mann et al. (2002)	1992-1998	InSAR	2.1-4.7
Miyagi et al. (2004)	2000-2002	GPS	2.7
Lu et al. (2005)	1992-2003	InSAR	3.2
Fournier et al. (2009)	2000-2007	GPS/CGPS	2.5
Lu et al. 2010	1997-2008	InSAR	3.1
Lu and Dzurisin (2010)	2007-2008	InSAR	2-3
Biggs et al. (2010)	1992-2007	GPS/CGPS/InSAR	3
Masterlark et al. (2010)		ANT	LVZ at 0-2, 4+
Ohlendorf et al. (2014)	2003-2009	P-wave velocity	LVZ 0-2, 6
Larsen et al. (2013)	2008	Petrological and geochemical	Less than 3, 3-6

Ohlendorf et al. (2014) presented a 3D P-wave velocity model for Okmok that is consistent with two low velocity zones. Based on the findings of the study, it is suggested that the anomalous eruption in 2008 was triggered by magma coming from a deeper magma chamber and interacting with a small pond of magma and groundwater beneath Cone D. However, the authors note that neither ANT nor this study using locatable earthquakes can resolve reservoirs in the range of 10 km deep. The two studies also cannot resolve if near-surface heterogeneity is due to caldera fill or shallow magma bodies.

Additional support for the theory of melt rising from a deeper chamber and interacting with a smaller near-surface chamber comes from a geochemical study of the 2008 erupted material. The material erupted from Cone A during historic times has been basaltic, while the 2008 material from Cone D is primarily basaltic andesite similar to what was erupted from Cone B in 1817. This sudden change in material over a mere 11 years indicates that the magma erupted in 1997 and 2008 is not from the same homogenous reservoir. Instead, it is suggested that basaltic material from a deeper magma chamber (3-6 km) rises and intersects a more evolved basaltic andesite magma chamber less than 3 km beneath Cone D (*Larsen et al.,* 2013).

These studies of the shallow crustal features at Okmok consistently place the source of deformation beneath the center of the caldera. With the exception of the 2008 eruption though, all eruptions in the past century have been at Cone A near the southern rim of the caldera. This indicates that magma is migrating horizontally approximately 3 km at some point during its ascent. Fournier et al. (2009) suggest that this occurs along dipping dikes or conduits that follow conical features, with dips ranging from roughly

45° to 90°. Masterlark et al. (2010) suggest that the base of the shallow LVZ is a horizon of neutral buoyancy beneath the center of the caldera. This horizon would drive magma towards the rim prior to eruption. It is suggested that the eruption at Cone D could be due to changes in the stress regime from loading of lava flows near Cone A (*Masterlark et al.,* 2010).

1.8 References

Bean, K. W. (1999). The Holocene eruptive history and stratigraphy of Makushin volcano, Unalaska Island, Alaska. *University of Alaska Fairbanks unpublished MS thesis*.

Begét, J. E., Neal, J. F., Nye, C. A., & CJ Schaefer, J. R. (2005). Preliminary volcano-hazard assessment for Okmok volcano, Umnak Island, Alaska. *Report of Investigations — Alaska. Division of Geological & Geophysical Surveys, 3*.

Byers Jr, F. M. (1959). *Geology of Umnak and Bogoslof Islands, Aleutian Islands, Alaska* (No. 1028-L). US Govt. Print. Off.,.

Fliedner, M. M., & Klemperer, S. L. (1999). Structure of an island‐arc: Wide‐angle seismic studies in the eastern Aleutian Islands, Alaska. *Journal of Geophysical Research: Solid Earth*, *104*(B5), 10667-10694.

Fournier, T., Freymueller, J., & Cervelli, P. (2009). Tracking magma volume recovery at Okmok volcano using GPS and an unscented Kalman filter. *Journal of Geophysical Research: Solid Earth*, *114*(B2).

Freymueller, J. T., & Kaufman, A. M. (2010). Changes in the magma system during the 2008 eruption of Okmok volcano, Alaska, based on GPS measurements. *Journal of Geophysical Research: Solid Earth*, *115*(B12).

Holbrook, W. S., Lizarralde, D., McGeary, S., Bangs, N., & Diebold, J. (1999). Structure and composition of the Aleutian island arc and implications for continental crustal growth. *Geology*, *27*(1), 31-34.

Janiszewski, H. A., Abers, G. A., Shillington, D. J., & Calkins, J. A. (2013). Crustal structure along the Aleutian island arc: New insights from receiver functions constrained by active‐source data. *Geochemistry, Geophysics, Geosystems*, *14*(8), 2977-2992.

Kay, S. M., & Kay, R. W. (1994). Aleutian magmas in space and time. *The geology of Alaska. Boulder. CO. Geol. Soc. Amer. The Geology of North America/Eds Plafteir G., Berg H*, *1*.

Larsen, J. F., Neal, C., Schaefer, J., Beget, J., & Nye, C. (2007). Late Pleistocene and Holocene Caldera‐Forming Eruptions of Okmok Caldera, Aleutian Islands, Alaska. *Volcanism and subduction: The Kamchatka region*, 343-364.

Larsen, J., Neal, C., Webley, P., Freymueller, J., Haney, M., McNutt, S., … & Wessels, R. (2009). Eruption of Alaska volcano breaks historic pattern. *Eos, Transactions American Geophysical Union*, *90*(20), 173-174.

Larsen, J. F., Śliwiński, M. G., Nye, C., Cameron, C., & Schaefer, J. R. (2013). The 2008 eruption of Okmok Volcano, Alaska: Petrological and geochemical constraints on the subsurface magma plumbing system. *Journal of Volcanology and Geothermal Research*, *264*, 85-106.

Leat, P. T., & Larter, R. D. (2003). Intra-oceanic subduction systems: introduction. *Geological Society, London, Special Publications*, *219*(1), 1-17.

Lizarralde, D., Holbrook, W. S., McGeary, S., Bangs, N. L., & Diebold, J. B. (2002). Crustal construction of a volcanic arc, wide-angle seismic results from the western Alaska Peninsula. *Journal of Geophysical Research: Solid Earth*, *107*(B8).

Lu, Z., Masterlark, T., & Dzurisin, D. (2005). Interferometric synthetic aperture radar study of Okmok volcano, Alaska, 1992–2003: Magma supply dynamics and postemplacement lava flow deformation. *Journal of Geophysical Research: Solid Earth*, *110*(B2).

Lu, Z., & Dzurisin, D. (2010). Ground surface deformation patterns, magma supply, and magma storage at Okmok volcano, Alaska, from InSAR analysis: 2. Coeruptive deflation, July–August 2008. *Journal of Geophysical Research: Solid Earth*, *115*(B5).

Lu, Z., Dzurisin, D., Biggs, J., Wicks, C., & McNutt, S. (2010). Ground surface deformation patterns, magma supply, and magma storage at Okmok volcano, Alaska, from InSAR analysis: 1. Intereruption deformation, 1997–2008. *Journal of Geophysical Research: Solid Earth*, *115*(B5).

Mann, D., Freymueller, J., & Lu, Z. (2002). Deformation associated with the 1997 eruption of Okmok volcano, Alaska. *Journal of Geophysical Research: Solid Earth*, *107*(B4).

Marsh, B. D. (1979). Island arc development: Some observations, experiments, and speculations. *The Journal of Geology*, 687-713.

Masterlark, T., Haney, M., Dickinson, H., Fournier, T., & Searcy, C. (2010). Rheologic and structural controls on the deformation of Okmok volcano, Alaska: FEMs, InSAR, and ambient noise tomography. *Journal of Geophysical Research: Solid Earth*, *115*(B2).

Masterlark, T., Feigl, K. L., Haney, M., Stone, J., Thurber, C., & Ronchin, E. (2012). Nonlinear estimation of geometric parameters in FEMs of volcano deformation: Integrating tomography models and geodetic data for Okmok volcano, Alaska. *Journal of Geophysical Research: Solid Earth*, *117*(B2).

Miller, T. P., McGimsey, R. G., Richter, D. H., Riehle, J. R., Nye, C. J., Yount, M. E., & Dumoulin, J. A. (1998). Catalog of the historically active volcanoes of Alaska. *US Geological Survey Open-File Report*, 98-582.

Miyagi, Y., Freymueller, J. T., Kimata, F., Sato, T., & Mann, D. (2004). Surface deformation caused by shallow magmatic activity at Okmok volcano, Alaska, detected by GPS campaigns 2000–2002. *Earth, planets and space*, *56*(10), 29-32.

Nye, C.J. (1990). Okmok Caldera: eastern Aleutian Islands. *Wood, C.A., and Kienle, Jürgen, eds., Volcanoes of North America: Cambridge University Press*, 41–43.

Ohlendorf, S. J., Thurber, C. H., Pesicek, J. D., & Prejean, S. G. (2014). Seismicity and seismic structure at Okmok Volcano, Alaska. *Journal of Volcanology and Geothermal Research*, *278*, 103-119.

Patrick, M. R., Dehn, J., Papp, K. R., Lu, Z., Dean, K., Moxey, L., ... & Guritz, R. (2003). The 1997 eruption of Okmok Volcano, Alaska: a synthesis of remotely sensed imagery. *Journal of Volcanology and Geothermal Research*, *127*(1), 87-105.

Peacock, S. M. (1990). Fluid processes in subduction zones. *Science*, *248*(4953), 329-337.

Plafker, G., & Berg, H. C. (Eds.). (1994). The geology of Alaska.

Shillington, D. J., Van Avendonk, H. J., Holbrook, W. S., Kelemen, P. B., & Hornbach, M. J. (2004). Composition and structure of the central Aleutian island arc from arc‐parallel wide‐angle seismic data. *Geochemistry, Geophysics, Geosystems*, *5*(10).

Shillington, D. J., Van Avendonk, H. J., Behn, M. D., Kelemen, P. B., & Jagoutz, O. (2013). Constraints on the composition of the Aleutian arc lower crust from VP/VS. *Geophysical Research Letters*, *40*(11), 2579-2584.

van Keken, P. E. (2003). The structure and dynamics of the mantle wedge. *Earth and planetary science letters*, *215*(3), 323-338.

von Huene, R., & Scholl, D. W. (1991). Observations at convergent margins concerning sediment subduction, subduction erosion, and the growth of continental crust. *Reviews of Geophysics*, *29*(3), 279-316.

Worrall, D. M. (1991). Tectonic history of the Bering Sea and the evolution of Tertiary strike-slip basins of the Bering Shelf. *Geological Society of America Special Papers*, *257*, 1

Chapter 2

Introduction to the Magnetotelluric Method

The following sections are a brief review of MT theory. For an exhaustive review of the MT method and its implementation see Bahr (1988). The magnetotelluric method (MT) uses naturally-occurring electromagnetic fields of external origin to image the resistivity (or its inverse, conductivity) structure within the Earth. High frequency signal (greather than 1 Hz) comes from global lightning strikes. Energy produced by storms, primarily near the equator, travels in the non-conducting waveguide between the surface of the Earth and the ionosphere. Part of this energy also passes into the subsurface. Lower frequency electromagnetic signal comes from the interaction of charged particles from the sun, also known as solar wind, with Earth's geomagnetic field. Large-scale electrical currents are created in the ionosphere, with some of the energy propagating down to the subsurface. Because space weather is chaotic, the amplitude of the geomagnetic field will vary over a wide range of frequencies. This creates excellent signal for natural-source electromagnetic methods (see Figure 2.1).

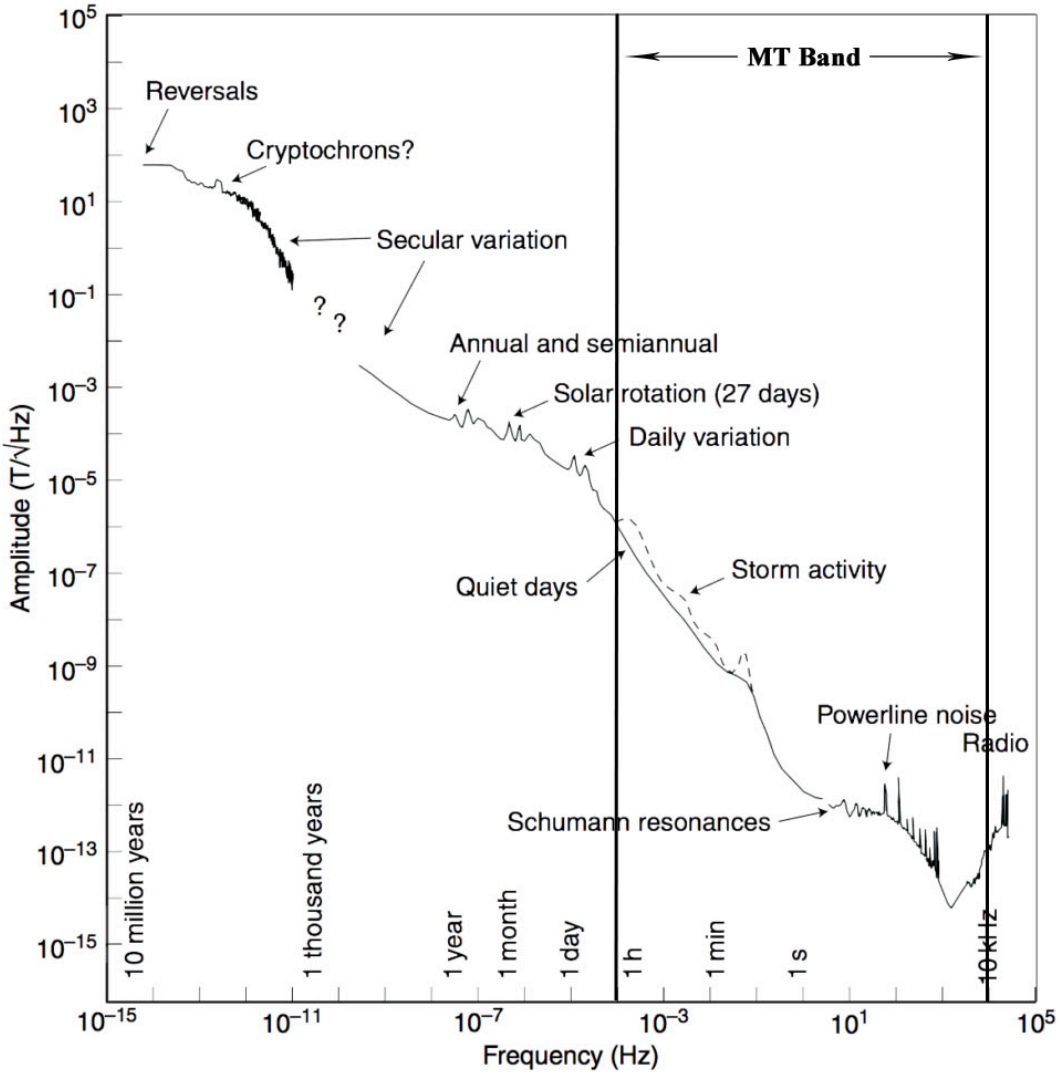

Figure 2.1: Amplitude spectrum of variations in the geomagnetic field. Modified from Constable and Constable (2004).

For both source types, it is assumed that the external energy reaches the surface as plane waves of random orientation and phases. Because the Earth is a good conductor and the air is not, these waves are refracted vertically downwards into the subsurface and generate electrical currents (also called telluric) there. These currents then induce secondary magnetic fields as the plane waves diffuse into the earth. The MT method measures small changes in the electric and magnetic fields at the surface or on the

seafloor. We can then relate these fields using transfer functions to deduce information about the resistivity structure in the subsurface.

Oceanic crust, such as what is subducted in the Aleutians, commonly consists of a layer of deposited sediment above a basaltic crust. Beneath the crust, the mantle is primarily peridotite. As shown in Figure 2.2, the resistivity of seawater is several orders of magnitude lower than that of basalt. Near surface, the resistivity is therefore highly dependent on fluid content and porosity. At greater depths, the lithosphere is effectively non-porous, and bulk resistivity in the mantle is driven more by the presence of partial melt and the water content of anhydrous minerals (*Yoshino and Katsura*, 2013).

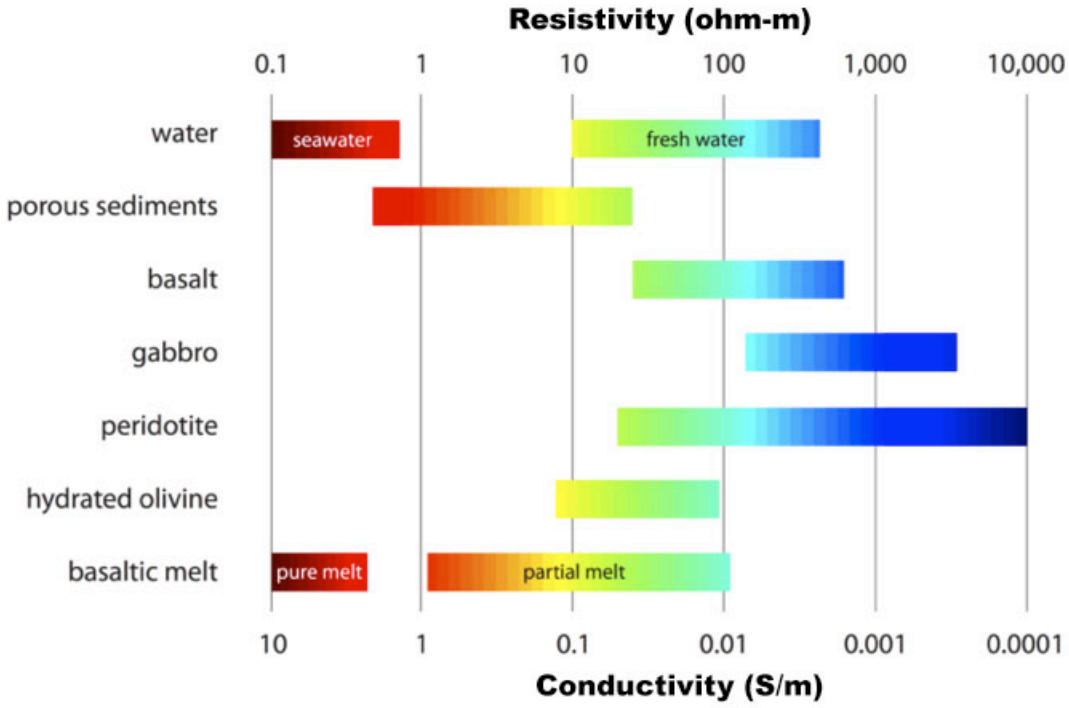

Figure 2.2: Electrical resistivities for common Earth materials. Modified from Naif (2015).

Offshore systems are typically investigated with seismic, thermal, geochemical, and bathymetric mapping, as well as drilling studies. Such work is often prohibitively

expensive or cannot uniquely image fluids in the subsurface across broad areas. The magnetotelluric method images electrical resistivity, which is highly dependent on porosity while being insensitive to mechanical properties (i.e. density and rheology). This makes the method an excellent complement to seismic methods in areas such as the Aleutians.

In recent years, MT has been used to successfully image fluid release and melt generation and transport in several areas of the world. Worzewski et al. (2011) used an amphibious MT profile to show several zones of fluid release associated with dehydration reactions on the down-going slab in Costa Rica. McGary et al. (2014) used spacing and wideband frequency range similar to our study to reveal fluid release on the slab as well as generation and transport of melt from the mantle to the shallow crust in Cascadia. Naif et al. (2013) used MT and controlled source electromagnetics to image fluid associated with subduction in Nicaragua.

2.1 Electromagnetic induction

A full review of electromagnetic induction can be found in Cagniard (1953) and Ward and Hohmann (1988). A brief overview will be given here. The magnetotelluric method is based on the relationships between electric and magnetic fields, which are described by Maxwell's equations as shown in Ward and Hohmann (1988). In particular, Faraday's law (Equation 2.1) and Ampere's law (Equation 2.2) are the fundamental governing equations upon which we develop the theory for MT:

$$\nabla \times \boldsymbol{E} = -\frac{\partial \boldsymbol{B}}{\partial t} \tag{2.1}$$

$$\nabla \times \boldsymbol{H} = \boldsymbol{J} + \frac{\partial \boldsymbol{D}}{\partial t} \tag{2.2}$$

For Faraday's law, **E** is electric field [V m^{-1}] and **B** is magnetic flux density [T]. This law shows that a time-varying magnetic field will induce a loop of current. In Ampere's law (Equation 2.2) we represent the magnetic field in [A m^{-1}] as **H**, the electric current density as **J** [A m^{-2}], and the displacement current density in [C m^{-2}] as **D**. Ampere's law describes that when an electric current is induced by a time-varying magnetic field it will in turn create a secondary magnetic field that is proportional to the total current density.

When Maxwell's equations are applied to earth materials, we must define constitutive equations as follows:

$$\boldsymbol{B} = \mu \boldsymbol{H} \tag{2.3}$$

$$\boldsymbol{J} = \sigma \boldsymbol{E} \tag{2.4}$$

$$\boldsymbol{D} = \varepsilon \boldsymbol{E} \tag{2.5}$$

where μ, σ, and ε are material properties that are time-invariant. We define μ to be the magnetic permeability with units [N A^{-2}], σ is the electric conductivity in [S m^{-1}], and ε is the electric permittivity in [F m^{-1}].

In order to demonstrate electromagnetic induction based on these fundamental equations we must make a series of assumptions, beginning with the quasistatic approximation. This means that we are assuming that displacement currents ($\frac{\partial \boldsymbol{D}}{\partial t}$) are much smaller than the electric current density (**J**) in equation (2.2). This simplifies Ampere's law to one term on the right-hand side. We can also substitute the constitutive equations (2.3) and (2.4) into the simplified Ampere's law, resulting in:

$$\nabla \times \boldsymbol{B} = \mu \sigma \boldsymbol{E} \tag{2.6}$$

We then take the curl of Faraday's law, equation (2.1), to get:

$$\nabla\times\nabla\times\boldsymbol{E} = -\frac{\partial}{\partial t}(\nabla\times\boldsymbol{B}) \tag{2.7}$$

At this point we will make use of the curl-curl vector identity:

$$\nabla\times\nabla\times\boldsymbol{A} = \nabla(\nabla\cdot\boldsymbol{A}) - \nabla^{\boldsymbol{2}}\boldsymbol{A} \tag{2.8}$$

Applying this to equation (2.7) results in:

$$\nabla\times\nabla\times\boldsymbol{E} = -\frac{\partial}{\partial t}(\nabla\times\boldsymbol{B}) = \nabla\cdot\nabla\cdot\boldsymbol{E} - \nabla^{\boldsymbol{2}}\boldsymbol{E} \tag{2.9}$$

We then make our next fundamental assumption, which is that there are no electric current sources inside the assumed homogeneous material:

$$\nabla\cdot\boldsymbol{E} = 0 \tag{2.10}$$

Substituting this into equation (2.9) yields:

$$\nabla\times\nabla\times\boldsymbol{E} = -\frac{\boldsymbol{\partial}}{\boldsymbol{\partial t}}(\nabla\times\boldsymbol{B}) = -\nabla^2\boldsymbol{E} \tag{2.11}$$

We can then substitute the modified Ampere's law in equation (2.6) into this equation (2.11). Recall that the material properties are time-invariant. This results in the equation:

$$\nabla^2\boldsymbol{E} = \mu\sigma\frac{\boldsymbol{\partial E}}{\boldsymbol{\partial t}} \tag{2.12}$$

We now follow these same steps, beginning with (2.6), taking the curl, using the curl-curl identity, and assuming a monopole (Gauss's law), to manipulate the magnetic field to reach the equation:

$$\nabla^2\boldsymbol{B} = \mu\sigma\frac{\boldsymbol{\partial B}}{\boldsymbol{\partial t}} \tag{2.13}$$

When taken together, equations (2.12) and (2.13) demonstrate that electromagnetic fields propagate diffusively, similar to how heat would flow through the subsurface. Recall that we have assumed a homogeneous region. If we were instead to assume an inhomogeneous region, these equations would become complicated by terms accounting for boundary charges. For simplicity's sake, we will maintain the homogeneous assumption.

We will next make the plane wave assumption. Applying this first to the magnetic field, we assume that the magnetic source is a periodic horizontally polarized plane wave. Mathematically this can be represented in harmonic form as:

$$\boldsymbol{B} = B_0 e^{i\omega t} \tag{2.14}$$

Applying this to the right side of equation (2.13) results in:

$$\nabla^2 \boldsymbol{B} = \mu\sigma i\omega \boldsymbol{B} \tag{2.15}$$

Making the same plane wave assumption for the electric field, and applying it to equation (2.12), gives us:

$$\nabla^2 \boldsymbol{E} = i\omega\mu\sigma \boldsymbol{E} \tag{2.16}$$

We now define the complex wavenumber k=$\sqrt{i\omega\mu\sigma}$. Substituting this into equations (2.15) and (2.16) yields:

$$\nabla^2 \boldsymbol{B} = k^2 \boldsymbol{B} \tag{2.17}$$

$$\nabla^2 \boldsymbol{E} = k^2 \boldsymbol{E} \tag{2.18}$$

We have already assumed that the source fields are vertically incident horizontally polarized plane waves. We have also assumed a homogeneous half-space. If we were to

expand out the left sides of equations (2.17) and (2.18), the derivatives with respect to x and y would fall out, leaving only a z term showing how fields attenuate with depth. Mathematically, the equations would simplify to:

$$\frac{\partial^2 \boldsymbol{E}}{\partial z^2} - k^2 \boldsymbol{E} = 0 \tag{2.19}$$

$$\frac{\partial^2 \boldsymbol{B}}{\partial z^2} - k^2 \boldsymbol{B} = 0 \tag{2.20}$$

These equations are homogeneous linear second-order differential equations, and so will have solutions with the form:

$$\boldsymbol{B}(z) = C_1 e^{kz} + C_2 e^{-ikz} \tag{2.21}$$

We split the complex wavenumber into its real and imaginary components using the definition of the square root of an imaginary number. This results in:

$$k = (1+i)\sqrt{\frac{\omega\mu\sigma}{2}} \tag{2.22}$$

We now define the real part of this complex wave number to be the skin depth, z_s:

$$z_s(\omega) = \sqrt{\frac{2}{\omega\mu\sigma}} \tag{2.23}$$

Equations (2.22) and (2.23) are then substituted into the characteristic solution (2.21). After some manipulation this gives:

$$\boldsymbol{B}(z) = C_1 z e^{z/z_s} e^{iz/z_s} + C_2 z e^{z/z_s} e^{-iz/z_s} \tag{2.24}$$

On the right hand side of this equation the first term accounts for up-going energy, while the second term accounts for energy going downwards. We know that electromagnetic fields decay with depth inside the earth, so C_1=0, and the first term goes to zero. We now use our boundary condition that at the surface (z=0) the magnetic field will be at full amplitude. The second unknown variable, C_2, will therefore be equal to

equation (2.14). This means that with our assumptions the full solution in a homogeneous half-space is:

$$\boldsymbol{B}(z,t) = B_0 e^{i\omega t} e^{-z(1+i)/z_s} \tag{2.25}$$

We substitute equation (2.25) back into equation (2.6). Keeping in mind that we are assuming a plane wave polarized in the x-direction, the curl will simplify to the derivative of B_x with respect to z in the $\hat{y}$ direction. After and solving for **E**, we get:

$$E_y = -B_0 \left(\frac{1+i}{\mu\sigma z_s}\right) e^{i\omega t} e^{-z(1+i)/z_s} \tag{2.26}$$

This shows that when we assume the inducing magnetic field is a plane wave polarized in the x-direction, the resulting electric currents are horizontal and flow perpendicular to the inducing magnetic field. We therefore measure electric and magnetic fields as orthogonal components in the MT method.

2.2 Skin depth

Different frequencies of electromagnetic fields are sensitive to resistivity structure at different depths in the Earth. Lower frequency fields penetrate deeper, while higher frequency fields attenuate near surface. We can define the skin depth, z_s, to be the depth at which amplitude is now 1/e (~37%) what it was at the surface. At this point the phase of the incoming field will have also shifted by one radian. More commonly, we state the skin depth is:

$$z_s(f) \approx 500 \left(\frac{1}{\sigma f}\right)^{1/2} \tag{2.27}$$

where σ is the conductivity of the material in S/m, and f is the frequency of the field. This relationship allows us to determine the maximum depth that a particular frequency will be sensitive to, assuming we have some knowledge of the conductivity structure.

2.3 Impedance tensor

By measuring the electric and magnetic fields in orthogonal directions in the time domain we can estimate the electrical conductivity of the subsurface as a function of depth using a frequency-dependent transfer function (*Tikhonov,* 1950; *Cagniard,* 1953). This transfer function takes the form:

$$Z_{xy}(\omega) = \frac{E_x}{H_y} \tag{2.28}$$

When the resistivity changes in two or three dimensions, this transfer function is more generally described using the impedance tensor

$$\boldsymbol{Z} = \begin{bmatrix} Z_{xx} & Z_{xy} \\ Z_{yx} & Z_{yy} \end{bmatrix} \tag{2.29}$$

where the impedance tensor represents the linear relationship between electric and magnetic fields:

$$\boldsymbol{E} = \boldsymbol{ZH} \tag{2.30}$$

For a 2D conductivity structure with strike direction x, the component Z_{xy} is referred to as the transverse electric (TE) mode. In this mode the electric field is parallel to the geoelectric strike, while the magnetic field is perpendicular. The value Z_{yx} is the transverse magnetic (TM) mode, where the magnetic field is parallel to strike and the

electric field is perpendicular. These modes are sensitive to different aspects of the electrical conductivity structure. In general, the TM mode is more sensitive to near-surface structures and lateral contacts, while TE may be more sensitive to deeper structure. The TM mode is generally considered to be less sensitive to 3D effects from conductive structures, while the TE mode is less sensitive to effects from 3D resistive features in the subsurface (*Berdichevsky* et al., 1998). This sensitivity to different features will be crucial for work with this data set, as 3D effects present a major challenge to modeling.

This impedance tensor is the starting point for much of the analysis of MT data sets, including the phase and apparent resistivity, swift skew, polarization grids, and phase tensors as discussed in Chapter 4.

2.4 References

Bahr, K. (1988), Interpretadon of the magnetotelluric impedance tensor: regional induction and local telluric distortion, Journal of Geophysics, 62, 119–127.

Berdichevsky, M. N., Dmitriev, V. I., & Pozdnjakova, E. E. (1998). On two-dimensional interpretation of magnetotelluric soundings. *Geophysical Journal International*, *133*(3), 585-606.

Cagniard, L. (1953). Basic theory of the magneto-telluric method of geophysical prospecting. *Geophysics*, *18*(3), 605-635.

Constable, C. G., & Constable, S. C. (2004). Satellite magnetic field measurements: applications in studying the deep earth. *The State of the Planet: Frontiers and Challenges in Geophysics*, 147-159.

Constable, S. (2013). Review paper: Instrumentation for marine magnetotelluric and controlled source electromagnetic sounding. *Geophysical Prospecting*, *61*(s1), 505-532.

McGary, R. S., Evans, R. L., Wannamaker, P. E., Elsenbeck, J., & Rondenay, S. (2014). Pathway from subducting slab to surface for melt and fluids beneath Mount Rainier. *Nature*, *511*(7509), 338-340.

Naif, S., Key, K., Constable, S., & Evans, R. L. (2013). Melt-rich channel observed at the lithosphere-asthenosphere boundary. *Nature*, *495*(7441), 356-359.

Naif, S. N. (2015). Marine electromagnetic experiment across the Nicaragua Trench: Imaging water-rich faults and melt-rich asthenosphere, Ph.D. dissertation, University of California San Diego.

Tikhonov, A. N. (1950, February). On determining electrical characteristics of the deep layers of the Earth's crust. In *Doklady* (Vol. 73, No. 2, pp. 295-297).

Ward, S. H., & Hohmann, G. W. (1988). Electromagnetic theory for geophysical applications. *Electromagnetic methods in applied geophysics*, *1*(3), 131-311.

Worzewski, T., Jegen, M., Kopp, H., Brasse, H., & Castillo, W. T. (2011). Magnetotelluric image of the fluid cycle in the Costa Rican subduction zone. *Nature Geoscience*, *4*(2), 108-111.

Yoshino, T., & Katsura, T. (2013). Electrical conductivity of mantle minerals: role of water in conductivity anomalies. *Annual review of earth and planetary sciences*, *41*, 605-628.

Chapter 3

Data Collection

In order to make MT measurements we record changes in the horizontal electric and magnetic fields in orthogonal directions. These measurements can be made onshore or along the seafloor with only a few changes to the fundamental design of the instruments. For this project seafloor receivers from the Marine EM Lab at Scripps were used to collect data at 54 stations offshore. Broadband and long period instruments from Scripps and the US Geological Survey were also used at 29 sites onshore both in and around the caldera, and 13 onshore temporary broadband seismometers from the IRIS PASSCAL Instrumentation Center were installed to supplement the permanent network of seismometers on the island.

3.1 MT instrumentation

In both onshore and offshore environments, the magnetotelluric method relies on time series measurements of electric and magnetic fields (see illustration in Figure 3.1). Measurements of each field type are made in two orthogonal directions, meaning that four channels of data are collected (Ex, Ey, Hx,Hy). Onshore, the vertical Hz is also generally measured. In the marine environment, only the horizontal components are

recorded since the vertical component data is not as valuable as horizontal data and the added cost in money and weight for the vertical component is not deemed worthwhile.

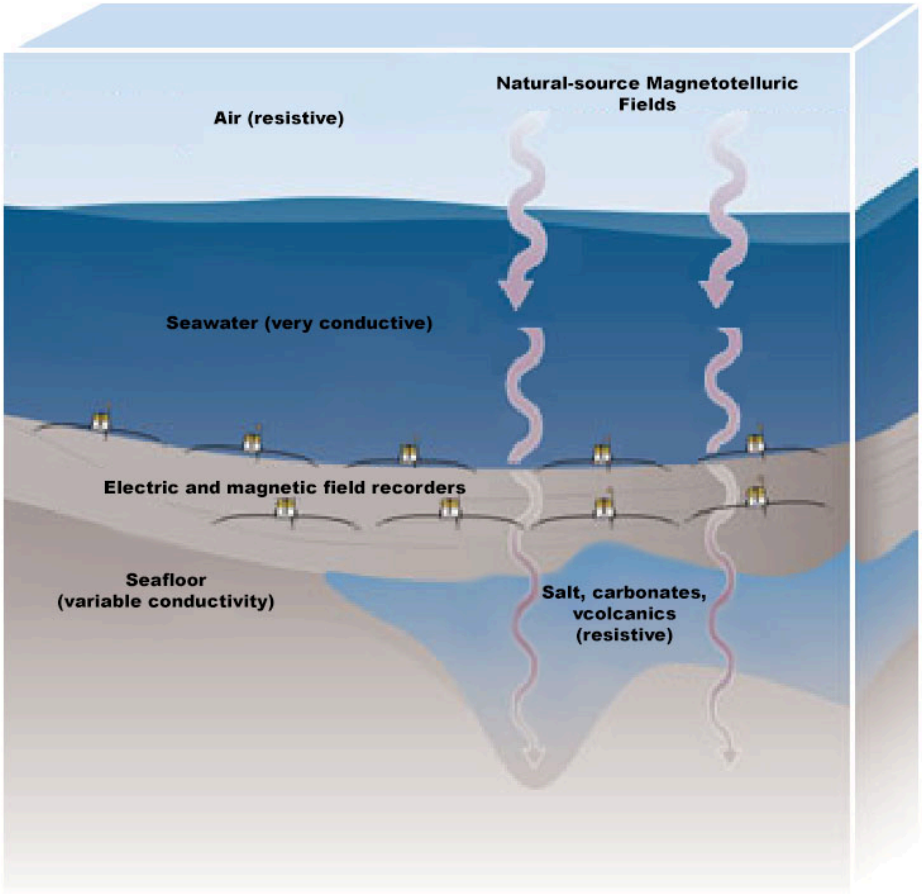

Figure 3.1: Illustration of the marine MT concept. Seafloor receivers make time series measurements of the naturally varying electric and magnetic fields. These measurements can then be used to infer information about subsurface resistivity, and through that we can begin to constrain the geology. Modified from Constable (2013).

In general, there are two classes of magnetotelluric systems. Long-period instruments are capable of measuring lower frequencies in the band 0.00001 to about 0.05 Hz, and therefore can be used to resolve deeper resistivity structure. Because lower frequencies are being measured, deployments must be significantly longer, with

instruments sometimes being left in place for up to a year. In order to measure magnetic fields at these low frequencies, fluxgate magnetometers are used.

The seafloor receivers made and used at Scripps Institution of Oceanography fall into the broadband class of instruments (see Figure 3.2). These instruments measure higher frequencies, and so constrain shallower features. Broadband instruments can be deployed for significantly less time, with onshore instruments often remaining in place for only a night or two. These higher-frequency instruments use induction coil magnetometers rather than fluxgate magnetometers. An induction coil magnetometer consists of a ferromagnetic core with wire wrapped around the length of it. As time-varying magnetic fields pass across the magnetometer, a voltage is induced in the wire and recorded.

The electric field measurements are made using what is essentially an oversized multimeter. For each electric dipole two Ag-AgCl electrodes are separated some distance in order to increase the signal-to-noise ratio. For seafloor receivers, the electrode separation is 10 m, while onshore each dipole can be up to 100 m long. The potential difference between the two electrodes is measured.

While the basic principles are the same for both onshore and marine instruments (measuring electric and magnetic fields in two orthogonal directions), there are many complexities to working in the marine environment that require specialized engineering. Any marine instrument must be self-contained, capable of accurately measuring time without access to GPS, and of appropriate weight and material to be stable on the seafloor, recoverable, and resistant to corrosion. The broadband seafloor receivers used by Scripps for this project are the third iteration of ocean-bottom receivers designed and

built by the Marine EM Lab at Scripps Institution of Oceanography. Full details of the instruments can be found in Constable (2013), but an overview of components will be given here.

As already mentioned, Ag-AgCl electrodes are used in the marine environment to measure changes in the electric field. The magnetic field is measured using induction coil magnetometers similar to what would be used onshore. The marine variation, however, uses aluminum wire wrapped around mu-metal alloy to reduce the weight of the instrument. Weight is a major factor in marine work, and requires careful calculations in advance of instrument deployment. Concrete slabs are attached to the instrument prior to deployment to ensure that the system rests stably on the seafloor. During recovery acoustic pings are sent from the ship to the acoustic transponder on the system. The correct sequence triggers a small voltage across a burn wire attached to the concrete block. This small amount of electricity speeds corrosion of the wire, and within minutes the instrument is free of the concrete. A secondary burn wire is also on the system to allow for recovery if the primary burn wire fails. Once the instrument is separated from the concrete it rises to the surface due to the buoyancy of four glass spheres in the yellow hardhat on the top of the system.

Electronics for the system, including amplifiers and the data logger, as well as all batteries, are contained in an aluminum alloy pressure case. The pressure case is anodized to protect from corrosion, which would add significant electric noise. Instruments are typically prepped in a warm lab environment onboard the boat. The seafloor is cold, and so if caution is not taken condensation within the cylinder can impact electronics. To prevent this, desiccant is placed in the cylinder and the humid air

is replaced with ambient air passed through additional desiccant. All components have been designed to be as energy efficient as possible, since batteries are one of the heaviest portions of the system.

Because the instrument drifts through the water column and lands on the seafloor in an arbitrary position we must have a way to measure orientation and pitch. In the third iteration of the Scripps system this is achieved with an electronic compass and tiltmeter attached to the frame as far as possible from the magnetometers to reduce bias from their magnetized cores. The compass remains active for 24 hours after deployment typically, making measurements every 30 minutes. Figure 3.2 shows a modern Scripps EM seafloor receiver, with major components discussed in this section highlighted.

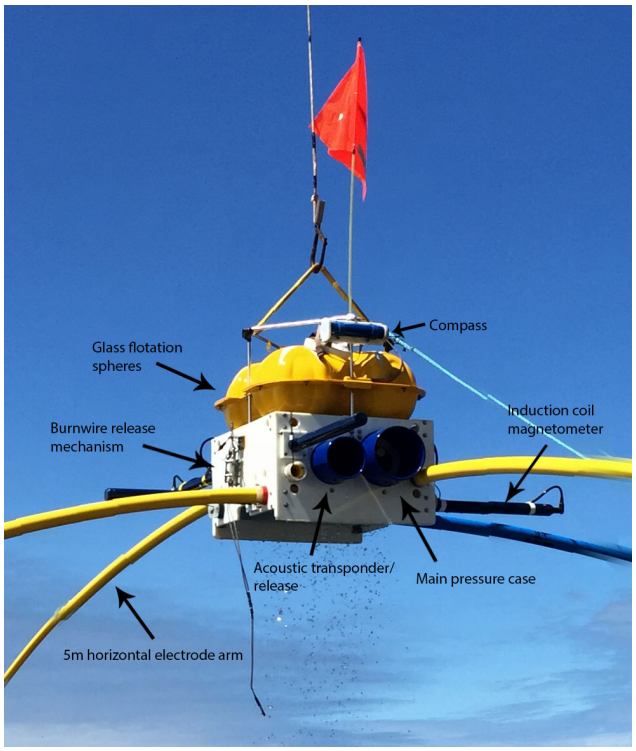

Figure 3.2: Third iteration marine electromagnetic seafloor receiver being recovered. The concrete slab has already been released.

3.2 Survey design

In order to constrain the resistivity structure throughout the magmatic system MT instruments were deployed both onshore and offshore. Twenty-nine closely spaced onshore receivers in and around the caldera will be used to image shallow crustal features, including the shallow magma bodies indicated by previous seismic and geodetic surveys of the volcano. Deeper, more regional features can be imaged using the profile of marine MT receivers running perpendicular to the subduction zone from the forearc into the backarc. Station spacing in the distant forearc and backarc was larger, in the range of 10 km, while closer to the island the spacing decreased to approximately 5 km. A ring of marine instruments roughly 13 km apart around the volcano in shallow water will also be used to constrain the magmatic system. Fifty-four marine instruments were deployed. The instrument at one shallow ring site (R09) was not recovered, giving a total of 53 marine MT sites. Figure 3.3 shows the locations of magnetotelluric instruments used in this project, both onshore and offshore. This thesis uses only the marine data. Future work will incorporate the onshore data to give a complete view of the magmatic system, from fluids being released along the subducting slab to shallow crustal magma storage. A brief overview of the fieldwork will now be given, with emphasis on the marine portion.

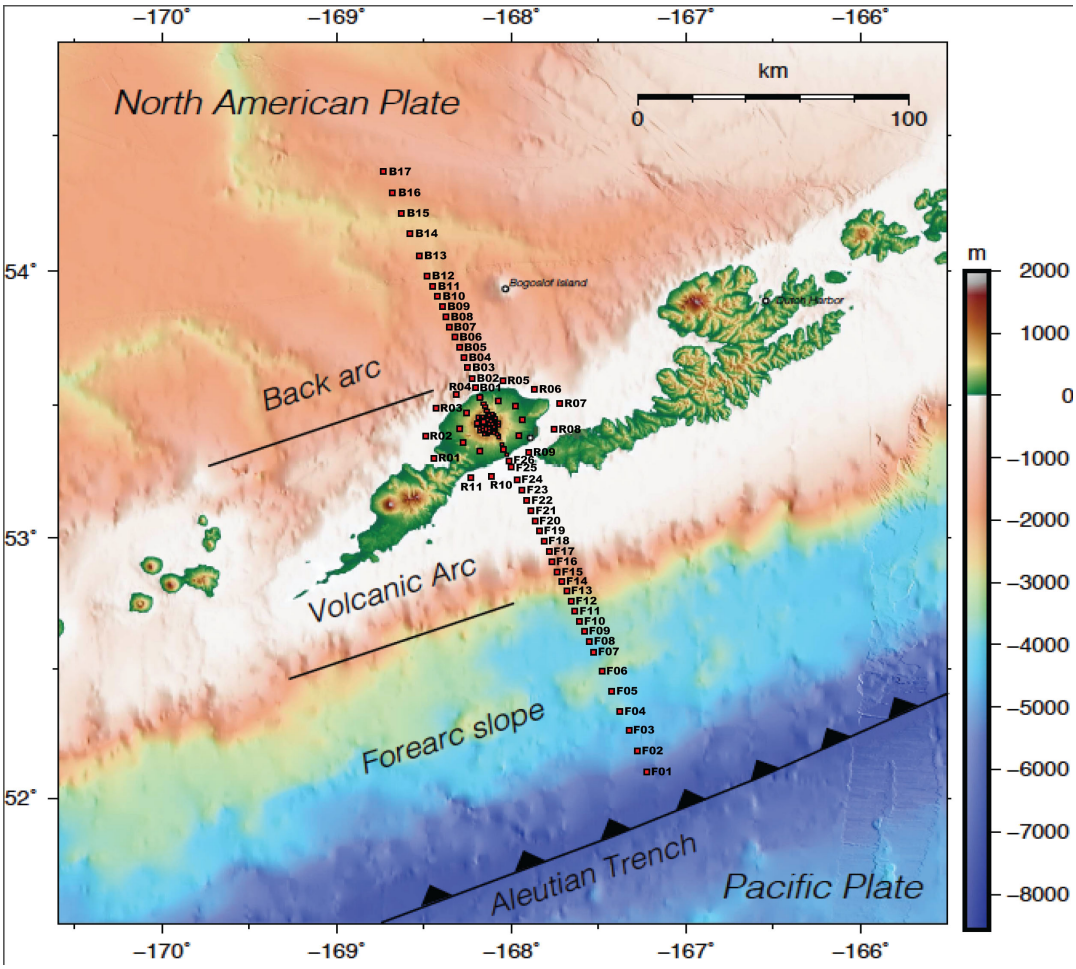

Figure 3.3: MT stations collected during summer 2015.

3.3 Deployment cruise

Seafloor receivers were deployed from the R/V Thomas G. Thompson between June 18, 2015, and June 21, 2015. As discussed in the previous section, the MT receivers were arranged in a 2D profile crossing from the forearc to the backarc to target deeper features including melt originating along the subducting slab and dehydration of sediments. Several of the receivers were also arranged in a ring around the island to constrain deeper features immediately around the volcano. In total, 54 seafloor instruments were deployed during this cruise. It was noted on deployment that twelve

instruments did not have fully operational stray lines. In eleven of these cases, the stray lines had flashing LEDs only, and did not have a functional GPS. In the case of station F25 the stray line did not have a GPS or functioning LEDs. The majority of these instruments were at shallow sites immediately surrounding the volcano. Sites located in Umnak Pass (sites R07-R09) were noted to be in an area with extremely strong surface currents. After all instruments had been deployed the ship returned to Dutch Harbor. All members of the science party for this cruise were from Scripps.

Figure 3.4: Marine EM Lab seafloor receiver being deployed from the deck of the R/V Thomas G. Thompson. Image courtesy of Kerry Key.

3.4 Onshore data collection

Following the deployment cruise Kerry Key and Georgianna Zelenak from SIO traveled to Umnak Island to join collaborators from the USGS, University of Wisconsin Madison, and AVO for collection of onshore MT and seismic data. The onshore portion of this project lasted from June 20 to July 11, 2015. All work was based out of Fort Glenn, a former military base and current cattle ranch on the slopes of Okmok. The fascinating history of Fort Glenn can be found in appendix 1 of this thesis. Throughout the onshore fieldwork helicopters were used to access remote sites both in and around the caldera. A wide range of unexpected hazards, from quicksand to feral bulls to sudden storms, was encountered. However, by the end of the onshore portion of the fieldwork data had been collected at 29 MT stations and 13 temporary broadband seismometers had been installed.

Figure 3.5: Base camp at Fort Glenn as seen from the helicopter. Image courtesy of Kerry Key.

The MT sites included both long-period and broadband instrumentation. After processing and inversion this should yield information about the resistivity structure both in the shallow crust directly beneath the caldera and in deeper regions beneath the volcano. Figure 3.6 shows one of the broadband instruments within the caldera. In general broadband instruments were left in the field for 1-3 days. At least two sites were deployed at all times to allow for remote referencing.

In addition to the magnetotelluric stations, 13 temporary broadband seismometers were installed to supplement the permanent seismic network operated by AVO. These instruments remained in the field for one year, and were recovered during the summer of 2016. The data set from these instruments will help better constrain near-surface velocity structure. Eventually, a joint inversion of the magnetotelluric and seismic data sets will be possible, giving an unprecedented look at the structure of an active volcano.

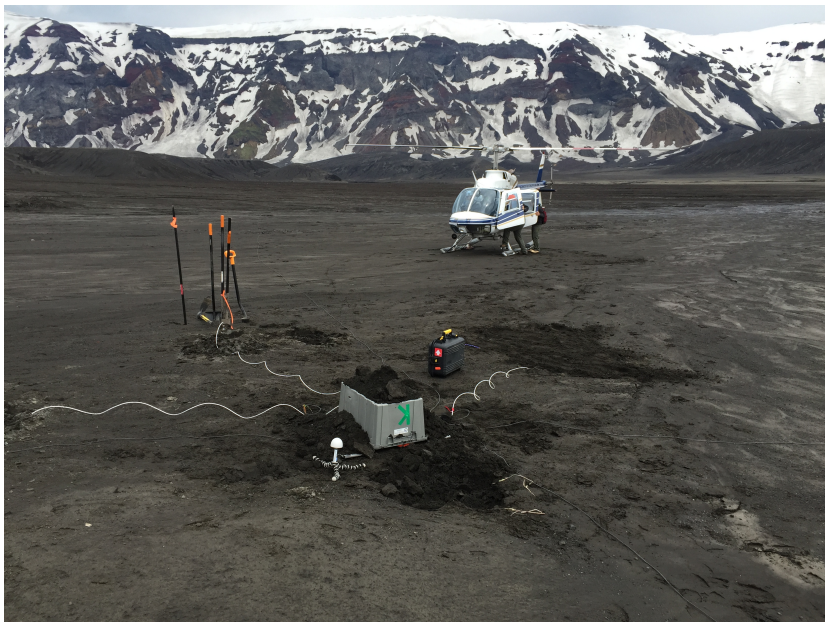

Figure 3.6: Broadband MT station deployed in the caldera. Image courtesy of Kerry Key.

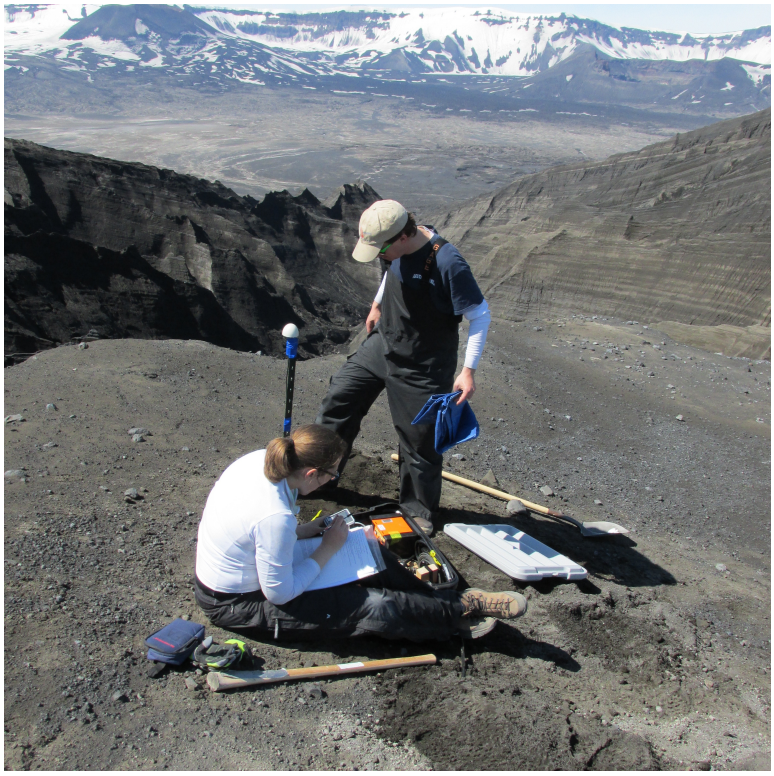

Figure 3.7: Collaborators Ninfa Bennington and Matt Haney install a temporary broadband seismometer on the narrow tephra ridge running between Cone D and Ahmnalix. Image courtesy of Summer Ohlendorf.

3.5 Recovery cruise

Following the onshore work, the two members of the Scripps party on the island were transported to the new icebreaker R/V Sikuliaq via small boat. All other members of the Marine EM Lab involved in the project met the boat in Dutch Harbor. The recovery cruise ran from July 9 to July 14, 2015.

Figure 3.8: Instrument recovery onboard the R/V Sikuliaq, with Umnak Island in the background. Image courtesy of Kerry Key.

In total, 53 of the 54 deployed instruments were recovered, giving a 98% success rate. The only instrument not recovered was R09, a shallow-water site located in the middle of Umnak Pass. Initially when attempts were made to communicate with this instrument no acoustic responses were received. The cruise therefore continued, and all other instruments were recovered. On the way back to Dutch Harbor we passed in the vicinity of R09 again, and attempts were made to communicate with the instrument. Acoustic pings from the instrument were received 2.5 km from where the site had been deployed. This reinforces that there were extremely strong currents in the area, as the instrument and its heavy concrete anchor were shifted incredible distances. Once the instrument was located the release command was sent. Shortly after all acoustic signals from the instrument were lost. The ship remained on site for quite a while searching for the instrument on the surface. However, sunrise led to significant glare at the surface,

and this instrument was one that had been deployed without a GPS system. It is also quite likely that the flag was snapped off the frame as the instrument was moved along the seafloor. The surface currents were also very strong at the time, with rip currents visible around the ship. Ultimately the instrument was not located.

Several other sites were noted to have damage upon recovery. Station F17, for example, had noticeably bent electrode arms as shown in Figure 3.9. It is quite likely that this damage occurred during instrument recovery, but it is possible that the arms were bent on the seafloor. This station also had a cracked hardhat over the glass balls on recovery. Other instruments also sustained bent arms or had compasses lost during the recovery process. Overall, though, a success rate of 98% recovery is exceptional for the conditions encountered during the work and the lack of fully functional stray lines.

Figure 3.9: Bent electrode arms on station F17. Image courtesy of Kerry Key.

3.6 References

Constable, S. (2013). Review paper: Instrumentation for marine magnetotelluric and controlled source electromagnetic sounding. *Geophysical Prospecting*, *61*(s1), 505-532.

Chapter 4

Magnetotelluric Data Analysis

Prior to doing any forward modeling or inversion we can manipulate the impedance tensor to elucidate information about trends and dimensionality of the data set. Specifically we can use apparent resistivity and phase, swift skew, polarization grids, and phase tensor analysis to learn more about the data set and subsurface trends prior to moving on to more computationally expensive methods of manipulation.

4.1 Apparent resistivity and phase

The impedance tensor can be used to calculate apparent resistivity, or the bulk volume average of resistivity, according to the equation:

$$\rho_{\boldsymbol{a}}(\omega) = \frac{1}{\mu\omega}|Z(\omega)|^2 \tag{4.1}$$

The impedance tensor is also used to calculate the phase:

$$\phi = arg\frac{Im(Z)}{Re(Z)} \tag{4.2}$$

Figure 4.1 shows apparent resistivity across all stations as a function of frequency after all sites have been rotated to the survey strike. Note that sites R05 and F06 have been excluded, despite the instruments at these stations being recovered. Station F06 had

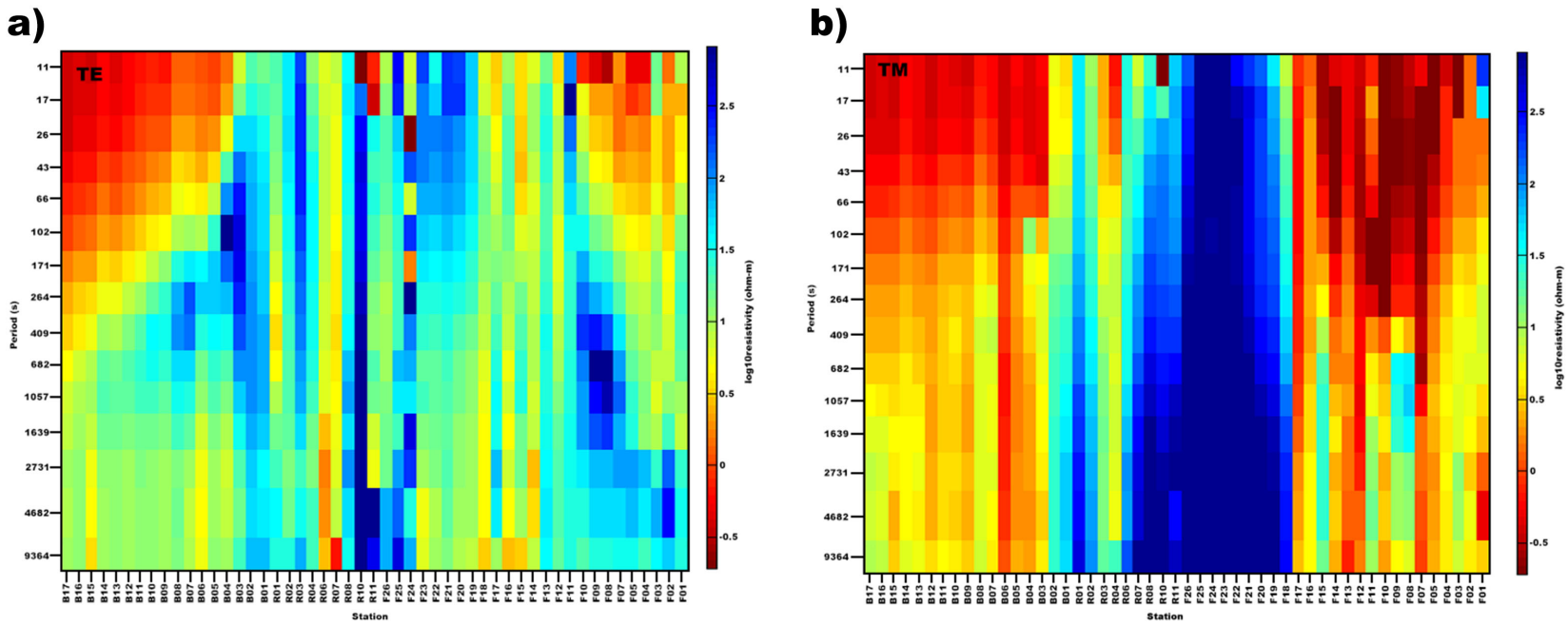

Figure 4.1: Apparent resistivities in a) TE mode and b) TM mode across all sites as a function of frequency.

a faulty channel, and there was a calibration issue for one of the magnetometers used at station R05. Station F17 is included in these figures, although it was noted on recovery of the instrument that the electrode arms were bent. Figure 4.2 shows the locations of these stations.

Figure 4.3 shows the phase across all stations as a function of frequency. This figure is quite remarkable, as it shows values wrapping from -180° to 180° in both the TE and TM modes. This is previously unheard of in data collected by the Marine EM Lab. Negative TE mode phases have previously been observed, most notably offshore northeastern Japan (*Key and Constable,* 2010). In the survey off Japan, the TE wrapping was attributed to the coast effect, where bathymetric changes and sharp boundaries between conductive ocean and resistive seafloor cause curvature of the diffusing electromagnetic field. The bathymetric changes in the Aleutians are more extreme than in Japan. It is plausible that the wrapping in both modes is therefore due to the more complicated and rugged bathymetry in this region along with possible inductive coupling with heterogeneous magmatic systems beneath the arc. The effect of the regional bathymetry and island topography will be tested in the forward modeling portion of this thesis.

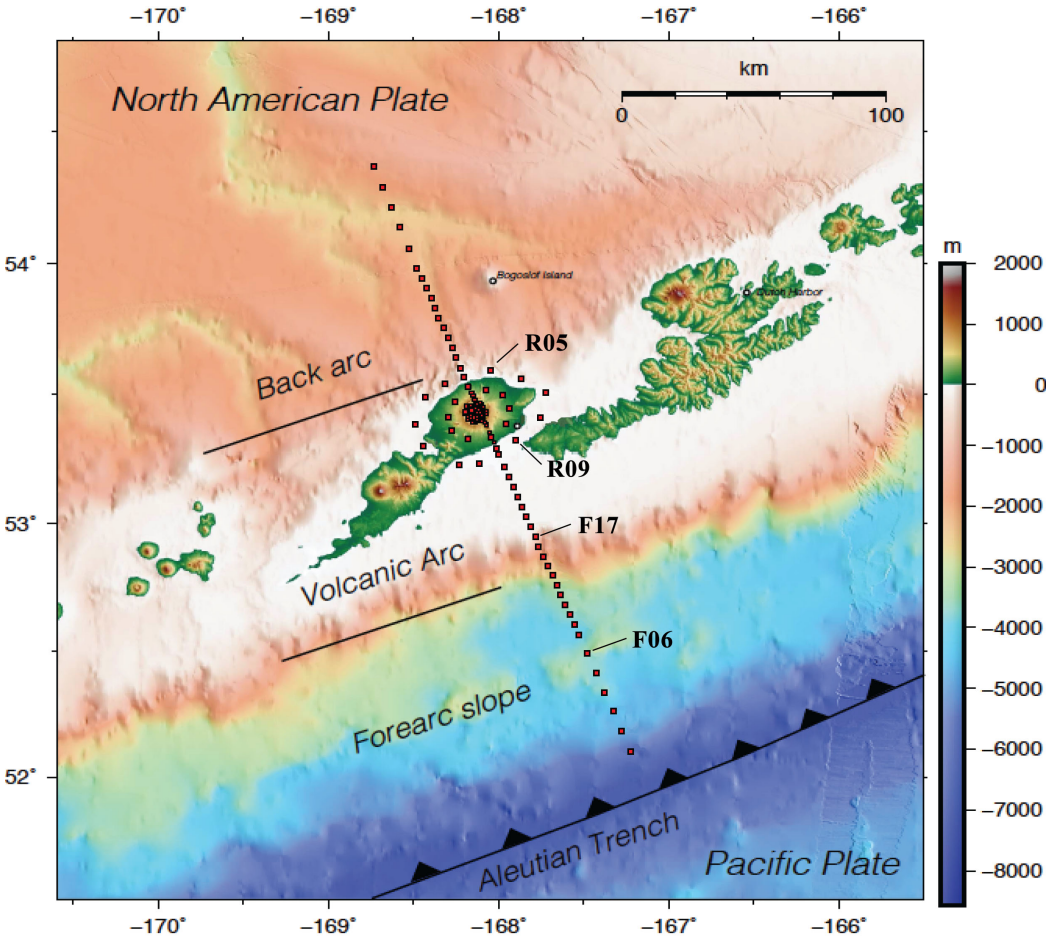

Figure 4.2: Locations of sites with known issues prior to processing.

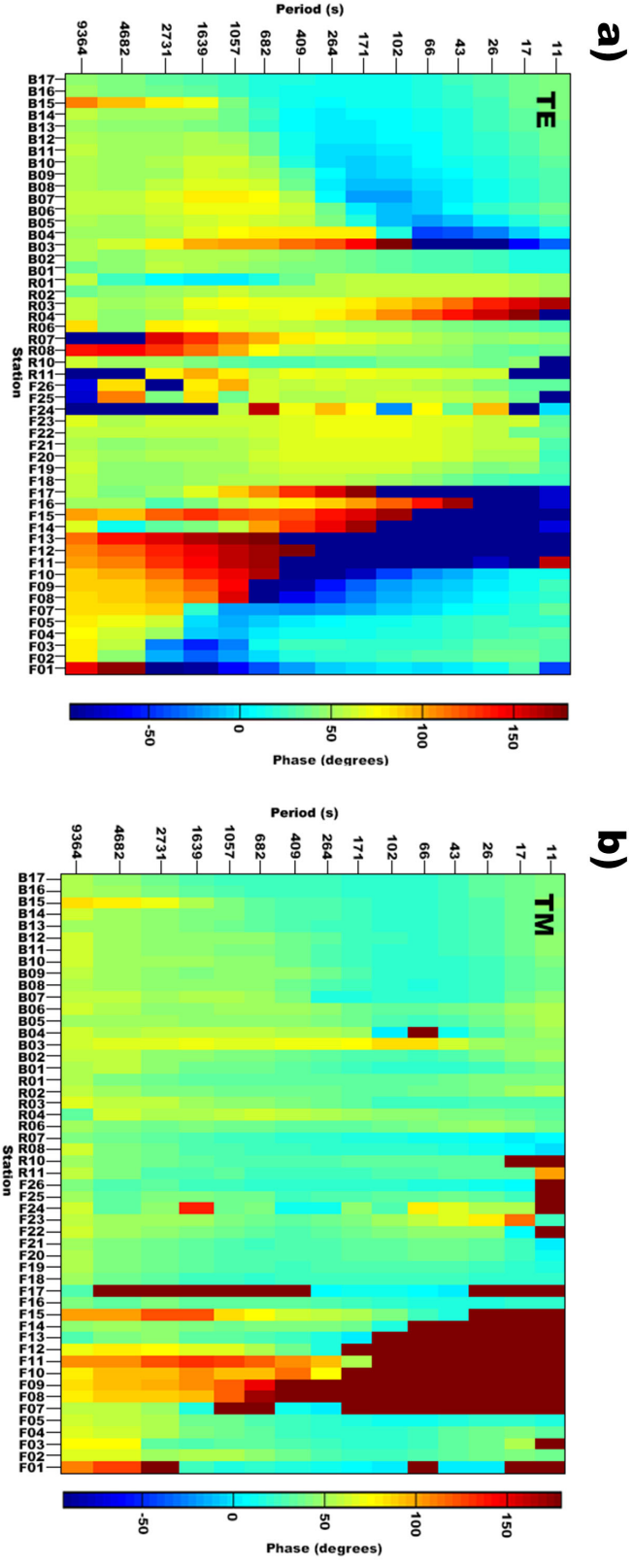

Figure 4.3: Phases for a) TE mode and b) TM mode across all sites as a function of frequency.

4.2 Swift skew

The dimensionality of the data set as a function of frequency can be determined in part using the Swift skew, which is the quotient of the trace and anti-trace of the impedance tensor:

$$S_s = \left|\frac{Z_{xx}+Z_{yy}}{Z_{xy}-Z_{yx}}\right| \tag{4.3}$$

This value is independent of rotation (*Swift*, 1967). We define that a Swift skew value over 0.2 indicates outright 3D structure, while values below 0.2 are either noisy 1D or 2D structure. Note that this definition of dimensionality is highly subjective and while presence of a large skew definitely indicates 3D structure, the absence of a large skew does not necessarily imply a lack of 3D structure.

Figure 4.4 shows the swift skew for the marine magnetotelluric data of this project. In this plot the deeper blues show low skew, below 0.2, and therefore indicate 1D or 2D structure. The warm colors indicate 3D structure. As we move from the distant backarc towards the volcanic center (site B17 progressing towards B01), we can see a predominantly 1D or 2D environment in the short periods where sensitivity is primarily in the near surface, with more complex 3D features at longer periods sensitive to deeper structure. The large skew implying 3D structure appears at shorter periods closer to the volcano, implying 3D conductivity at shallower depths. This is probably due to complicated features in the mantle and in the magmatic system beneath the volcano and could, for example, possibly indicate along strike variations in the magma supply beneath the volcano. The sites in a ring around the volcano (R01-R11) do not show as clear of a trend. These stations were in shallow water, and in general were noisier than deeper-

water sites. Shallow sites in the forearc, near the volcano (F26-F18) have lower swift skew values, again indicating less complex structure or possibly from some overprint on the MT fields from the thin conductive ocean on the shelf (less than 50 m), although further research is necessary to understand the dramatic shift to very low skews on the shelf. The sudden change in skew between sites F18 and F17 corresponds to the shelf break, with sites F17-F01 being in deeper water. As we saw in the backarc, the deeper forearc sites (F17-F01) have simple 1D or 2D structure overlying more complex 3D structure at depth.

The swift skew cannot distinguish between 1D and 2D structure. It also cannot distinguish symmetrical 3D, as the trace would be zero in this case. Polar diagrams are often used in conjunction with swift skew to evaluate dimensionality, as they can distinguish 3D data more clearly.

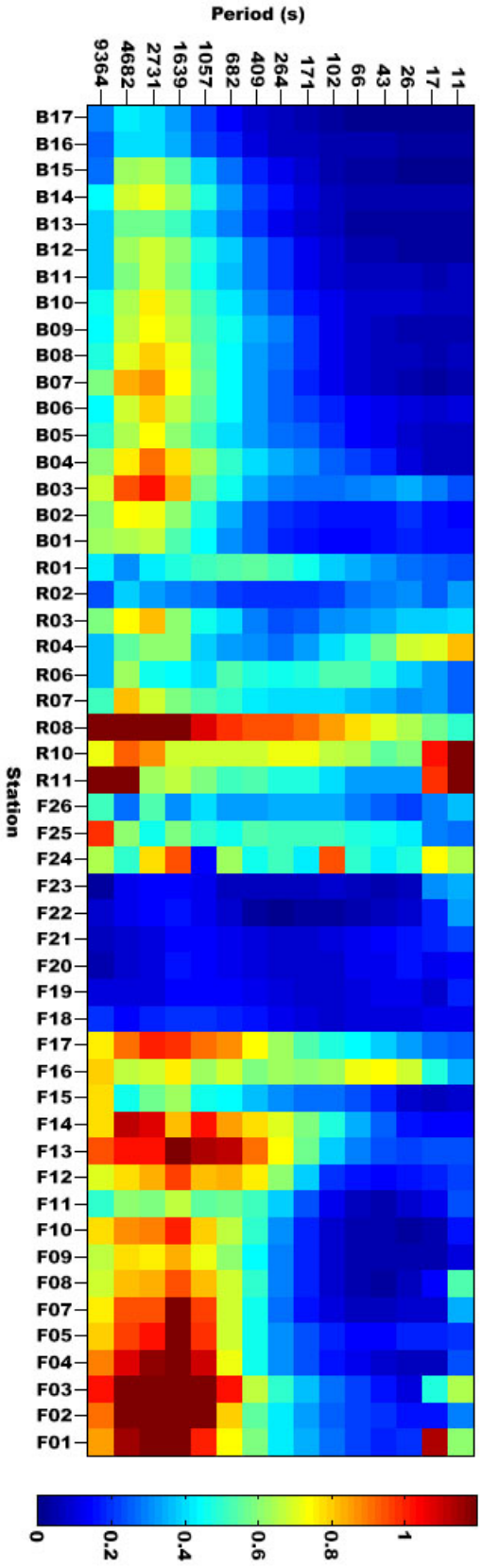

Figure 4.4: Swift skew across the marine MT stations as a function of period. Values above 0.2 are considered 3D.

4.3 Impedance polar diagrams

It is possible to elucidate information about the dimensionality of the Earth structure based solely on the impedance tensor. For 1D electrical structure, the diagonal components of the tensor will be zero, while the off-diagonals will be equal with opposite signs:

$$\boldsymbol{Z} = \begin{bmatrix} 0 & Z_{xy} \\ -Z_{xy} & 0 \end{bmatrix} \tag{4.4}$$

In a real-world environment, there will always be some noise, so the diagonals will just be close to zero, and the off-diagonals will have nearly equal values.

For 2D conductivity structure, we must consider the relative strike angle (ζ) between the underlying resistivity structure and the strike of the field measurements. When the relative strike is not parallel or perpendicular, the diagonal components of the impedance tensor will be equal and opposite values, while the off-diagonals will have different magnitudes. When the relative strike is parallel or perpendicular, the diagonals will be zero and the off-diagonals will have different values:

$$\boldsymbol{Z} = \begin{bmatrix} Z_{xx} & Z_{xy} \\ Z_{yx} & -Z_{xx} \end{bmatrix} \qquad \{\zeta \neq 0°, 90°\} \tag{4.5}$$

$$\boldsymbol{Z} = \begin{bmatrix} 0 & Z_{xy} \\ Z_{yx} & 0 \end{bmatrix} \qquad \{\zeta = 0°, 90°\} \tag{4.6}$$

If the conductivity structure is 3D, all components of the tensor can take any value regardless of strike:

$$\boldsymbol{Z} = \begin{bmatrix} Z_{xx} & Z_{xy} \\ Z_{yx} & Z_{yy} \end{bmatrix} \qquad \{0° \leq \zeta \leq 90°\} \tag{4.7}$$

As we rotate the tensor to different relative strike values, we can trace out how the diagonal and off-diagonal values are changing in order to visually determine if data is 1D, 2D, or 3D. See Figure 4.5 for a summary that shows examples of how the polar diagrams may appear for 1D, 2D and 3D structures.

Figure 4.6 shows the polarization plots for all of the marine magnetotelluric stations collected during this survey. In general, the trends seen in this figure are complimentary to the dimensionality indicated by the Swift skew. In the distant backarc (around station B17) the polarizations indicate 1D structure near the surface. At depth, and closer to the volcano, structure becomes more 2D and 3D. The polarization plots are also in agreement with the skew in that there is simpler structure (1D and 2D) for the forearc sites on the shelf (F23-F18).

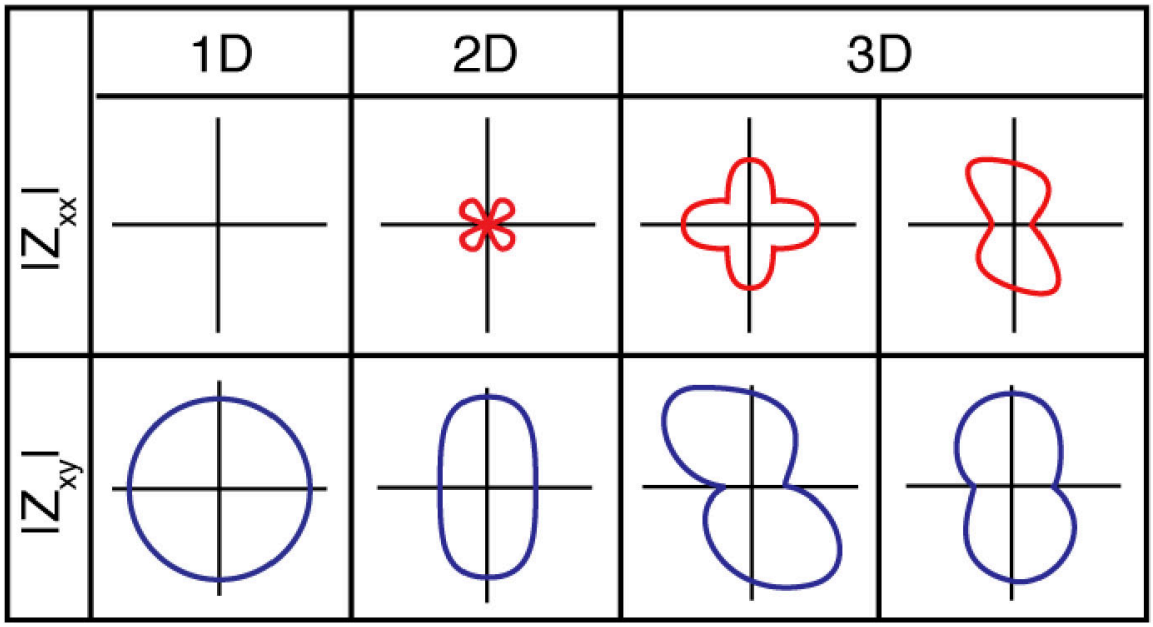

Figure 4.5: Diagonal and off-diagonal components of the rotated impedance tensor for the 1D, 2D, and 3D case. Modified from Naif (2015).

Where there are near-surface conductivity heterogeneities the MT regional response becomes distorted in what is called galvanic distortion. Polarization plots do

not remove these galvanic distortions, and so if there is near-surface heterogeneity the overall interpretation can be inaccurate. In the marine environment, it is generally assumed that the near-surface sediments are homogeneous. It is therefore appropriate to use polarization plots to determine dimensionality. However, it is also worthwhile to examine phase tensors, which display similar information while removing galvanic distortion from the regional response.

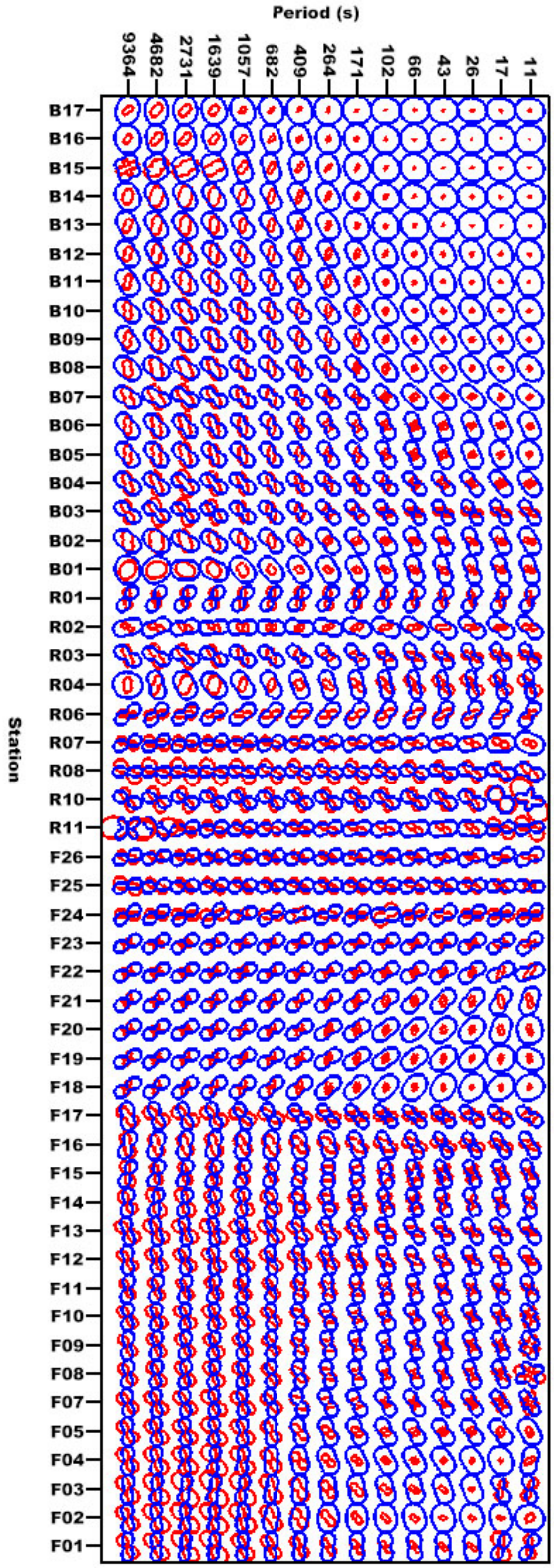

Figure 4.6: Polarization plots as a function of period for the marine magnetotelluric stations.

4.4 Phase tensors

The phase tensor is defined as:

$$\boldsymbol{\Phi} = \boldsymbol{X}^{-1}\boldsymbol{Y} = \begin{bmatrix} \Phi_{xx} & \Phi_{xy} \\ \Phi_{yx} & \Phi_{yy} \end{bmatrix} \tag{4.8}$$

where **X** and **Y** are the real and imaginary parts of the impedance tensor (*Caldwell et al.,* 2004). In most onshore surveys the phase tensor is preferable to the impedance tensor for determining dimensionality, as it is independent of galvanic distortion. This can be demonstrated by considering a distortion tensor, **D**. If we apply a distortion to the impedance tensor, the results would be:

$$\boldsymbol{Z}_D = \boldsymbol{DZ} = \boldsymbol{DX} + \boldsymbol{D}(i\boldsymbol{Y}) \tag{4.9}$$

Clearly in this case the distortion has not been canceled out, and it will therefore be in the polarization plots. If we apply the same distortion tensor to the phase tensor, the results will be:

$$\boldsymbol{\Phi}_D = \boldsymbol{DX}^{-1}\boldsymbol{DY} = \boldsymbol{X}^{-1}\boldsymbol{D}^{-1}\boldsymbol{DY} = \boldsymbol{\Phi} \tag{4.10}$$

This means that the phase tensor is independent of near-surface effects such as galvanic distortion. More detailed information on the phase tensor can be found in Caldwell et al. (2004).

Because the phase tensor is real-valued, it is possible to rotate it about a unit circle and plot the resulting ellipse. Figure 4.7 shows such phase tensor ellipses for the different marine MT stations as a function of period. The color in the ellipses corresponds to the phase tensor skew angle, β, where:

$$\beta = \frac{1}{2} tan^{-1}\left(\frac{\Phi_{12}-\Phi_{21}}{\Phi_{11}+\Phi_{22}}\right) \tag{4.11}$$

This value is a rotation away from the regional strike, and is a measure of the tensor's asymmetry. In general, over 1D resistivity structure the phase tensor ellipse will appear as a circle, with β close to zero. Two-dimensional structure will be an ellipse with principle axes of different lengths, with β still near zero. Three-dimensional structure will have principle axes of different lengths and non-zero fill.

Figure 4.7 shows the phase tensors for the marine MT sites associated with this project. As seen with the polarization plots and swift skew, the structure in the far backarc (station B17) is primarily 1D, with stations throughout the backarc becoming more complex with depth and towards the volcanic center. The dimensionality from the phase tensors is also consistent with the polarizations and skew in that the shallow forearc sites on the shelf are two dimensional, with a sharp break in dimensionality at the shelf's edge near site F17. Deeper sites beyond site F17 are again much more complex, with 2D and 3D structure.

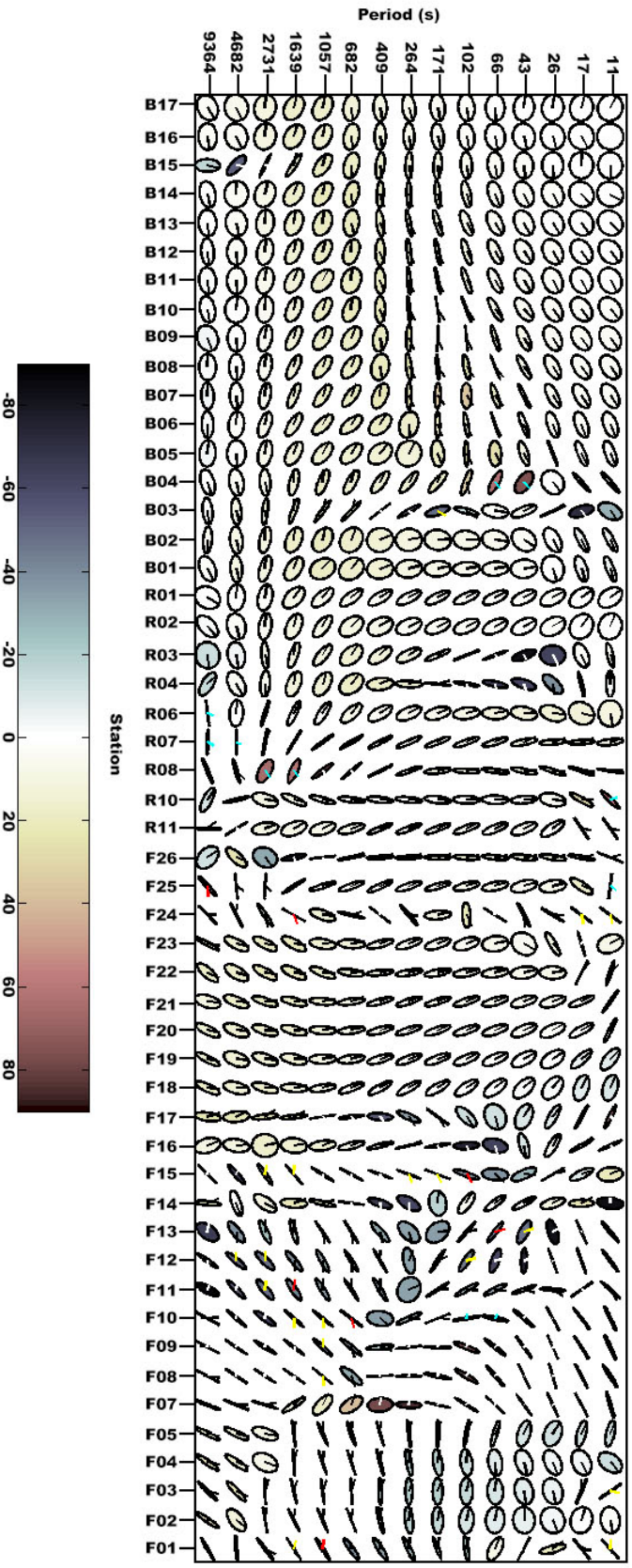

Figure 4.7: Phase tensors for all marine magnetotelluric sites. Fill is the phase tensor skew angle, β.

4.5 References

Caldwell, T. G., Bibby, H. M., & Brown, C. (2004). The magnetotelluric phase tensor. *Geophysical Journal International*, *158*(2), 457-469.

Key, K., & Constable, S. (2010). Coast effect distortion of marine magnetotelluric data: insights from a pilot study offshore northeastern Japan. *Physics of the Earth and Planetary Interiors*, *184*(3), 194-207.

Swift, C. M., Jr (1967), A Magnetotelluric Investigation of an Electrical Conductivity Anomaly in the Southwestern United States, Ph.D. thesis, Massachusetts Institute of Technology.

Chapter 5

2D Inversions

Initial attempts to invert the data set used the open-source code MARE2D developed by Kerry Key at Scripps Institution of Oceanography (*Key*, 2016). This parallel goal-oriented adaptive finite element code uses unstructured triangular grid elements. This allows for modeling of topography, dipping layers, and multiple scale structures without propagating small grid elements to depths and edges of the model. This is crucial, particularly for this data set with rapid changes in bathymetry, as sharp boundaries between the conductive ocean and resistive land can lead to wrapping in the measured fields that complicates data. Because small cells are not propagated to the model edges, MARE2D has faster run-times and uses less memory than finite-difference codes. MARE2D uses the Occam inversion methodology, meaning that smoother models are preferred (*Constable et al.,* 1987). This is appropriate for the MT method, as it is diffusive and therefore cannot constrain sharp boundaries or thin layers.

5.1 Mesh design

Designing an appropriate inversion parameter mesh for modeling is a crucial first step for inversion of MT data. It is important to develop a mesh that has refined enough elements to capture changes in bathymetry and to show small-scale features in the subsurface. However, too many elements can make the inversions too computationally expensive to run on current computer clusters. For this work, the region of interest was set to extend from the surface to a depth of 200 km across the distance covered by sites. This region of interest was then split into a shallower section, running from the surface to approximately 75 km depth, and a deeper section extending from 75 km to 200 km. The shallower region was filled with smaller elements to capture the bathymetry and to allow for smaller-scale features sampled by higher frequency fields to be reflected in the model. The deeper region was then filled with slightly coarser mesh, and outside the region of interest the mesh was allowed to auto-fill with the coarsest elements possible. In total the model has 79116 free parameters. Figure 5.1 shows the mesh beneath the collected sites. It should be noted that the mesh actually extends far beyond what is shown, both laterally and with depth, in order to insure that the boundary conditions are not violated

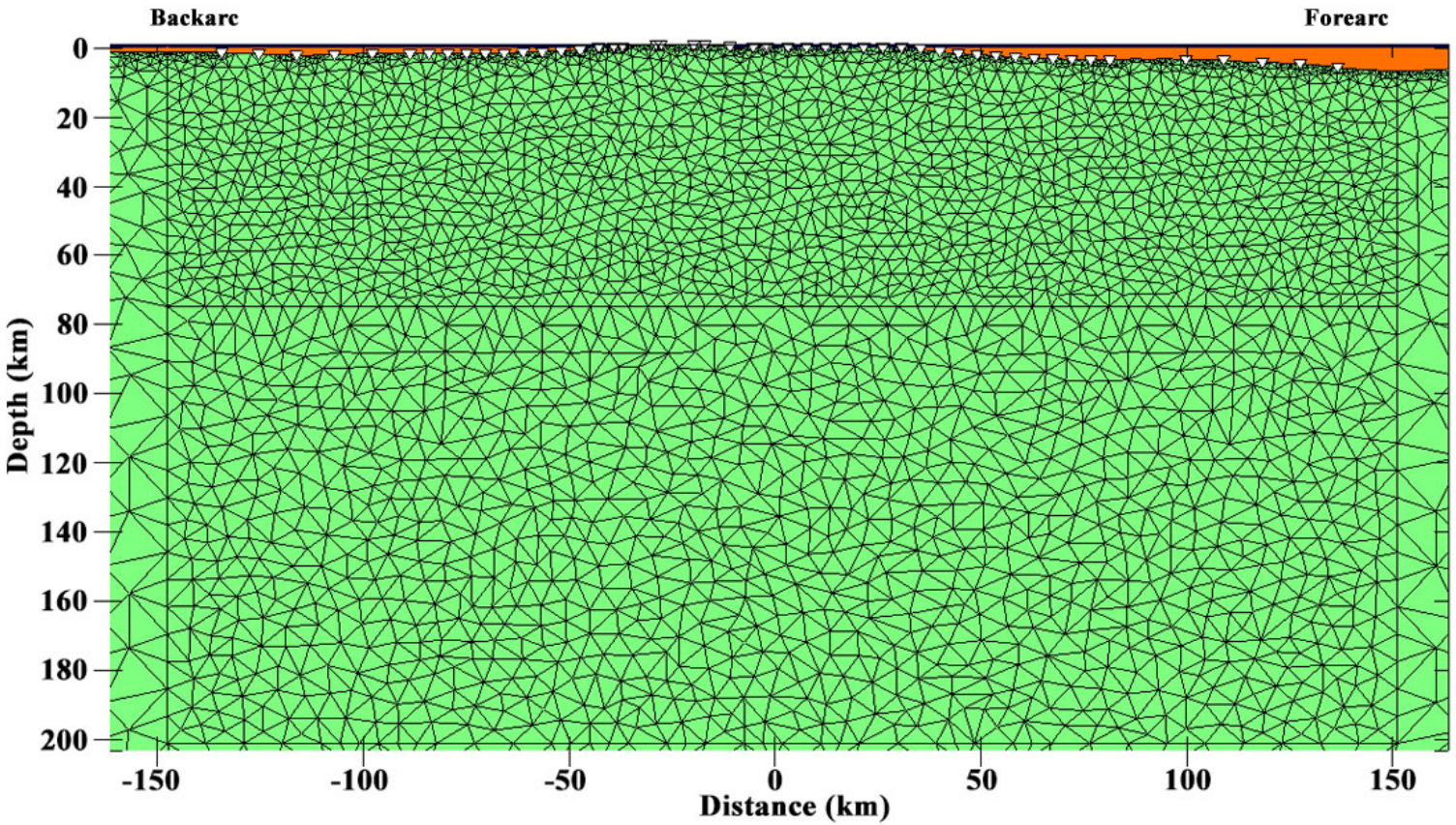

Figure 5.1: Mesh design used for MARE2D inversions. Backarc is to the left, forearc is to the right, and stations are shown as white triangles

5.2 Inversion of the full data set

Initially inversions of the Okmok data set excluded only data from sites with known issues, such as stations F06 and F17 (station F06 had a faulty channel, and station F17 was recovered with bent electrode arms). Station F24 was extremely noisy across all frequencies, and was therefore also removed. Ring sites were excluded, as they are not on the 2D profile and they are in shallow water with high noise due to strong water currents. The two highest frequencies were trimmed from all sites. However, no data was trimmed based on dimensional analysis. The resulting model from inversion of both the TE and TM modes is shown in Figure 5.2.

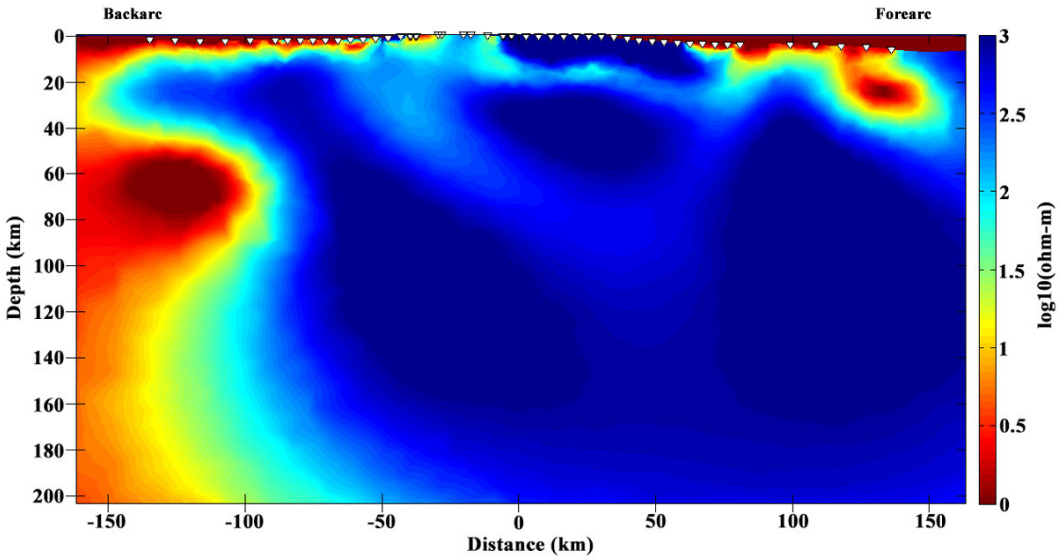

Figure 5.2: Iteration 21 of inversion using both modes of full data set, fitting the data to RMS 15.8065.

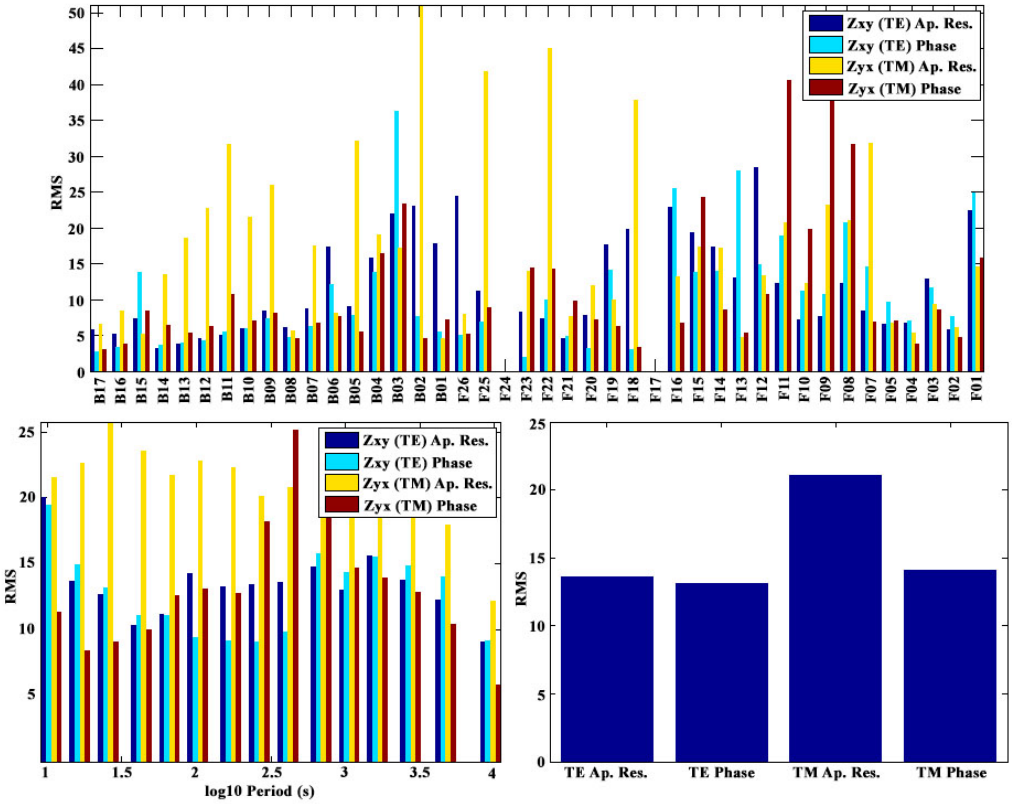

Figure 5.3: Misfit breakdown of inversion using both modes of full data set.

This inversion ran through 21 iterations, and reached a final RMS misfit of 15.8065. Figure 5.3 shows the breakdown of where misfit in this model is highest. In general, the best fit seems to be to stations in the far backarc, specifically sites B17 and B16, where misfit is down to approximately 5. Misfit is down to around 10 for sites F01-F05 in the forearc. For all other sites the misfit is very high, and so the model should not be considered reliable apart from in the far backarc. Interpretations in the far forearc are also dubious. The apparent resistivity or phase has high misfit for at least one mode across all frequencies, so the model is not more reliable at any particular depth. Focusing only on the backarc sites with relatively low RMS misfit, we see a strong conductor immediately beneath the furthest sites. A resistor on order of hundreds of ohm-m then extends to roughly 40 km depth. From 40 km to roughly 90km there is a very strong conductor, and at depth we see a slightly weaker conductor. Because this model has such high misfit across the majority of the stations, and across all depths in at least one mode, it is difficult to make any conclusions about subsurface structure. The most obvious way to decrease misfit is to mask any obviously 3D portions of the data set, as this 2D code will not be capable of creating models that fit such features.

5.3 Masking of 3D features

The polarization plots and swift skew evaluated in Chapter 4 of this thesis were used to determine what portions of the data set show 3D effects. Any point with a swift skew greater than 0.2 was deemed 3D and was masked prior to inversion. As previously

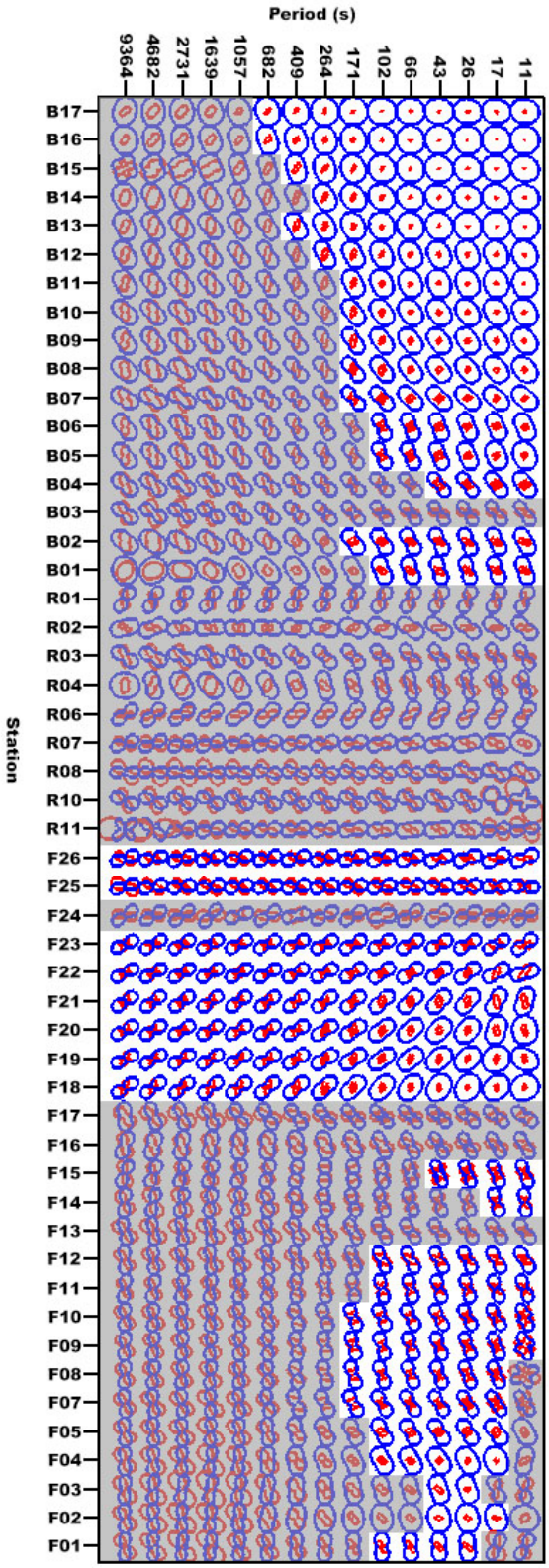

Figure 5.4: Polarization plot of full data set, with 3D masked portions colored gray.

discussed, this use of 0.2 as the cutoff point is somewhat arbitrary, so the polarization plots were used as confirmation that the points did indeed show 3D effects. Figure 5.4 shows the portions of the data set that were masked due to 3D effects. All ring sites were masked, both because of the 3D effects and due to their location off the profile. Stations B03, F24, F17, F16, and F13 were masked entirely due to large swift skew values. Across the backarc much of the data at depth was masked, with more points being masked closer to the volcanic center. In the forearc the same trend occurred, although the highest frequencies at the points furthest from the volcano also had to be trimmed. The only stations that did not require any sort of masking occurred at the shallow forearc sites lying between the volcanic center and the shelf break.

5.4 Inversion of the data set with 3D features masked

Initial inversion of the masked data set used both the TE and TM modes with an error floor of 10%. The inversion ran for 20 iterations, and reached an RMS misfit of 14.5892, decreasing the misfit by 1.3 as compared to the inversion of the full data set. The resulting model is shown in Figure 5.5. Figure 5.6 demonstrates where in this model misfit is highest. Overall, this masked inversion led to a much better fit for TE mode phase and apparent resistivity, as well as TM mode phase in the forearc. The TM mode apparent resistivity, however, remains problematic. In the forearc the overall RMS misfit is lower, but there is not as clear a trend in one single component having a higher misfit. In terms of which frequencies are fit better, RMS misfit seems to decrease with lower frequency, corresponding to deeper depths. The breakdown according to period again demonstrates that misfit is higher for TM mode

apparent resistivity. As with the inversion of the unmasked data, the best fit for this model is in the sites furthest in the backarc. The basic trends in the model here also match the unmasked inversion, with a shallow conductor directly beneath the sites, a resistor on order of hundreds of ohm-m from roughly 20-60 km depth, and then a more conductive (10-50 Ωm) conductor extending to depth. The deeper conductor does not have as low of a resistivity in this model.

Modeling the TE or TM mode independently can impact the depth sensitivity of the inversion, and can alter how 3D effects impact the results. As demonstrated by Berdichevsky et al. (1998), the TM mode is more sensitive to near-surface structure. It is also less sensitive to 3D effects from conductive structures. The TM mode also is more susceptible to static shift, which is not problematic in this case as we assume that the near-surface sediments are homogenous. In the same work Berdichevsky et al. show that the TE mode is sensitive to deeper structures, and will be less sensitive to 3D effects from resistive structures. It is therefore useful for us to invert the TE and TM modes of the masked data set independently.

Going into the modeling, one would expect for the TM mode to achieve a lower RMS misfit, as most of the 3D structure in the region would likely be due to conductive features associated with the magmatic system. The TE mode would be more sensitive than the TM mode to these structures. An inversion of the TM mode alone ran for 25 iterations, with the final inversion shown in Figure 5.7. The model ultimately reached an RMS misfit of 12.4058. This is only a minor improvement over the misfit from inverting both the TE and TM modes. Since the TM apparent

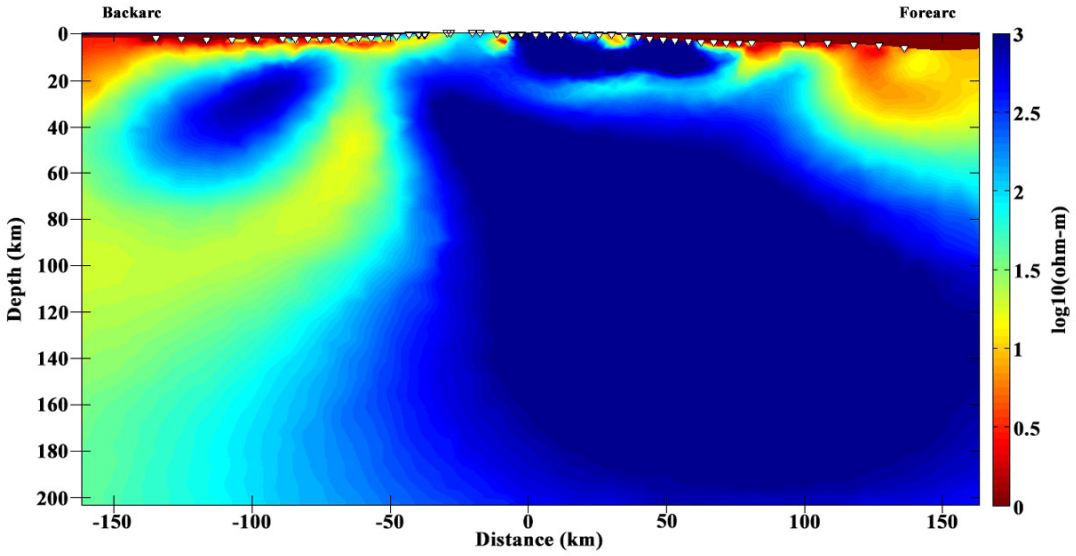

Figure 5.5: Iteration 20 of inversion using both modes after 3D portions of the data set have been masked, fitting the data to RMS misfit 14.5892.

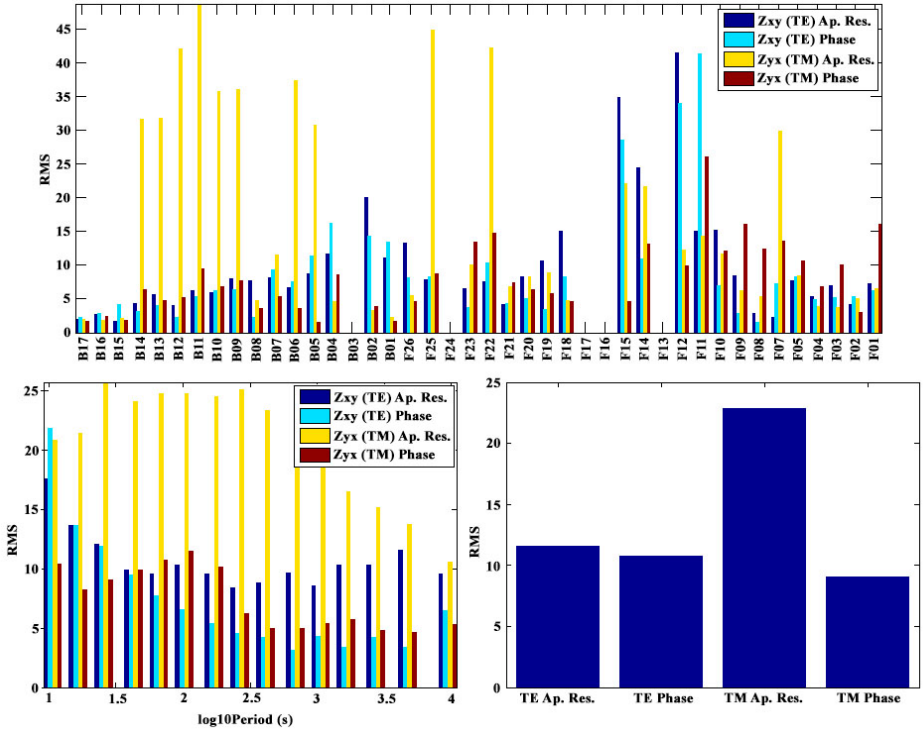

Figure 5.6: misfit breakdown inversion of both modes after 3D portions of the data set have been masked

resistivity was the most problematic portion of the inversion of both modes, as shown in Figure 5.6, this is not entirely unexpected. The breakdown of the RMS misfit from the inversion of the TM mode alone is shown in Figure 5.8. Again, we can see that across all sites the apparent resistivity is more problematic than the phase. If we focus solely on the shallow forearc between stations F05 and F01 where the misfit is relatively low, we see a conductor in the range of 50 Ωm dipping from the trench down towards the mantle beneath the volcano. This could correspond to the hydrated sediments being subducted along with the downgoing slab, although a model with better fit to the data would be needed to definitively show this.

Inverting the TE mode alone once 3D portions had been masked led to the only model with a RMS lower than 10. After 18 iterations the inversion reached an RMS misfit of 7.9327. Figure 5.11 shows where the misfit is distributed across the model. As with all previous models, the misfit in general is lower in the backarc. At all sites and frequencies, the phase is fit better than the apparent resistivity. As frequency decreases, the phase in general is fit better. As demonstrated by Berdichevsky et al. (1998), the TE mode is more sensitive to structure at depth. This combined with the improved RMS misfit at depth make it appealing to try to interpret the deeper structures shown in the model in Figure 5.10. However, it is important to keep in mind that most of the data at low frequencies was masked at due to its 3D nature. If only shallow data points are being inverted it is not logical to try to draw conclusions about deeper structure. It does appear that the TE mode does a good job mapping the thickness of the conductive seafloor sediments.

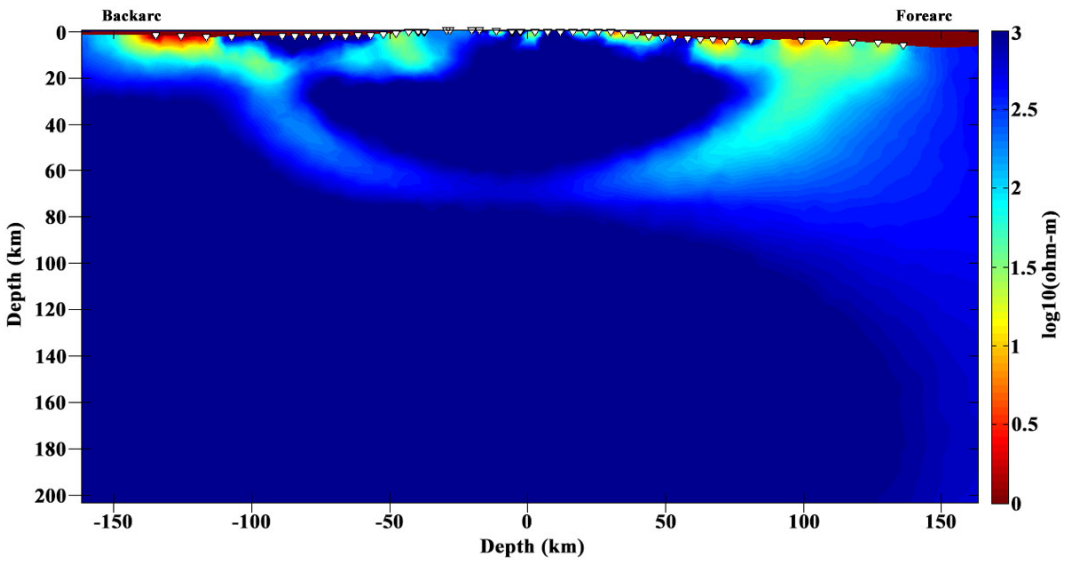

Figure 5.7: Iteration 25 of inversion of TM mode only after 3D portions of data set have been masked. RMS 12.4058.

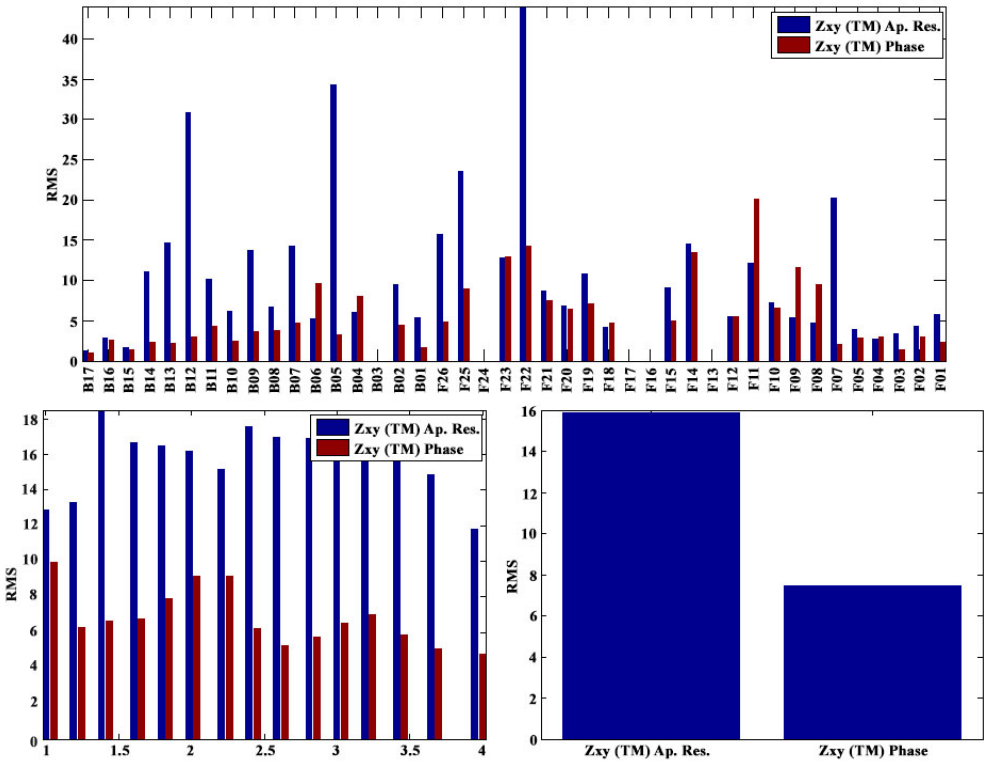

Figure 5.8: Misfit breakdown of the TM mode inversion after 3D portions of data set have been masked

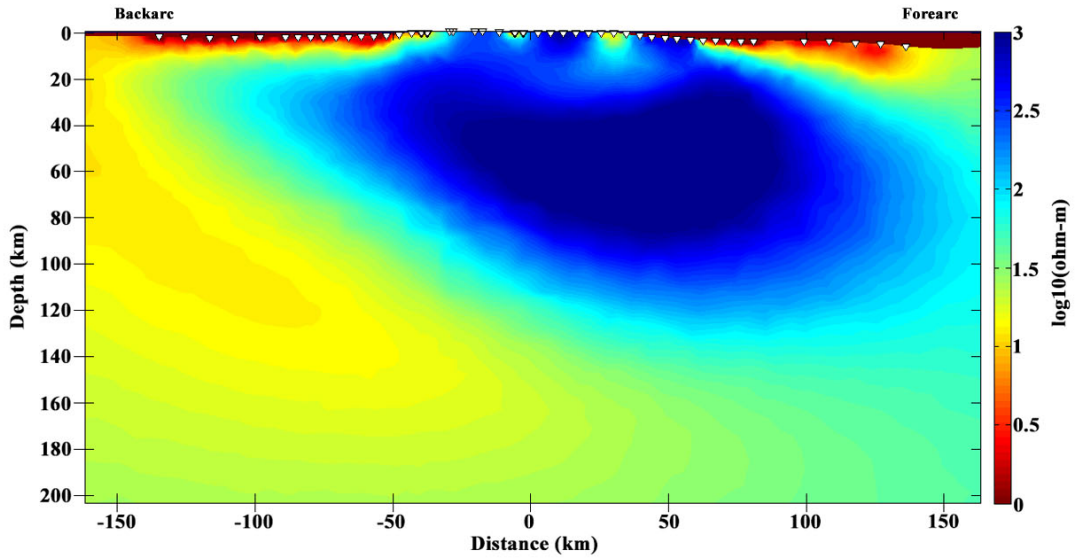

Figure 5.9: Iteration 25 of inversion of TE mode only after 3D portions of data set have been masked. RMS 7.9327.

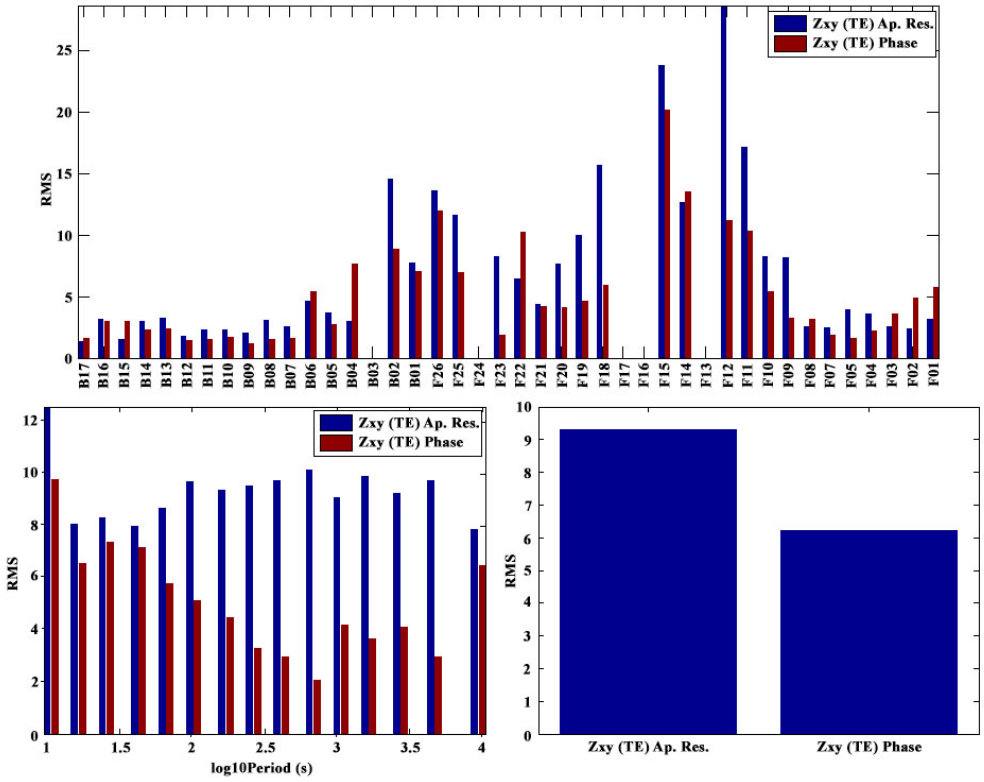

Figure 5.10: Misfit breakdown of inversion of TE mode with 3D portions of data set masked.

5.5 Conclusions and next steps

Across all models run, MARE2DEM seems to be able to fit phase better than apparent resistivity, and TE mode better than TM mode once 3D portions of the data set have been masked. When 3D effects are not masked MARE2DEM produces models with RMS misfit too high to be reliably interpreted. It is worth noting that all models discussed in this chapter assumed isotropy. It is possible that shifting to anisotropic models could decrease the misfit. However, it is safe to conclude that the extreme 3D nature of much of this data set necessitates the use of a 3D inversion code.

5.6 References

Berdichevsky, M. N., Dmitriev, V. I., & Pozdnjakova, E. E. (1998). On two-dimensional interpretation of magnetotelluric soundings. *Geophysical Journal International*, *133*(3), 585-606.

Constable, S. C., Parker, R. L., & Constable, C. G. (1987). Occam's inversion: A practical algorithm for generating smooth models from electromagnetic sounding data. *Geophysics*, *52*(3), 289-300.

Key, K. (2016), MARE2DEM: a 2-D inversion code for controlled-source electromagnetic and magnetotelluric data, *Geophys J Int*, *207*(1), 571–588, doi:10.1093/gji/ggw290.

Chapter 6

3D Forward Modeling

Currently there are no freely available 3D finite element codes capable of inverting electromagnetic data sets. As demonstrated in previous chapters of this thesis, many of the sites collected at Okmok show strong 3D effects. In general, the two-dimensional finite element code MARE2D can be used for preliminary inversions when portions of the data set containing 3D structure are masked. It is also possible to use only the TM mode, as it is less sensitive to 3D effects from conductive structures as compared to the TE mode (*Berdichevsky et al.,* 1998). Masking the 3D data and limiting inversion to the TM or TE mode alone was not effective in significantly decreasing the RMS misfit for this survey, however, as demonstrated in Chapter 5. To make full use of this data set and gain a complete understanding of the magmatic system at Okmok, it is important to include the portions that show significant 3D effects.

Attempts were made to forward model the area surrounding Okmok using the 3D finite difference code ModEM. Details of this code can be found in Egbert and Kelbert (2012) and Kelbert et al. (2014). Note that this code currently is not stable for inversion of marine data, limiting work to forward modeling.

All modeling was completed on the Cray CS300 computing cluster at the University of Hawaii at Manoa. As of March 2016, this cluster consisted of 5,876 cores and 178 standard nodes with 128GB of physical RAM. Each standard node consists of two 10-core Intel Ivy-Bridge processors. The system uses MPI and fat tree network topology. Maximum run time is three days. For most runs of ModEM four nodes were used.

6.1 Mesh refinement

The cusps in apparent resistivity and wrapping in phase at many of the sites collected at Okmok indicate that there is a very strong coast effect in the area due to dramatic changes in bathymetry. One of the biggest challenges related to this data set is creating a mesh for forward modeling and inversion that captures these rapid changes in seafloor shape. This is particularly a challenge with ModEM, as the finite difference code uses a structured rectangular grid. In order to model the complex bathymetry, we must create small cells in the center of the model space. These small cells then extend into thin rows and columns throughout the entire domain. This dramatically increases the number of cells used, and can often use more memory than is available.

Initial work with ModEM consisted of creating a 30 Ωm half space with draped bathymetry. A wide range of meshes were then tested to see how refined the near-surface grid could be without exceeding the memory capacity.

As a starting point, a mesh consisting of 250 m thick thin layers near surface was tested. Cells were set to be 1000 m square, with thickness of 250 m to a depth of 5 km. Padding with growth factor 1.5 was then added for 15 blocks north, south, east, and west.

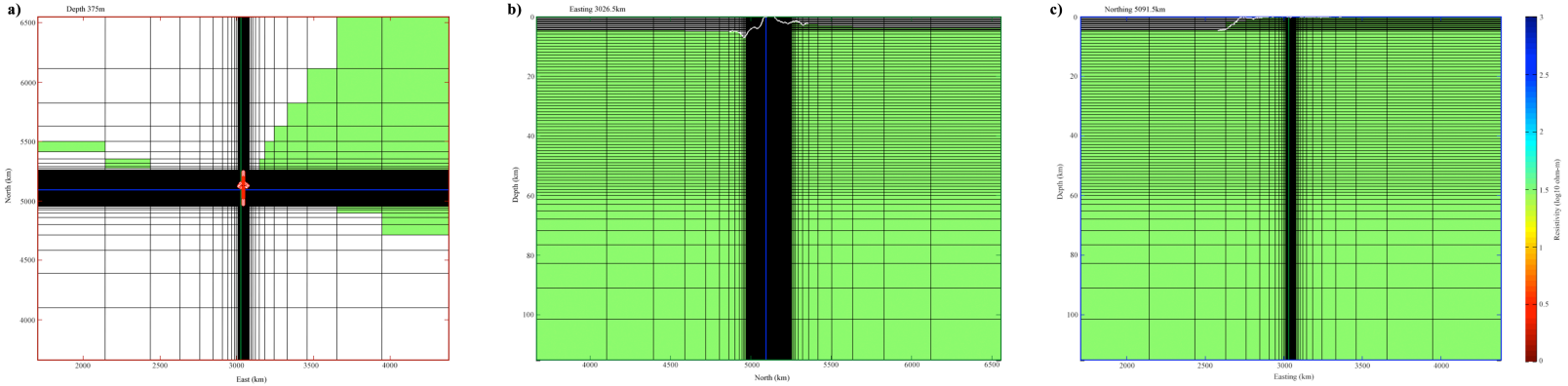

Figure 6.1: Preliminary mesh tested on Cray computing cluster. Near-surface cells are 1000 m square and 250 m thick, with padding added in all directions. Sites are shown as red and white circles, bathymetry is the white line near the surface.

Padding of fixed height 1000 m was added for 55 blocks down. An additional 10 blocks with a growth factor of 1.3 were added to the bottom of the model, as seen in Figure 6.1.

This model was run successfully, however a closer look at the mesh shows that it is not refined enough to accurately capture the dramatic changes in bathymetry in the near surface. In Figure 6.2 the red dots indicate stations on our marine profile, and the bold black line is true bathymetry. Since these instruments are seafloor receivers, they should rest roughly one meter above the black line. However, because the mesh is 250 m tall, many of the sites are placed well above the seafloor, in many cases at the water-air interface. In an area where the processed data indicates strong coast effect this is less

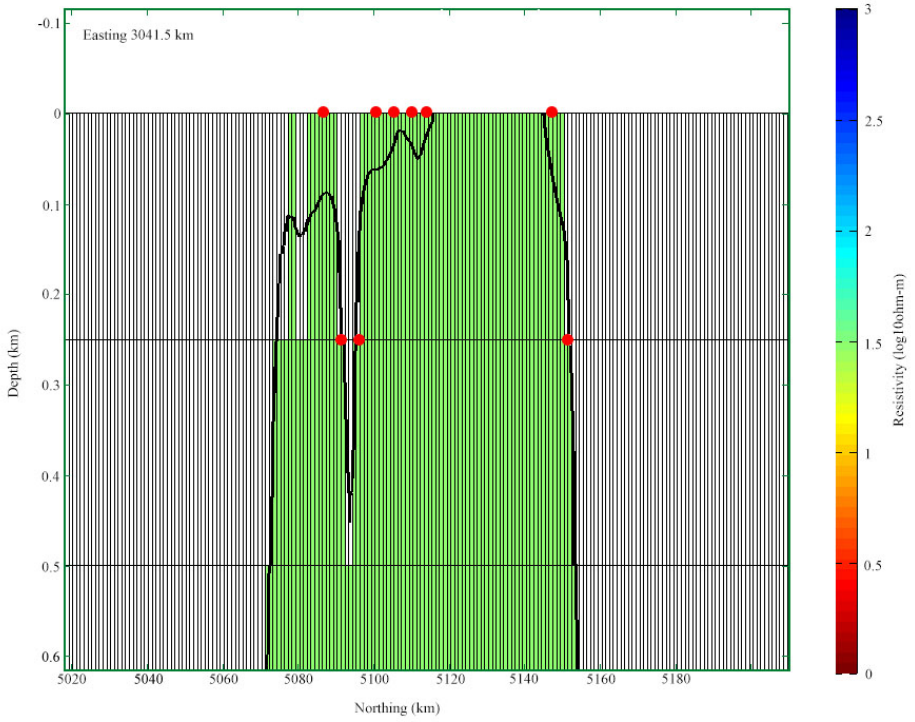

Figure 6.2: Zoomed-in view of mesh in the very near surface demonstrating that the mesh is too coarse to capture rapid changes in bathymetry. Sites are shown as solid red dots, and bathymetry is the bold black line.

than ideal, and may make it impossible to model complex features such as the phase wrapping in both TE and TM modes.

In an attempt to refine the model, numerous other mesh designs for the same half-space were created and run. The widths and heights of cells in the thin layers were varied, with the most refined cells being 50m cubic. Models were also tested with a 50 m thick cells overlying 250 m cells, with constant growth factor padding beneath. In one test the cells closest to the surface were set to 50 m thick, with constant growth factor of 1.2 on the padded cells beneath to a depth of roughly 75 km. In all of these cases, the run time exceeded the three-day limit on the Cray cluster and the jobs were killed before any output files were created. This indicates that the memory demands for these meshes were too high.

Based on the models run with different thin layers and padding, it was determined that the initial test with cells that are 1000 m square and 250 m thick near surface is the best mesh that can be achieved for this data set with the current version of ModEM. The initial run used a 30 Ωm half-space. In order to better understand what background resistivity is appropriate for the area, the same mesh was tested with half-space resistivities ranging from 30 Ωm to 1000 Ωm.

6.2 Varying half-space resistivity

In order to better understand what simplified models can best explain the data set, characteristic sites from the forearc and backarc were selected. Ring sites were not included in this comparison, as the coarse mesh led to them being placed at the sea

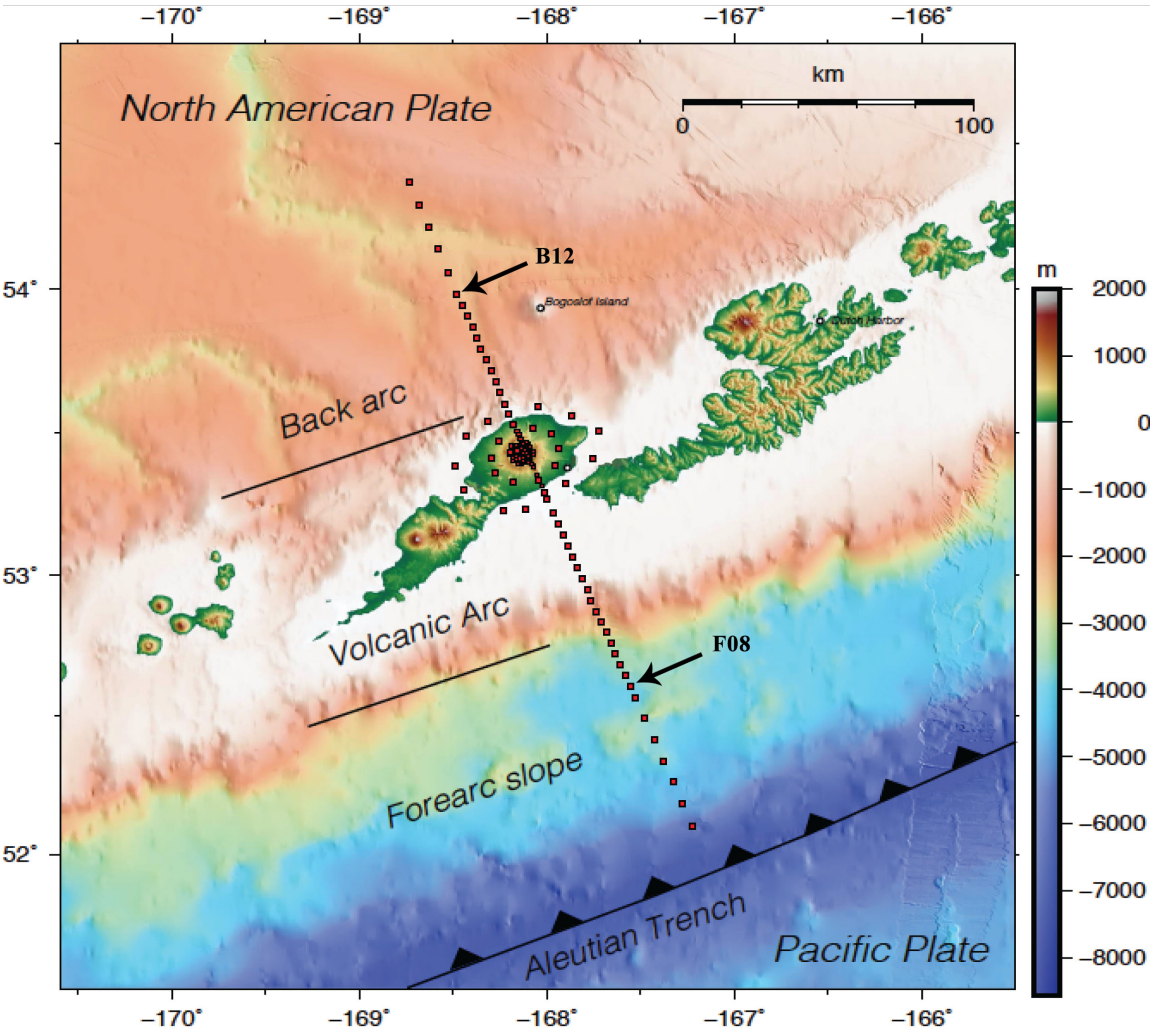

Figure 6.3: Locations of sites B12 and F08 in the broader survey area.

surface in the models. The data for these sites was also much noisier, as there are strong currents in the shallow water around the island.

In the backarc, site B12 was selected for comparison. The phase and apparent resistivity for this site are shown as the disconnected points in panels (a) and (b) of Figure 6.4. The swift skew is shown as the points connected by a solid line in panel (c) of the same figure. In general, the backarc sites have smooth curves in both phase and apparent

resistivity, with very little splitting between TE and TM modes. These features are apparent in station B12.

In the forearc, station F08 is used for comparison. The forearc sites have greater variation in characteristics in TE and TM mode phase and apparent resistivity, with some showing smooth curves, some having wrapping and cusps in one mode only, and some showing wrapping and cusps in both TE and TM modes. Site F08 was selected because it has cusps in apparent resistivity in both modes and there is wrapping in TE and TM phases. Wrapping and cusps in the TE mode have been seen before in areas with extreme bathymetry, as shown in Key and Constable (2010). However, these features had not previously been seen in the TM mode. It is therefore important to understand what subsurface features can contribute to these complexities in the data set.

Of the simple half-space models, the 30 Ωm model came the closest to matching the overall trends at sites B12 and F08 (see figure 6.4). In the backarc the model matches the general trend of TE and TM mode apparent resistivities being well aligned, with slight divergence starting around 100 s, although the overall resistivity is higher than is reflected in the data set. At station F08 the 30 Ωm half-space model does an excellent job of recovering TE mode apparent resistivity and phase, as seen in panels (d) and (e) of Figure 6.4. The cusp in apparent resistivity and the wrapping in phase are both reflected in the model, although the period is slightly higher for both than we see in the real data.

The 30 Ωm model fails to capture the higher swift skew values seen at both sites B12 and F08. At periods longer than 200-300 s, the skew for the real data for both sites is greater than 0.2. In the model the skew does not go above 0.1 for either site. The model also does not reflect any of the distinct features of the TM mode at the forearc site.

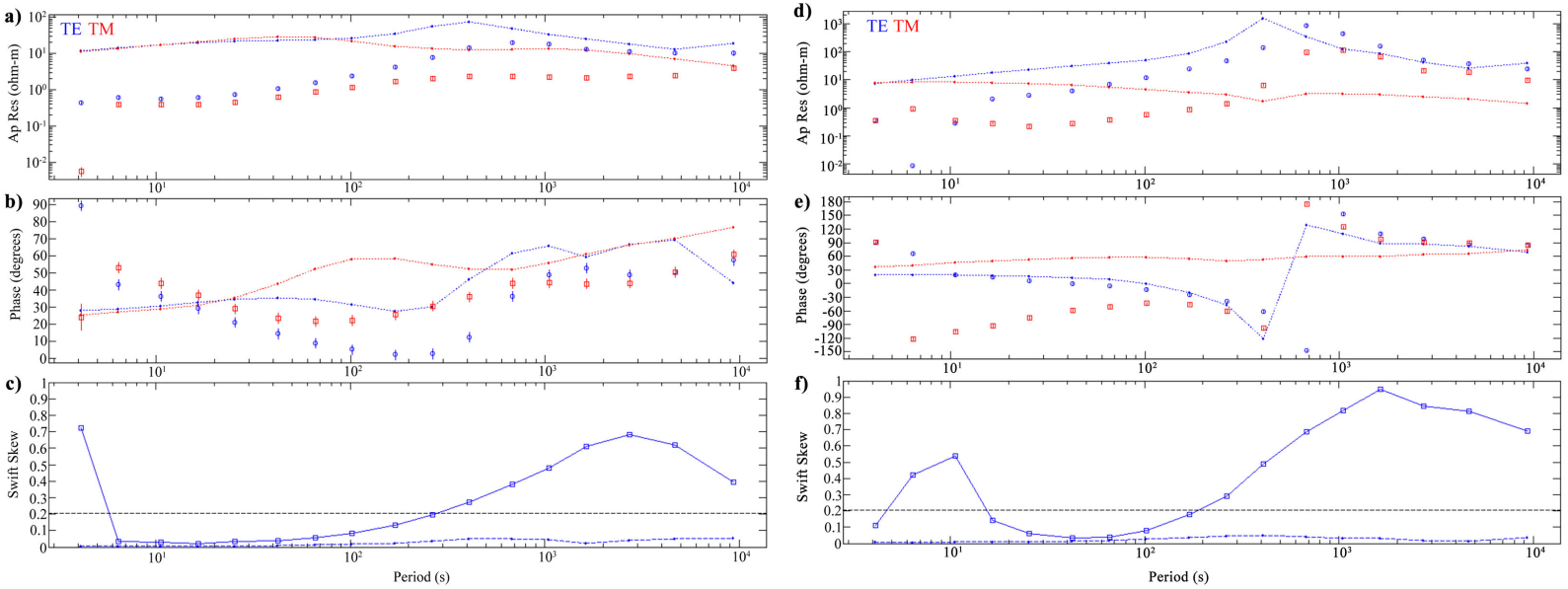

Figure 6.4: Results of the 30 Ωm half-space model. (a) apparent resistivity and (b) phase for site B12, with actual data shown as individual circles and the model shown as the connected smaller points. (c) Swift skew for B12, with the actual data as the solid connected line and the model as the thinner dotted line. (d) Apparent resistivity, (e) phase, and (f) swift skew for site F08 with the same model.

The model does not show a cusp in TM mode apparent resistivity, and the TM phase is a linear and smooth rather than having full wrapping. This indicates that a fairly simple structure with a 30 Ωm background resistivity may explain features in the backarc, but that much more work must be done to understand the complex trends seen in the real data in the forearc.

To test if changing the half-space resistivity could improve the fit in swift skew and forearc TM mode phase and resistivity a wide range of more resistive models were run. The results of the most extreme model, with a half-space resistivity of 1000 Ωm, are shown in Figure 6.5. In both the forearc and backarc the skew values increased and began to take the shape seen in the real data, although values are now too high. This indicates a lower resistivity would be more appropriate for matching the skew.

The 1000 Ωm half-space model demonstrates that the main features in the TM mode in the forearc cannot be explained with a half-space model with draped bathymetry alone. In this model the TE mode at F08 shows a negative cusp in apparent resistivity, and wraps numerous times from negative to positive phases. In the backarc, interestingly, there is wrapping in the phase in both TE and TM modes despite the relatively flat bathymetry in the area. Station F08 is much closer to sudden changes in bathymetry, and yet the model does not reflect any wrapping in the TM mode phase. More complex geologic structures will need to be incorporated into the model to explain the basic features seen in the real data set.

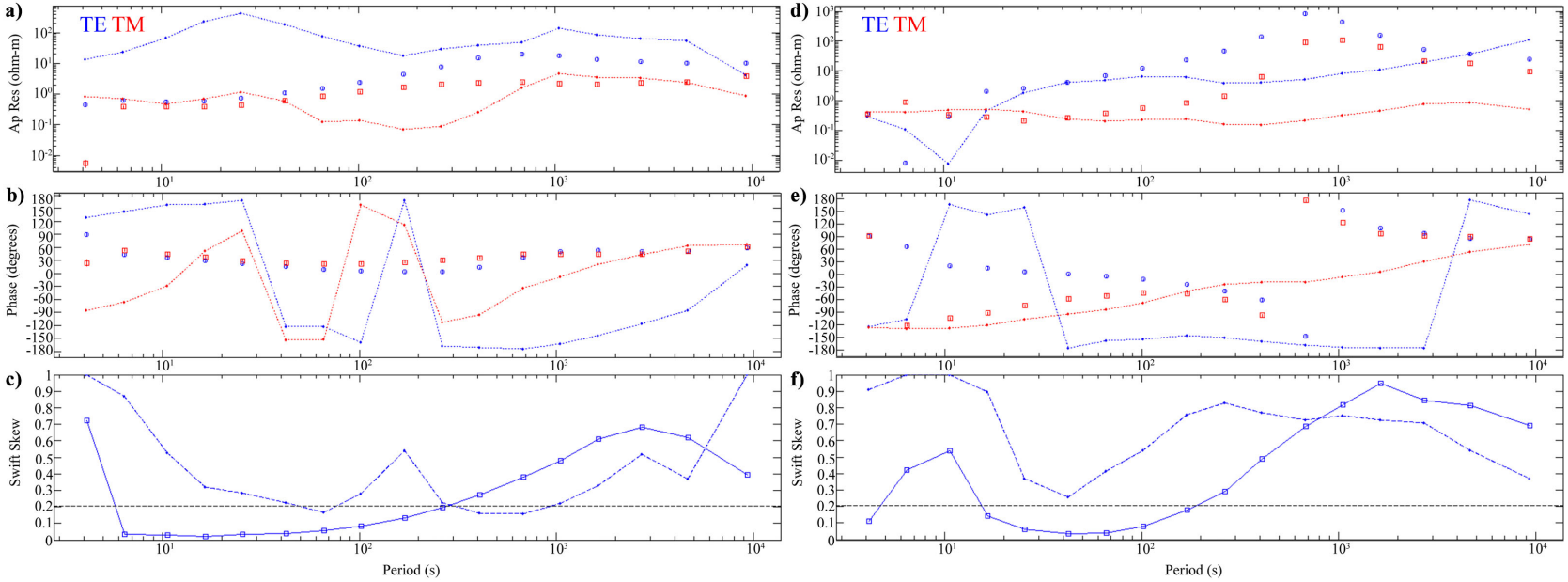

Figure 6.5: Results of the 1000 Ωm half-space model. (a) apparent resistivity and (b) phase for site B12, with actual data shown as individual circles and the model shown as the connected smaller points. (c) Swift skew for B12, with the actual data as the solid connected line and the model as the thinner dotted line. (d) Apparent resistivity, (e) phase, and (f) swift skew for site F08 with the same model.

6.3 Effects of thin conductive sediment layer

Early attempts at incorporating geologic structure used 500 m of saturated sediments in the near surface. This thickness of sediments is consistent with the conclusions of Leat and Larter (2003) for the Aleutians. Several sediment resistivities were tested, with the lowest resistivity being 1 Ωm. Figure 6.6 shows the results for sites B12 and F08 when 500 m of 1 Ωm sediments are draped over a 30 Ωm half-space incorporating true bathymetry.

In general, these results are nearly indistinguishable from what was seen with a simple 30 Ωm half-space (Figure 6.4). In the backarc the apparent resistivities are depressed slightly at shorter periods, and the TM phase becomes more linear. In the forearc the cusp in TE mode apparent resistivity has shifted to a longer period, making it more consistent with the actual data. The phase for the TE mode at F08 has become smoother. In general, this model is not a significant improvement to fit of the data.

The same sediment structure was also tested over a 200 Ωm half-space. In this case, the fit to phase and apparent resistivity in both the forearc and backarc was noticeably worse (see Figure 6.7). In the backarc cusps in the TE and TM mode apparent resistivities appeared that are not seen in the data. In the forearc the cusps disappeared and the apparent resistivity curves became nearly linear for both modes. The TM mode phase and apparent resistivity still do not reflect any of the characteristic traits of the actual data. This model did improve the fit of the swift skew for both sites, particularly in the range of 10-100 s, but clearly much more complex structure is needed to explain the data in the forearc.

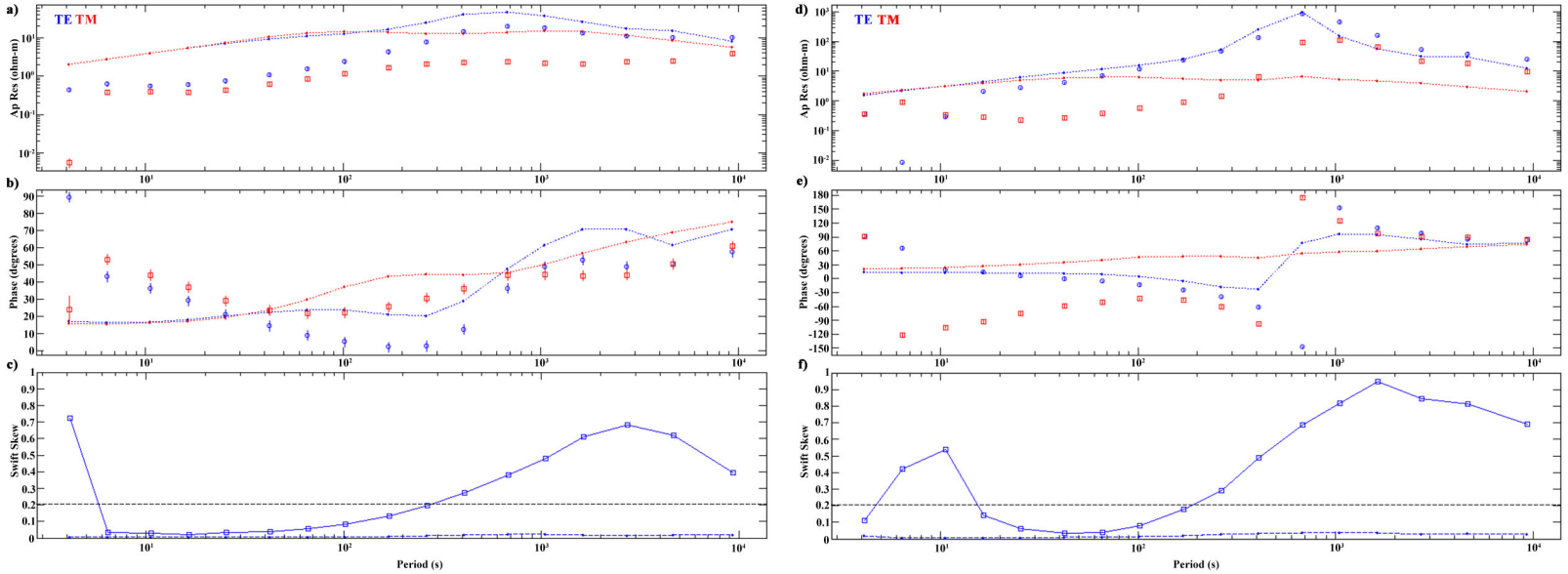

Figure 6.6: Results of a 30 Ωm half-space with 500 m of 1 Ωm sediments. (a) apparent resistivity and (b) phase for site B12, with actual data shown as individual circles and the model shown as the connected smaller points. (c) Swift skew for B12, with the actual data as the solid connected line and the model as the thinner dotted line. (d) Apparent resistivity, (e) phase, and (f) swift skew for site F08 with the same model.

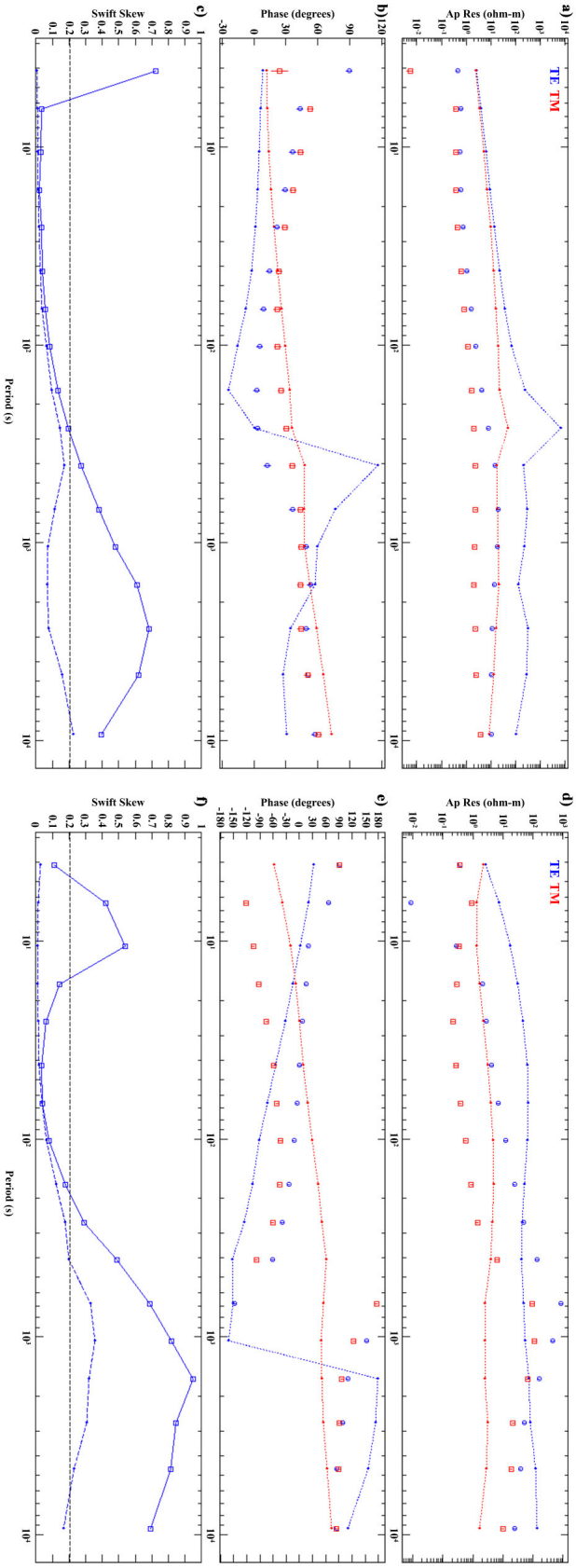

Figure 6.7: Results of a 200 Ωm half-space with 500 m of 1 Ωm sediments. (a) apparent resistivity and (b) phase for site B12, with actual data shown as individual circles and the model shown as the connected smaller points. (c) Swift skew for B12, with the actual data as the solid connected line and the model as the thinner dotted line. (d) Apparent resistivity, (e) phase, and (f) swift skew for site F08 with the same model.

6.4 Effects of resistive subducting slab

The resistive subducting slab is the largest regional geologic feature in the area. Slab1.0, a 3D model of 85% of the global subduction zones, was used to incorporate the subducting plate into this work. The model gives detailed geometry of the trench into the mid-mantle, including the seismogenic zone, based on a series of 2D profiles created from seismicity, bathymetry, and sediment thickness studies. These 2D profiles are created every 10 km and then stitched together to give a comprehensive view of the subducting slab (*Hayes et al*., 2012). Once the upper boundary of the slab was incorporated into our model the subducting plate was set to be 40 km thick with a range of resistivities. The most resistive model set the plate to be 1000 Ωm.

When the 1000 Ωm slab was incorporated into the 30 Ωm half-space model (with no conductive sediments), the only improvement to data fit was an increase in skew at longer periods in the forearc (Figure 6.8). In the backarc the TE mode phase jumped erratically in this model, rather than behaving as a smooth curve as seen in the actual data. The subducting slab does not explain the odd behavior in TM mode seen in the forearc.

Increasing the resistivity of the subsurface surrounding the slab to 100 Ωm increased the skew in both the forearc and backarc to values much closer to the actual data (Figure 6.9). However, this model led to cusps in the apparent resistivity and wrapping in the phase in both the forearc and backarc that is inconsistent with the collected data set, indicating that the coast effect in the model is stronger than what we see in reality. A model that is generally more conductive will reduce this coast effect and

bring the responses back down towards what we see in the collected data. Again, this model does not account for the cusp in TM apparent resistivity and the wrapping in TM phase in the backarc.

6.5 Conclusions

Simple models consisting of draped bathymetry over a half-space incorporating either a resistive subducting slab or a conductive layer of sediments match the general trends seen in the backarc of this data set. Further modeling with more complex subsurface geology may improve fit to the actual data in the forearc, but as of yet no combination of half-space resistivity and simple geologic features has matched the cusps in TM mode apparent resistivity and wrapping in TM phase. Future modeling could incorporate melt pooling at different depths beneath the caldera, and could vary sediment thickness and resistivity between the backarc and forearc. When a 3D finite-element code is complete it will be possible to invert this data set in both TE and TM modes with no high-quality data trimmed, allowing for a better look at what the true electrical resistivity structure beneath this active volcano is.

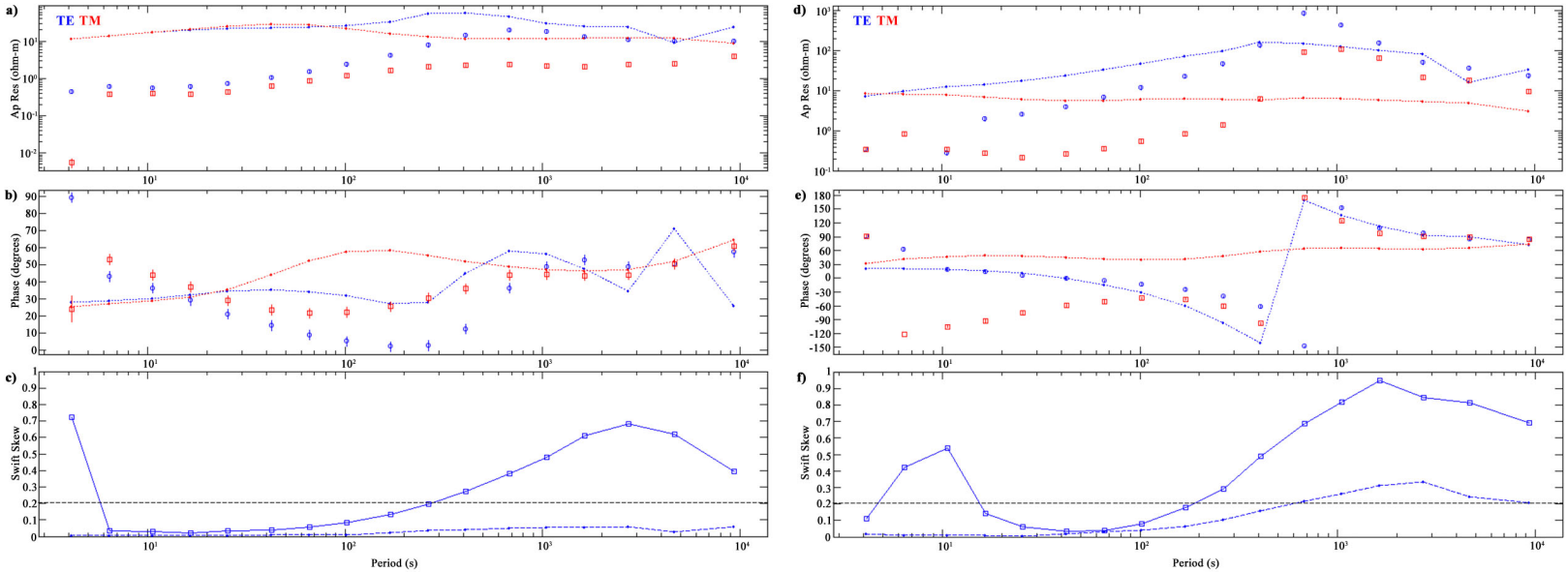

Figure 6.8: Results of a 30 Ωm half-space with a 40 km thick 1000 Ωm slab. (a) apparent resistivity and (b) phase for site B12, with actual data shown as individual circles and the model shown as the connected smaller points. (c) Swift skew for B12, with the actual data as the solid connected line and the model as the thinner dotted line. (d) Apparent resistivity, (e) phase, and (f) swift skew for site F08 with the same model.

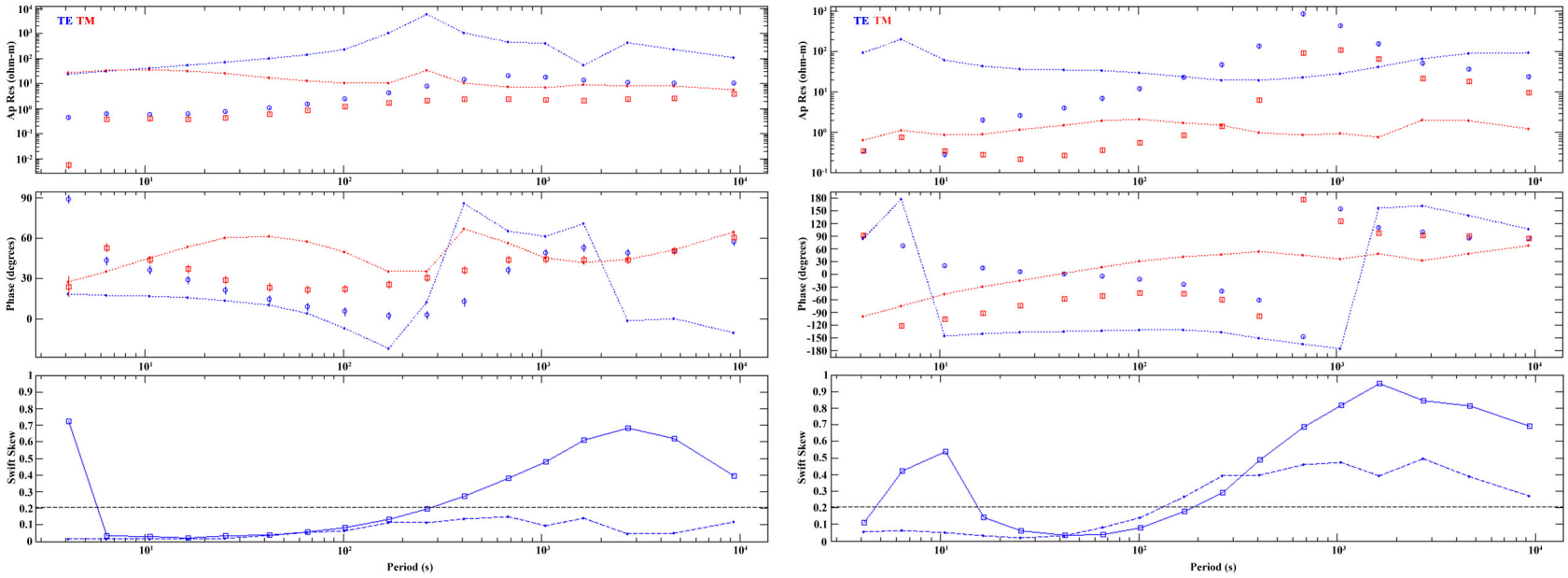

Figure 6.9: Results of a 100 Ωm half-space with a 40 km thick 1000 Ωm slab. (a) apparent resistivity and (b) phase for site B12, with actual data shown as individual circles and the model shown as the connected smaller points. (c) Swift skew for B12, with the actual data as the solid connected line and the model as the thinner dotted line. (d) Apparent resistivity, (e) phase, and (f) swift skew for site F08 with the same model.

6.6 References

Berdichevsky, M. N., Dmitriev, V. I., & Pozdnjakova, E. E. (1998). On two-dimensional interpretation of magnetotelluric soundings. *Geophysical Journal International*, *133*(3), 585-606.

Egbert, G. D., & Kelbert, A. (2012). Computational recipes for electromagnetic inverse problems. *Geophysical Journal International*, *189*(1), 251-267.

Kelbert, A., Meqbel, N., Egbert, G. D., & Tandon, K. (2014). ModEM: a modular system for inversion of electromagnetic geophysical data. *Computers & Geosciences*, *66*, 40-53.

Key, K., & Constable, S. (2011). Coast effect distortion of marine magnetotelluric data: insights from a pilot study offshore northeastern Japan. *Physics of the Earth and Planetary Interiors*, *184*(3), 194-207.

Leat, P. T., & Larter, R. D. (2003). Intra-oceanic subduction systems: introduction. *Geological Society, London, Special Publications*, *219*(1), 1-17.

Appendix 1

History of Fort Glenn

The first written records of eruptions at Okmok come from the 18th and 19th centuries when Russian exploration and colonization was beginning in the Aleutians. Umnak was first spotted in 1741 by a Russian ship involved in an expedition to North America. However, with the exceptions of a handful of fur traders, the Russians did not set foot on the island. Instead, observations of eruptions were dependent on a ship happening to pass by on a clear day during an explosive event. Alaska was purchased by the United States in 1867, but the first survey of Umnak did not occur until 1883 when a new dome formed offshore Bogoslof Island, to the northeast of Umnak (*Byers,* 1959).

The record of eruptions at Okmok becomes much more detailed beginning with World War 2. Shortly after Pearl Harbor the United States intercepted messages indicating that the Japanese intended to attack Midway and the Aleutian Islands. If the Japanese were to occupy Unalaska Island (home to Dutch Harbor), they would have easy access to the mainland United States as well as Siberia. Alaska would be isolated and susceptible to attack, and a major shipping lane through Unimak pass would fall into Japanese control (*Garfield,* 2010). American resources in the area were exceptionally thin, but it became evident that an airstrip would be needed to defend Dutch Harbor. There was no suitable land on Unalaska Island, so plans were put in motion to build a

base on nearby Umnak Island. Construction was initially disguised as a fish packing plant. Engineers raced against the clock, laying down 90,000 hand-fitted pieces of the newly developed Marsden matting to create a pierced steel runway at Cape Field, also called Fort Glenn, in less than two weeks. By March 1942 the project was complete, and Fort Glenn became home to the "Aleutian Tigers" of the Eleventh Air Force. On June 3 and 4, 1942, the Japanese attacked Dutch Harbor. The intercepted messages, combined with an early radar system that detected the incoming planes, allowed soldiers to reach defensive positions in time and damage to Dutch Harbor was minimal. A flaw in the communication system made it so that Fort Glenn did not receive word of the attack until after the Japanese planes were gone. Instead, it was fighters from Cold Bay, significantly further away, that responded. However, the pilots from Fort Glenn were involved in subsequent searches for the Japanese in the area and defense of Dutch Harbor on the second day of the attacks (*Garfield,* 2010). In later parts of the war the Fort Glenn became a forward operating base for attacks on the Japanese-occupied Kiska, some 1,200 miles west of Umnak.

In 1945 US forces stationed at Fort Glenn observed an eruption at Okmok. The eruption did no damage to the military base, but it forced authorities to recognize that military installations throughout the Aleutians were susceptible to damage from active volcanoes. In October 1945 the Alaskan Defense command requested that the USGS complete systematic studies of the Aleutian Islands. Okmok was one of the first volcanoes studied due to its recent eruption and proximity to Fort Glenn (*Byers,* 1959).

Fort Glenn was shut down shortly after WW2, and most of the buildings are now in ruins. One of the three cinder runways built during WW2 remains operational,

however, and the area is now home to the Bering Pacific Ranch. The cattle on the island are largely left free to roam, but in summer months up to a dozen ranchers are present to help with round up and shipment of the animals. During an eruption in 1997 no instrumentation was installed on the ground at Okmok. Observations of this eruption come primarily from remote sensing, supplemented by information provided by the ranchers at Fort Glenn. At one point during the eruption one of the ranchers hiked to the caldera rim and made observations about the lava flow crossing the caldera floor (*Patrick,* 1997). In 2008 it was a call from the ranchers as they were evacuating that first notified Alaska Volcano Observatory (AVO) that Okmok was erupting. One of the quick-thinking ranchers collected a sample of ash from the initial stages of the eruption as they were fleeing on a fishing boat. This sample has allowed scientists to compare the composition of the erupted material at different times during the eruption (*Larsen,* 2013). The ranch headquarters at Fort Glenn have also served as home base for most scientific expeditions focused on Okmok in recent decades.

A1.1 References

Byers Jr, F. M. (1959). *Geology of Umnak and Bogoslof Islands, Aleutian Islands, Alaska* (No. 1028-L). US Govt. Print. Off.,.

Garfield, B. (2010). *Thousand-Mile War: World War II in Alaska and the Aleutians* (No. 4). University of Alaska Press.

Larsen, J. F., Śliwiński, M. G., Nye, C., Cameron, C., & Schaefer, J. R. (2013). The 2008 eruption of Okmok Volcano, Alaska: Petrological and geochemical constraints on the subsurface magma plumbing system. *Journal of Volcanology and Geothermal Research*, *264*, 85-106.

Patrick, M. R., Dehn, J., & Dean, K. (2004). Numerical modeling of lava flow cooling applied to the 1997 Okmok eruption: Approach and analysis. *Journal of Geophysical Research: Solid Earth*, *109*(B3).

Appendix 2

Aviation Hazards

The sudden jump in eruptive activity at Okmok during 2008 is particularly alarming as the volcano lies beneath a major trans-Pacific flight path, as shown in Figure A2.1. Volcanic ash is extremely abrasive and can have a wide range of impacts on jet aircraft. It can scour windshields and can cause severe damage to landing lights and engines. It can also affect sensors that deliver electronic data to the automated systems that fly the aircraft, and can impact instrumentation that determines altitude and air speed (*Salinas*, 2004). Current radar instruments are not able to detect ash clouds; thus the only guaranteed precaution is total avoidance.

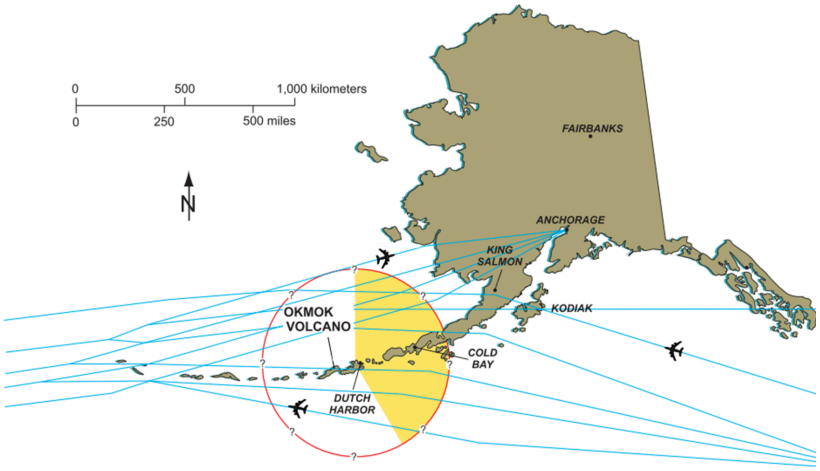

Figure A2.1: Major flight paths over Okmok and the surrounding region. Modified from Beget et al. (2005).

In recent decades there have been numerous close calls when an aircraft encountered an ash cloud unexpectedly. The most dramatic example comes from December 15, 1989. KLM Flight 867, with 231 passengers and 14 crew onboard, was scheduled to fly from Amsterdam to Tokyo with a refueling stop in Anchorage. Prior to flight the pilots were briefed about an eruption at Redoubt volcano to the west of Anchorage (labeled as volcano 3 in Figure 1.1). The flight proceeded as usual, and the plane began normal descent into Anchorage. Suddenly, at 25,000 feet, the aircraft encountered ash from Redoubt. The pilots immediately initiated a climb to get out of the ash cloud. At 27,900 feet all four engines lost power. The plane glided for four minutes, dropping to 17,200 feet before two engines were restarted, and descending to 13,300 feet before all four engines were restarted. Terrain in the area ranged from 7,000 to 11,000 feet. The plane was able to land in Anchorage, with no harm to passengers. However, the new plane sustained $80 million dollars in damage. Four other aircraft had encounters with this same ash cloud in the Anchorage area, although none lost power to any engines. Two additional flights encountered the ash cloud outside of El Paso, Texas, some 5,300 km away and 55 hours after the ash was created (*Casadevall*, 1994). Eruptions of Augustine (*Yount*, 1987) and Kasatochi (*Hudnall,* 2009) volcanoes in the Aleutians have also had major impacts on air travel over Alaska. However, there were no reports of planes encountering ash clouds from the 1997 eruption of Okmok.

Following the 1997 Okmok eruption a report was published about volcanic hazards associated with the system (*Beget et al*., 2005). It was determined that the primary hazard from future eruptions of Okmok would be ash clouds impacting air travel.

In the past 200 years numerous eruptions have ejected material up to 20 km above sea level. Although most historic eruptions have had much smaller ash clouds, an extreme eruption could create a plume to 40km above sea level. Ash from Okmok would be primarily carried to the northeast and east, but a change in wind direction could lead to ash being deposited anywhere in the region.

Despite the suddenness of the 2008 eruption and the location of Okmok beneath a major flight path, there was minimal impact on air travel. One military aircraft encountered the ash cloud near Kodiak Island on July 15, 2008, but pilots didn't note any changes in smell or aircraft performance, and the incident was deemed non-damaging (*Hudnall and Krueger*, 2009).

In the days following the start of the eruption at Okmok the ash cloud moved across the northwestern United States and Canada. Figure A2.2 shows sulfur dioxide as a proxy for ash across Washington, Idaho, and Montana on July 17, 2008 (five days after the eruption initiated).

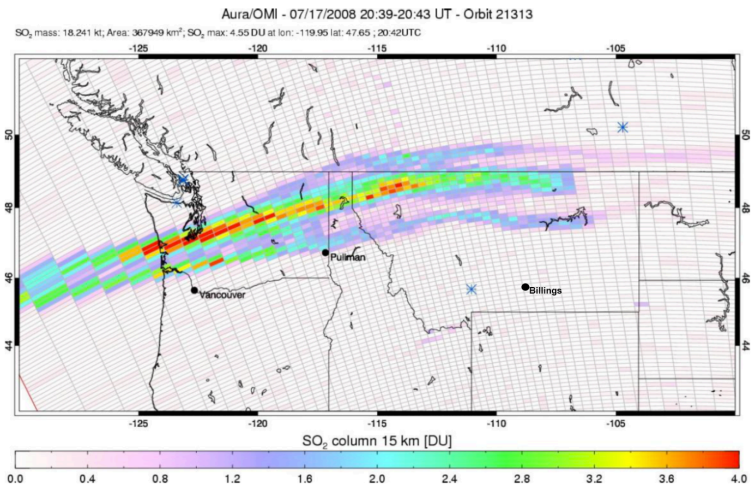

Figure A2.2: SO_2 as a proxy for ash particulates five days after the 2008 eruption of Okmok. Modified from Hudnall and Krueger (2009).

.

In response, the Volcanic Ash Advisory Center in Washington issued an advisory over much of the northwestern United States. The ash lingered in the area for several days. Figure A2.3 shows the plume over Billings, Montana as seen from the cockpit of a commercial Alaska Airlines flight on July 19, 2008. In this image the ash cloud is estimated to be between 32,000 and 36,000 feet above mean sea level. The impacts of this 2008 eruption were relatively minor, yet they still demonstrate that ash from Okmok can have an impact on aviation, both in the immediate region and across the United States as a whole. Understanding this system is crucial, as future eruptions could have major disruptive impacts on aviation throughout much of the country.

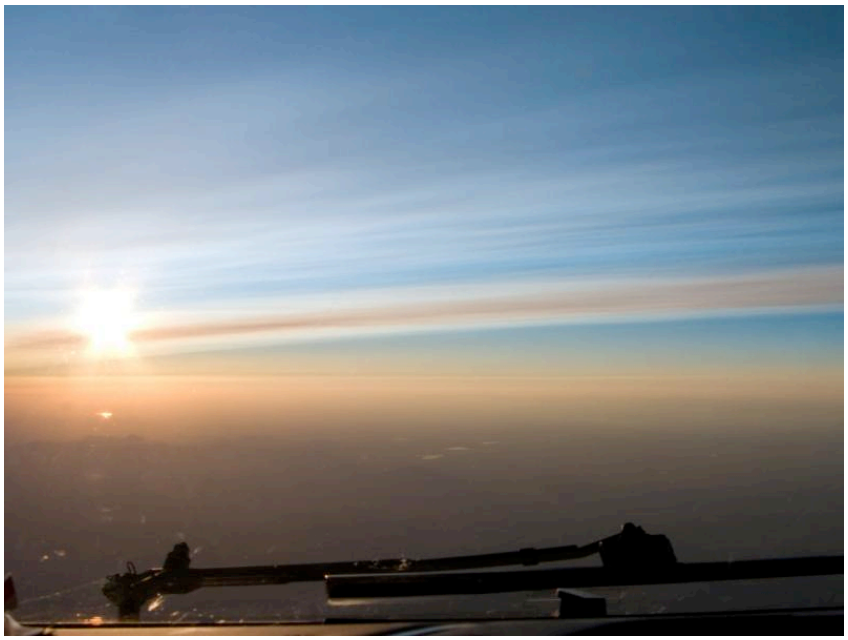

Figure A2.3: Ash cloud from the July 12, 2008 eruption at Okmok over Billings, Montana from the cockpit of commercial Alaska Airlines passenger jet on July 19. Plume is between 32,000 and 36,000 feet above mean sea level (image courtesy of Bradley Johnson and Alaska Airlines).

A2.1 References

Begét, J. E., Neal, J. F., Nye, C. A., & CJ Schaefer, J. R. (2005). Preliminary volcano-hazard assessment for Okmok volcano, Umnak Island, Alaska. *Report of Investigations — Alaska. Division of Geological & Geophysical Surveys, 3*.

Casadevall, T. J. (1994). The 1989–1990 eruption of Redoubt Volcano, Alaska: impacts on aircraft operations. *Journal of Volcanology and Geothermal Research*, *62*(1), 301-316.

Hudnall, L. A., Krueger, A. J., Matus, A., Murray, J. J., & Pippin, M. (2009). The Impacts on Air Traffic of Volcanic Ash from the Okmok and Kasatochi Eruptions During the Summer of 2008. In *1st AIAA Atmospheric and Space Environments Conference* (p. 3637).

Salinas, L. J. (2004, November). Volcanic ash clouds pose a real threat to aircraft safety. In *2nd International Conference on Volcanic Ash and Aviation Safety*.

Yount, M. E., Miller, T. P., & Gamble, B. M. (1987). The 1986 eruptions of Augustine volcano, Alaska: hazards and effects. *US Geol Surv Circ*, *998*, 4-13.